Spin and Charge Fluctuations Behind Strange Metallicity in the Hubbard Model

By

Gopal Prakash
PHYS10201705006

The Institute of Mathematical Sciences, Chennai

A thesis submitted to the
Board of Studies in Physical Sciences
In partial fulfillment of requirements
for the Degree of
DOCTOR OF PHILOSOPHY
of

HOMI BHABHA NATIONAL INSTITUTE

September 25, 2025

Homi Bhabha National Institute

Recommendations of the Viva Voce Committee

As members of the Viva Voce Committee, we certify that we have read the dissertation prepared by Gopal Prakash entitled "Spin and Charge Fluctuations Behind Strange Metallicity in the Hubbard Model" and recommend that it may be accepted as fulfilling the thesis requirement for the award of Degree of Doctor of Philosophy.

Sibasish Ghosh

Chairman - Sibasish Ghosh Date: September 25, 2025

S. R. Hassan

Guide/Convenor - Syed R Hassan Date: September 25, 2025

Examiner - Krishnendu Sengupta Date: September 25, 2025

Vsuryanarayana

Member 1 - Venkata Suryanarayana Nemani Date: September 25, 2025

Pinaki Chaudhuri

Member 2 - Pinaki Chaudhuri Date: September 25, 2025

Member 3 - Shrihari Gopalakrishna Date: September 25, 2025

Member 4 - Rajesh Narayanan Date: September 25, 2025

Final approval and acceptance of this thesis is contingent upon the candidate's submission of the final copies of the thesis to HBNI.

I hereby certify that I have read this thesis prepared under my direction and recommend that it may be accepted as fulfilling the thesis requirement.

Date: September 25, 2025

S. R. Hassan

Place: IMSc, Chennai

Guide : Syed R Hassan

STATEMENT BY AUTHOR

This dissertation has been submitted in partial fulfillment of requirements for an advanced degree at Homi Bhabha National Institute (HBNI) and is deposited in the Library to be made available to borrowers under rules of the HBNI.

Brief quotations from this dissertation are allowable without special permission, provided that accurate acknowledgement of source is made. Requests for permission for extended quotation from or reproduction of this manuscript in whole or in part may be granted by the Competent Authority of HBNI when in his or her judgement the proposed use of the material is in the interests of scholarship. In all other instances, however, permission must be obtained from the author.

Gprakash

Gopal Prakash

DECLARATION

I hereby declare that the investigation presented in the thesis has been carried out by me. The work is original and has not been submitted earlier as a whole or in part for a degree / diploma at this or any other Institution / University.

Gprakash
Gopal Prakash

LIST OF PUBLICATIONS ARISING FROM THE THESIS

Published

- **Strong local bosonic fluctuations: The key to understanding strongly correlated metals**
  S.R.Hassan, Gopal Prakash, N.S.Vidhyadhiraja, T.V.Ramakrishnan
  Phys. Rev. B 110, 075106

Submitted

- **Intricately Entangled Spin and Charge Diffusion and the Coherence-Incoherence Crossover in the High-Dimensional Hubbard Model**
  Gopal Prakash, S.R.Hassan, M.S. Laad, N.S.Vidhyadhiraja, T.V.Ramakrishnan
  arXiv:2501.08121 (Submitted to PRB)

Grakash
Gopal Prakash

List of presentations and participations at conferences

- Presented a poster titled *'Self consistent theory of U infinity Hubbard Model in large d'* at the Conference on Fractionalization and Emergent Gauge Fields in Quantum Matter held in Dec 2023 at ICTP, Trieste, Italy.
- Presented a poster titled *'Self consistent theory of U infinity Hubbard Model in large d'* at the WE-Heraeus-Seminar on Strange Metals in Quantum Materials and Quantum Emulators held in Dec 2023 at Physikzentrum Bad Honnef, Bad Honnef, Germany.
- Participated in *Frustrated Metals and Insulators* conference held in Sep 2022 at ICTS, Bengaluru, India.
- Participated in *Geometrical phases in optics and topological matter* conference in Jan 2020 held at ICTS, Bengaluru, India.
- Participated in *Novel Phases of Quantum Matter* conference held in Dec 2019 at ICTS, Bengaluru, India.
- Participated in *National Summer School on Statistical Physics* held in June 2018 at S.N. Bose Center for Basic Sciences, Kolkata, India.

To all my Loved Ones

ACKNOWLEDGEMENTS

This thesis has been possible with the help and support of numerous people including my peers, friends and family. I would like to take this opportunity to thank everyone who has been a part of my PhD journey.

First and foremost, I would like to thank my supervisor Prof Syed R Hassan for his patience, insightful discussions as well as guidance during the course of my PhD. This work wouldn't have been possible without his relentless efforts and support.

I would like to thank the members of doctoral committee, Prof Venkata Suryanarayana Nemani, Prof Sibasish Ghosh, Prof Srihari Gopalakrishna, Prof Pinaki Chaudhuri, Prof Rajesh Narayanan for closely observing my progress throughout the PhD, providing feedbacks and always being ready to help.

I would like to thank my collaborators Prof T V Ramakrishnan, Prof N S Vidhyadhiraja, Prof Mukul Laad with whom I had thorough discussions and got to learn a lot and find possible directions for my work. Thanks to Prof N S Vidhyadhiraja for being such a great host and providing me the opportunity to visit JNCASR.

I would like to thank Ankita Chakrabarti for her help during the initial phase of my PhD. Special thanks to Soumya Sur and Vigneshwaran Kannan for listening to my rants and always being up for interesting physics discussions.

I would also like to thank Institute of mathematical sciences (IMSc), Homi Bhabha national institue (HBNI) for providing excellent facilities for conducting research. I am particularly grateful to all the staff(teaching and non-teaching) at IMSc for their kindness.

This journey would have been much harder without my close friends Disha, Prince, Pavan, Amit, Surabhi, Nishant, Prateek, Akhil, Toshali who have been there through all the ups and downs. I would like to thank Rohit, Sourav, Sushant, Tirthraj, Manav, Suraj for being a source of joy and fun and rekindling my enthusiasm for Tennis which helped me a lot in the later phase of my PhD.

Last but not the least I would like to thank my family for being supportive.

Prakash

Gopal Prakash

Contents

List of Figures

Synopsis

Strongly correlated quantum materials host a wide variety of phenomenon eg: Kondo effect [4–6], Fractional quantum Hall effect [7], High T_c superconductivity which can not be explained using conventional methods. Example of such materials are Mott insulators [8], Twisted Bilayer graphene [9–14], High T_c superconductors [15]. Typically in these materials, the kinetic energy and potential energy are comparable to each other making them strongly correlated. These effects and the materials cannot be studied using Density functional theory (DFT) [16, 17] or perturbation theory and often call for the development of non-perturbative methods (Analytical and/or Numerical).

A key example of strongly correlated material is high-temperature superconductors, such as cuprates, which exhibit a complex phase diagram featuring antiferromagnetism, superconductivity, pseudogap phase, strange metal, and Fermi liquid phases. The transport properties of the normal state, particularly in the pseudogap and strange metal phases, are of central interest. Strange metals exhibit anomalous transport properties, notably linear-in-temperature resistivity extending from near the superconducting transition temperature (T_c) to very high temperatures. Unlike conventional metals, strange metals do not show resistivity saturation at the Mott-Ioffe-Regel (MIR) limit and exhibit unconventional magnetotransport behavior. In contrast, bad metals, typically found in the underdoped regime, display a similar violation of the MIR limit but lack strict T-linear resistivity at low temperatures. Strange metallicity is not unique to cuprates and is also observed in heavy fermion compounds, twisted bilayer graphene, and organic superconductors, suggesting a common underlying mechanism linked to strong electron correlations. This transport behaviour is non trivial because, in a typical metal, the resistivity is known to be linear at temperatures above $T \approx T_D/5$, where T_D is the Debye temperature and is caused by the scattering of electrons due to phonons. However, below T_D the resistivity has a power law behaviour where the contribution of electron-phonon scattering is T^5 and the electron-electron scattering contributes a T^2 behaviour which can be explained using Fermi Liquid (FL) theory [18]. FL theory relies on the assumption that there is an adiabatic continuity between the non-interacting ground state and the interacting ground state of the system. According to FL theory, the single particle excitations of the system are quasiparticles which behave in exactly same manner as the non-interacting electrons but with renormalized mass and charge.

The resistivity behaviour of clean or conventional metals being linear in temperature at $T >> T_D/5$ is a purely classical phenomenon. It is due to the average displacement of lattice sites at higher temperatures being proportional to T. It is important to distinguish between this classical linearity from a linearity in transport originating purely because of dominant quantum fluctuations.

Hubbard Model

A minimal model description for understanding the interplay of kinetic and potential energy is due to Hubbard, known as Hubbard model [19–21]. The Hubbard Hamiltonian is formulated as follows:

$$H = -t \sum_{\langle ij \rangle, \sigma} (c^\dagger_{i\sigma} c_{j\sigma} + \text{h.c.}) + U \sum_i n_{i\uparrow} n_{i\downarrow} - \mu \sum_{i\sigma} n_{i\sigma}, \tag{1}$$

where $c^\dagger_{i\sigma}$ and $c_{i\sigma}$ are the creation and annihilation operators for an electron with spin σ at site i. The hopping amplitude between nearest-neighbor sites is represented by t, and U indicates the on-site Coulomb repulsion. The electron number operator at site i with spin σ is $n_{i\sigma} = c^\dagger_{i\sigma} c_{i\sigma}$, and μ is the chemical potential. This Hamiltonian effectively captures the competition between electron delocalization, driven by kinetic energy, and localization, driven by on-site repulsion. The balance between these elements leads to various electronic phases such as metallic, Mott insulating, and correlated magnetic states, dependent on the ratio U/t and electron filling n.

In 2D on a bipartite lattice, at half filling the ground state is an antiferromagnetic (AF) insulator for all interaction strengths [22–25] and long range AF order appears. For $U/t << 1$ it is a slater insulator. The magnetic correlation length grows exponentially as temperature decreases. In the strong coupling limit $U/t >> 1$ The half-filled system becomes a Mott insulator due to electron localization. At half-filling, the low-energy physics maps onto the Heisenberg antiferromagnet with an exchange interaction $J = 4t^2/U$. The doped Hubbard model in 2D shows a rich behaviour with respect to various parameters. In the weakly interacting limit mean field studies show that in addition to AF ordering other incommensurate magnetic orders appear [26–28]. Various methods including perturbation expansion [29, 30] and Diagrammatic Monte Carlo give a convincing evidence for superconductivity at weak and moderate-coupling strengths. For the doped Hubbard model, the most natural model that emerges in the limit $U/t >> 1$ is known as $t - J$ model. One of the crucial limits for understanding this model is when $J = 0$ or in other words when $U = \infty$.

In this thesis we try to answer following important questions:

1. Can we understand transport in an extremely correlated Hubbard model [31–34] and can we figure out quantum and classical regimes in terms of two particle correlation functions?

2. Can we define characteristic time and energy scales that differentiate between quantum and classical transport regimes of the model?

3. For a finite U Hubbard model using dynamical mean field theory (DMFT) where charge and spin behave differently, can we find relevant time scales that differentiate between quantum and classical regimes of transport? Is it same or different for charge and spin?

In what follows we employ the terminology of quantum and classical regimes to characterize transport. This distinction is motivated by the relative magnitude of the average energy associated with bosonic fluctuation $\bar{\Omega}(T)$frequency compared to the thermal energy T. When $\bar{\Omega}(T) > T$, the relevant fluctuations are intrinsically quantum and dominate the incoherent regime; conversely, when $\bar{\Omega}(T) < T$, thermal effects prevail and transport crosses over to a classical diffusive form. This criterion is closely related to ideas of quantum critical transport [35] and to phenomenology of strange metals in cuprates and other correlated systems [3]. It also connects to earlier work on transport governed by local fluctuations, such as Shastry's extremely correlated Fermi liquid theory [31, 32].

Temperature-Dependent Transport Regimes and Bosonic Fluctuations in the $U = \infty$ Hubbard Model

For a lattice system with one orbital per site, a general state can be described completely in terms of the orbital states at a site i. This set consists of states $|0\rangle$, $|\sigma\rangle$, $|\bar{\sigma}\rangle$ and $|2\rangle$; namely those with no electron, one electron with spin $\sigma(\uparrow)$ or $\bar{\sigma}(\downarrow)$, and two electrons($\uparrow\downarrow$). The X operators introduced by Hubbard [20] are all the matrix elements in this Hilbert space; e.g. $X_i^{\sigma 0}$ is $|\sigma\rangle\langle 0|$ for states at site i. They are local Fermi like or Bose like field operators (not canonical Fermi or Bose operators), depending on whether they describe change in local electron number by unity (odd numbers in general) or by zero (even numbers in general) (see the book by Ovchinnikov and Val'kov [36] is on the X operators and its application in condensed matter physics). Commutators/anticommutators of X operators at different sites vanish, while for the the same site, they do not. These results are uniquely determined by the definition of X operators. The results of on site commutation/anticommutation are not c numbers as for canonical fermions and bosons, but are X operators.

The X operators obey the commutation relation

$$\left[X_i^{\alpha\beta}, X_j^{\gamma\delta}\right]_{\pm} = \left(X_i^{\alpha\delta}\delta_{\beta\gamma} \pm X_i^{\gamma\beta}\delta_{\delta\alpha}\right)\delta_{ij}, \tag{2}$$

The Hubbard Hamiltonian for the $U = \infty$ scenario where double occupancies are not allowed can be expressed in terms of Hubbard (X) operators with the system's chemical potential denoted as μ is:

$$H = -\mu \sum_{i,\sigma} X_i^{\sigma\sigma} + \sum_{ij} t_{ij} X_i^{\sigma 0} X_j^{0\sigma}, \tag{3}$$

where $X_i^{\sigma\sigma}$ symbolizes the number operator, t_{ij} indicates the element of the electron jumping matrix between the sites i and j, and $X_i^{\sigma 0}$ serves as a creation operator, introducing an electron with spin σ at the site i initially free of electrons.

We develop an equation of motion approach for double-time, retarded Green's function for the fermionic X-operator, defined as

$$G_{ij}^{R\sigma\sigma'}(t,t') = -i\theta(t-t')\left\langle \left[X_i^{0\sigma}(t), X_j^{\sigma' 0}(t')\right]_{+}\right\rangle \equiv \left\langle\left\langle X_i^{0\sigma}(t) \middle| X_j^{\sigma' 0}(t')\right\rangle\right\rangle \tag{4}$$

where $[\ ,\ ]_{+}$ denotes the anticommutator and $\langle ... \rangle$ represents the expectation value in the grand canonical ensemble. The second notation on the right-hand side offers a more concise description of the first term.

We derive the Dyson equation for this Green's function by using equation of motion and the irreducible Green's function approach. We also build an approximation for the Self energy by using decoupling of Fermionic and Bosonic degrees of freedom also known as self-consistent Born approximation (SCBA) [37, 38]. We further use $d = \infty$ limit in which the Dysonian Self energy and the Green's function both become local and we obtain a simple ansatz for the local self energy which is a convolution of Fermionic Green's function and the local bosonic fluctuations contributed by charge and spin degrees of freedom. We also derive the equation of motion for the local bosonic fluctuations. Here is the summary of the self-consistent set of equations that we obtained

- **Dyson Equation**

$$G = G^{MF} + G^{MF}\Sigma G \tag{5}$$

- **Expression for Self energy**

$$\Sigma^{R}(\omega) = -\frac{1}{Q^{2}}\int_{-\infty}^{\infty} \mathrm{d}\epsilon_{1}\mathrm{d}\epsilon_{2}\; \rho_{_G}(\epsilon_{1})\rho_{_D}(\epsilon_{2}) \left(\frac{\tanh\left(\frac{\beta\epsilon_{1}}{2}\right) + \coth\left(\frac{\beta\epsilon_{2}}{2}\right)}{\omega^{+} - \epsilon_{1} - \epsilon_{2}}\right) \tag{6}$$

$$\rho_{_G}(\epsilon_{1}) = -\frac{1}{\pi}\mathrm{Im}G^{R}(\epsilon_{1}),\;\; \rho_{_D}(\epsilon_{2}) = -\frac{1}{\pi}\mathrm{Im}D^{R}(\epsilon_{2}) \tag{7}$$

- **Bosonic Green's function**

$$D^{R}(t,t') = \frac{1}{4}\Big\{-i\theta(t-t')\left\langle [N(t),N(t')]_{-}\right\rangle\Big\} + \frac{3}{4}\Big\{-i\theta(t-t')\left\langle [S^{+}(t),S^{-}(t')]_{-}\right\rangle\Big\} \tag{8}$$

The full self consistency is presented below

Self Consistent set of equations

$$G = G^{MF} + G^{MF}\Sigma G,\; G^{MF}(\omega) = \frac{Q}{\omega - Q\epsilon_{k} + i0^{+}}$$

$$Q = 1 - \frac{n}{2},\, n = \langle N\rangle,\, \epsilon_{k} = -2t\sum_{i=1}^{d}\cos k_{i}$$

$$\chi^{R}(\omega) = \frac{1}{N}\sum_{k}\int\!\!\int d\omega_{1}d\omega_{2}\frac{\rho_{G}(k,\omega_{1})\rho_{G}(k,\omega_{2})v_{k}^{2}}{\omega + \omega_{1} - \omega_{2} + i\eta}\left(n_{F}(\omega_{1}) - n_{F}(\omega_{2})\right)$$

$$\chi^{R}_{N}(\omega) = 2\chi^{R}(\omega) \text{ and } \chi^{R}_{S}(\omega) = \chi^{R}(\omega)$$

$$\chi^{\alpha}_{\gamma}(\omega) = \int_{-\infty}^{\infty}\mathrm{d}\omega'\frac{\{\frac{1+\alpha}{2} + n_{B}(\omega')\}\rho_{_\gamma}(\omega')}{\omega - \omega' + i0^{+}},\, \alpha = \pm$$

$$\left(D^{\alpha}_{_N}(\omega)\right)^{-1} = \alpha\frac{1}{n}\left(\omega - \alpha\frac{\chi^{\alpha}_{_N}(\omega)}{n}\right),\quad \left(D^{\alpha}_{_S}(\omega)\right)^{-1} = \alpha\frac{2}{n}\left(\omega - \alpha\frac{\chi^{\alpha}_{_S}(\omega)}{\frac{n}{2}}\right)$$

$$D^{R}_{\gamma}(\omega) = \sum_{\alpha} D^{\alpha}_{\gamma}(\omega),\; \rho_{_{D_{N/S}}}(\omega) = \sum_{\alpha}\rho^{\alpha}_{_{D_{N/S}}}(\omega)$$

$$\rho_{_{D_{N/S}}}(\omega) = -\rho_{_{D_{N/S}}}(-\omega),\; \rho^{-}_{_{D_{N/S}}}(\omega) = -e^{-\beta\omega}\rho^{+}_{_{D_{N/S}}}(\omega)\,,$$

$$\Sigma^{R}(\omega) = -\frac{1}{Q^{2}}\int_{-\infty}^{\infty} \mathrm{d}\epsilon_{1}\mathrm{d}\epsilon_{2}\; \rho_{_G}(\epsilon_{1})\rho_{_D}(\epsilon_{2}) \left(\frac{\tanh\left(\frac{\beta\epsilon_{1}}{2}\right) + \coth\left(\frac{\beta\epsilon_{2}}{2}\right)}{\omega^{+} - \epsilon_{1} - \epsilon_{2}}\right)$$

where, $\rho_{_G}(\epsilon_{1}) = -\frac{1}{\pi}\mathrm{Im}G^{R}(\epsilon_{1}),\;\; \rho_{_D}(\epsilon_{2}) = -\frac{1}{\pi}\mathrm{Im}D^{R}(\epsilon_{2})$.

The equations listed above are a coupled set of non-linear equations which we solve numerically.

In this study, we investigate the temperature dependence of electrical resistivity at various doping levels within the infinite-U Hubbard model on a Bethe lattice. By solving the self-consistent equations specific to this lattice geometry, we uncover distinct transport regimes, each characterized by dominant scattering mechanisms and their corresponding energy scales. Figure 0.1(a) illustrates how resistivity evolves with temperature across different dopings. We emphasize that the present study deliberately omits superconductivity. While d-wave superconductivity is a central feature of the cuprate phase diagram, our focus here is exclusively on the normal state transport. There are two reasons for this choice: first, single-site DMFT and the X-operator formalism employed here are not capable of capturing d-wave pairing instabilities; second, our primary aim is to understand incoherent metallic behavior once superconductivity is suppressed experimentally. This focus allows us to isolate the role of spin and charge fluctuations in generating strange metallic transport, independent of pairing phenomena.

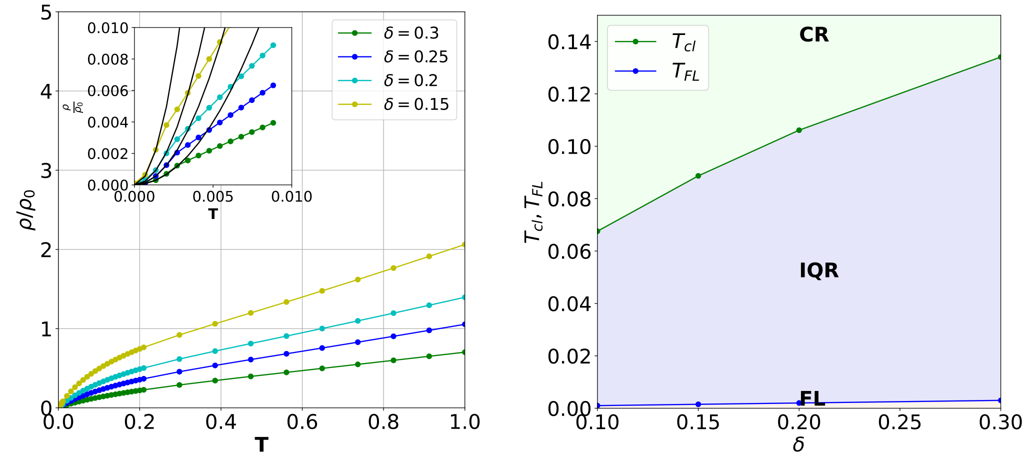

(a)

(b)

Figure 0.1: (a) Temperature dependence of resistivity for several doping levels δ in the unit of $\rho_0(= 1/\sigma_0)$. The inset shows the low-temperature resistivity vs. T, revealing the T^2 behavior with the black line representing the parabolic fit. (b) Different temperature regimes: FL (yellow) for $T < T_{FL}$, incoherent quantum regime (IQR) for $T_{FL} < T < T_{cl}$, and $T > T_{cl}$ a classical regime (CR).

To delineate quantum and classical transport behavior, we introduce the concept of an average bosonic fluctuation energy, denoted $\bar{\Omega}(T)$. This quantity serves as a key diagnostic: the system is said to lie in the quantum regime when $\bar{\Omega}(T) > T$, and in the classical regime when $\bar{\Omega}(T) < T$. The transition between these regimes governs the crossover from Fermi-liquid behavior to incoherent quantum transport and eventually to a classical diffusive regime.

At the lowest temperatures, the system exhibits Fermi-liquid (FL) behavior, marked by a characteristic T^2 increase in resistivity. This regime reflects coherent quasiparticle dynamics mediated by local charge bosons (charge excitations). As temperature increases, the system transitions into the Incoherent Quantum Regime (IQR), where resistivity rises linearly with temperature. Although coherence is lost in this regime, local charge excitations continue to play a significant role in the dynamics.

These regimes are clearly demarcated in Figure 0.1(b). Specifically, the FL regime spans $0 < T < T_{\mathrm{FL}}$, beyond which coherent quasiparticle behavior ceases. The intermediate IQR regime, defined by $T_{\mathrm{FL}} < T < T_{\mathrm{cl}}$, exhibits linear resistivity indicative of incoherent quantum processes. For $T > T_{\mathrm{cl}}$, the system enters the classical regime (CR), dominated by thermally induced fluctuations.

To better understand the nature of these crossovers, we analyze the bosonic fluctuation spectrum and extract the average fluctuation energy $\bar{\Omega}(T)$. Figure 0.2(a) compares $\bar{\Omega}(T)$ with the thermal energy T , highlighting the regions where quantum and classical behavior dominate. This comparison allows us to establish a physically meaningful criterion for distinguishing between quantum-coherent, quantum-incoherent, and classical regimes of transport.

Finite-U Hubbard Model: Spin-Charge Separation and Transport from DMFT+NRG

While our analysis of the $U = \infty$ Hubbard model provided valuable insight into transport via local spin and charge fluctuations, the approximations employed treated spin and charge on equal footing. As a result, they could not distinguish the distinct dynamical roles and timescales of spin and charge degrees of freedom, especially across different transport regimes. To address this limitation and to go beyond the infinite-U picture, we studied the finite-U Hubbard model using Dynamical Mean Field Theory (DMFT) with the Numerical Renormalization Group (NRG) as the impurity solver.

This approach allows us to capture real-frequency correlation functions directly, without relying on analytic continuation, and to probe the incoherent transport regime and crossover behavior in both doped and undoped systems. In particular, we focused on extracting dynamical information about spin and charge excitations, aiming to understand their separate contributions to resistivity and their

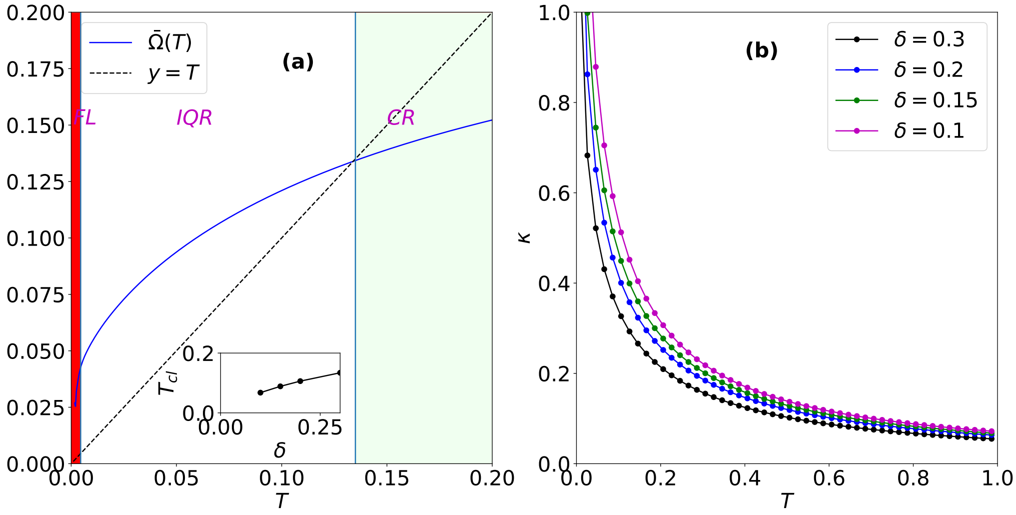

Figure 0.2: (a) The average frequency, denoted as $\bar{\Omega}(T)$, varies with temperature for a doping level of $\delta = 0.3$. In the temperature range $0 < T < 0.005$, represented by a shallow red area, the system exhibits Fermi liquid (FL) behavior. For temperatures in the range of $0.005 < T < T_{cl}(= 0.135)$, the system is within the incoherent Quantum region, crossing over to the classical regime (CR) when $T > T_{cl}$. An inset illustrates the relationship between T_{cl} and doping δ, with a dashed line indicating $Y = T$. (b) shows the charge compressibility, κ, as a function of temperature T for different doping levels.

distinct thermalization pathways. By construction, DMFT becomes exact in the $d = \infty$ limit, where the self-energy is purely local. While this renders it a powerful non-perturbative framework for studying Mott physics and local incoherence, it necessarily neglects non-local spatial correlations. In two-dimensional Hubbard models, such non-local fluctuations are known to be essential for pseudogap formation, short-range antiferromagnetic singlet physics, and superconductivity. As a consequence, our results should be interpreted as capturing the local aspects of strange metallicity and the associated spin/charge decoherence, but not the full richness of 2D physics. Cluster extensions such as DCA/CDMFT or diagrammatic methods can in principle address these issues, though they remain computationally demanding at low temperatures. Thus, while our DMFT results provide a useful baseline for understanding the role of local spin and charge fluctuations, they should be viewed as complementary to, rather than a replacement for, more spatially resolved approaches.

To quantify dissipation, we defined the diffusion spectrum for charge and spin fluctuations as:

$$P_{n/s}(\omega) = \frac{\mathrm{Im}\chi_{n/s}(\omega)}{\pi\omega\chi_{n/s}}$$

,

where $\chi_{n/s}(\omega)$ is the corresponding susceptibility. n represents charge while s represents spin. This spectral function provides a window into how energy is absorbed and dissipated through coupling with local bosonic fluctuations.

We first benchmarked the performance of two common NRG techniques—Density Matrix NRG (DMNRG) and Full Density Matrix NRG (FDM-NRG)—in capturing low-frequency spectral features. As illustrated in Fig. 5.1, DMNRG shows a more reliable low-frequency behavior, whereas FDM-NRG introduces artifacts near $\omega = 0$ at low temperatures. To mitigate this, we adopted a hybrid approach, performing spectral calculations on the Matsubara axis and employing numerical analytic continuation when necessary.

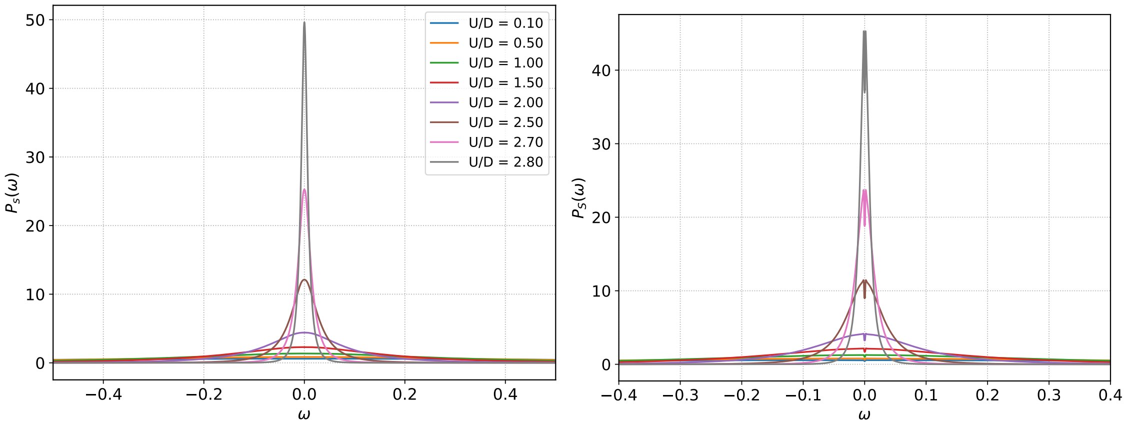

(a) (b)

Figure 0.3: (a) Spin diffusion spectrum for half-filling using DMNRG at $T/D = 0.001$. (b) Spin diffusion spectrum for half-filling using FDM at $T/D = 0.001$.

Quantum-Classical Crossover and Characteristic Frequency Scales

We investigated the transport properties at finite U in the doped Hubbard model (with $U/D = 4$), where the system exhibits a crossover from Fermi-liquid to incoherent transport. To characterize this crossover, we introduced the characteristic frequency scale:

$$\Omega_{n/s} = \int_0^\infty \omega\, P_{n/s}(\omega)\, d\omega,$$

which quantifies the typical energy of charge (n) and spin (s) fluctuations contributing to dissipation.

As shown in Fig. 5.6, the spin degrees of freedom transition to classical behavior at lower temperatures than the charge sector. This suggests that spin fluctuations become incoherent earlier, while charge dynamics remain quantum-mechanical over a broader temperature range. This decoupling is essential in understanding the nature of transport in the intermediate regime, where standard Fermi-liquid theory breaks down.

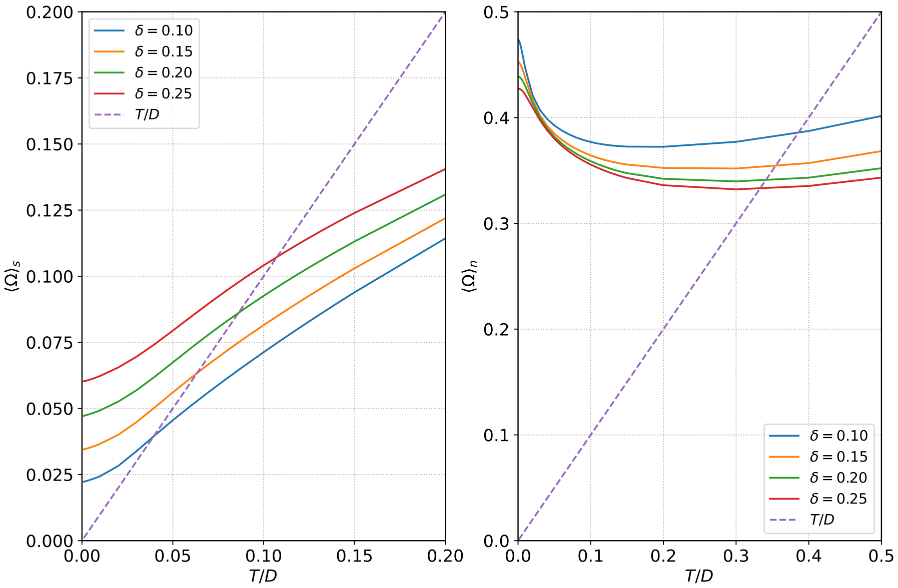

Figure 0.4: Characteristic fluctuation frequencies for spin and charge at U/D $= 4$ for various doping levels $\delta = 0.1,\ 0.15,\ 0.2,\ 0.25$.

Bosonic Fluctuations, Linear Resistivity, and the Two-Stage Breakdown of Fermi Liquid Behavior

The temperature dependence of resistivity for various doping levels at interaction strength $U/D = 4$ is shown in Fig. 0.5. As previously analyzed in detail in [39], the resistivity curve reveals three distinct regimes: a low-temperature Fermi Liquid (FL) phase characterized by T^2 behavior, followed by two successive linear-in- T regimes—a non-Fermi liquid (NFL) phase and a bad metal regime.

Our key insight is that the first linear-in- T regime (NFL) arises from the strong inelastic scattering of charge carriers off dynamically fluctuating, yet unquenched, local magnetic moments. In this regime, spin excitations have already become incoherent, while charge excitations remain quantum-coherent. This partial decoherence results in anomalous transport and linear resistivity—a hallmark of strange metallic behavior.

At higher temperatures, both spin and charge fluctuations become fully incoherent, entering a bad metallic regime. In this regime, quasiparticle coherence is lost entirely, and charge transport becomes increasingly diffusive and classical. The emergence of two separate temperature scales—one for spin decoherence and another for charge—leads to a two-stage breakdown of Fermi liquid behavior. Full quasiparticle coherence is only restored below the Fermi liquid scale T_{FL} , marking the onset of conventional metallic transport.

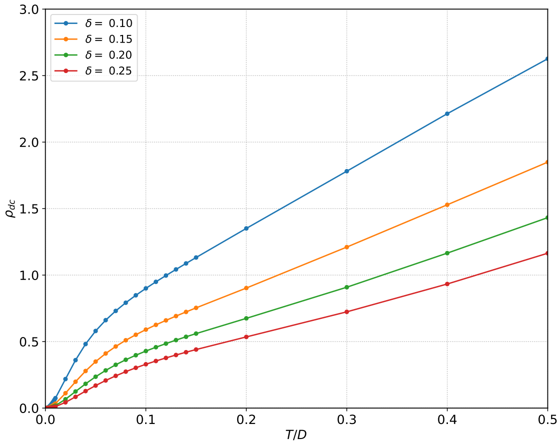

Figure 0.5: Temperature dependence of resistivity at U/D = 4 for different doping levels.

This analysis emphasizes that the interplay and decoupling of spin and charge dynamics are central to understanding transport in strongly correlated systems. The two-stage decoherence process we observe offers a microscopic basis for the emergence of strange metallicity and the bad metal regime in doped Mott systems—phenomena widely observed but still poorly understood in correlated materials.

Chapter 1

Introduction

The study of strongly correlated electron systems has been a central theme in condensed matter physics, offering profound insights into exotic quantum phases and emergent phenomena. These systems host a wide array of exotic quantum phases and emergent collective behavior that defy the expectations of conventional band theory. The hallmark of strongly correlated materials is the energy scale of electron-electron interactions becoming comparable to, or even surpassing, the kinetic energy of electrons [35]. In such regimes, the independent particle picture breaks down, and the system exhibits fundamentally new physics ranging from non-Fermi liquid behavior to unconventional superconductivity and quantum criticality.

Among the most prominent examples of such systems are the high-temperature superconductors, which challenge the conventional Bardeen-Cooper-Schrieffer (BCS) theory [40] and showcase a delicate interplay among spin, charge, orbital, and lattice degrees of freedom. The discovery of cuprate high-T_c superconductors in 1986 [15] revolutionized the field and opened up a host of unresolved questions that remain central to modern condensed matter research. These materials exhibit a remarkably rich phase diagram as a function of hole doping p and temperature T, reflecting their strongly correlated nature.

As shown in Fig. 1.1, the undoped parent compound ($p = 0$) is an antiferromagnetic Mott insulator below the Néel temperature T_N, while it becomes a paramagnetic insulator above T_N. Upon doping, a superconducting dome emerges in the range $p \approx 0.04 - 0.27$, with the critical temperature T_c reaching a maximum at optimal doping p_{opt}. The underdoped region ($p < p_{\text{opt}}$) features a mysterious pseudogap phase [41–60] between T_c and a higher temperature scale T^*, characterized by partial gapping of the Fermi surface and competing electronic orders. The overdoped region ($p > p_{\text{opt}}$) gradually evolves into a more conventional Fermi liquid phase. Sandwiched between these regimes is the enigmatic “strange metal” phase, where the system exhibits linear-in-temperature resistivity, defying the expectations of Fermi liquid theory.

This rich phenomenology emerging from subtle changes in doping or temperature highlights the need for theoretical tools that go beyond mean-field approaches and incorporate strong correlation effects explicitly. Understanding the normal state behavior of cuprates, particularly the pseudogap and strange metal regimes, remains one of the grand challenges in modern physics. It is within this context that the present thesis aims to explore how dynamic correlations; especially spin and charge fluctuations govern the transport behavior in strongly correlated lattice models like the Hubbard model.

Each of the phases depicted in the cuprate phase diagram carries profound physical interest, revealing different aspects of the underlying many-body interactions. Among them, two regimes stand out due to their profound implications and puzzling behaviors: the pseudogap phase and the so-called strange metal or non-Fermi liquid phase. These are regions where conventional quasiparticle-based descriptions fail and where strong correlations manifest in strikingly anomalous experimental signatures. The pseudogap phase for instance, is marked by the suppression of electronic states at the Fermi level without the onset of long-range order, suggesting the presence of competing or preformed orders. Meanwhile, the strange metal region exhibits transport properties that violate the expectations of Fermi liquid theory, such as linear-in-temperature resistivity persisting down to the lowest accessible temperatures.

Understanding these anomalous normal-state properties is not merely a matter of academic curiosity, it is a crucial step toward uncovering the mechanisms behind high-T_c superconductivity itself. In this thesis, our focus will be primarily on the normal (non-superconducting) state of these materials, especially the temperature and doping regimes where standard metallic behavior gives way to incoherent transport and scale-invariant dynamics. By investigating transport phenomena in this regime, we aim to shed light on how dynamical charge and spin fluctuations; hallmarks of strong correlation affect the resistivity and the breakdown of coherent quasiparticle motion.

To frame our investigation, we begin by summarizing the experimental features of the resistivity in hole-doped cuprates, particularly in the underdoped and overdoped regimes. These are illustrated in Fig.1.1, which shows the temperature-doping phase diagram of a typical high-T_c cuprate, and Fig.1.2, which captures the doping dependence of resistivity and its deviation from conventional behavior.

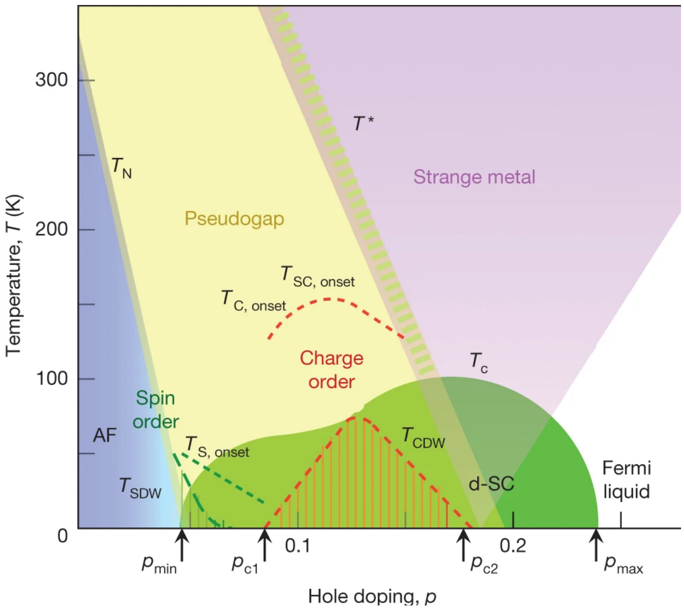

Figure 1.1: Phase diagram of a hole doped cuprate [1]

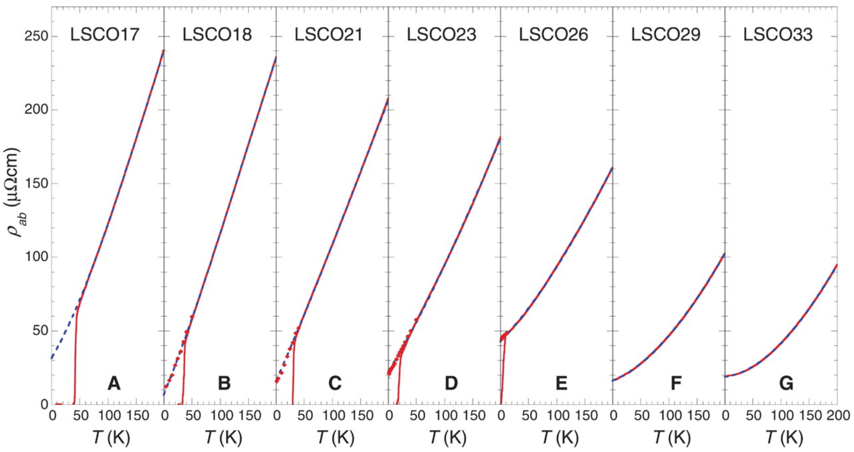

Figure 1.2: Resistivity in a hole doped cuprate LSCO; the labels for example LSCO17 denote that the hole concentration is 0.17 [2].

1.1 Strange and Bad Metals

In conventional metals, the temperature dependence of resistivity is well understood within the framework of Fermi liquid theory. At high temperatures—typically above $T \gtrsim T_D/5$, where T_D is the Debye temperature—resistivity increases linearly with temperature due to electron-phonon scattering [61]. At lower temperatures, resistivity follows a power-law behavior: the phonon contribution scales as T^5, and electron-electron interactions contribute a T^2 term. This T^2 scaling is one of the hallmarks of a Fermi liquid (FL), a paradigm that rests on the notion of long-lived quasiparticles—renormalized electrons that interact weakly and carry charge and spin like bare electrons.

However, many strongly correlated systems, especially hole-doped cuprates exhibit dramatic departures from this behavior [62–65]. In these materials, the resistivity often remains linear in temperature over a wide range, extending from just above the superconducting critical temperature T_c to temperatures well above room temperature. This linearity persists even as the magnitude of the resistivity exceeds the Mott-Ioffe-Regel (MIR) limit, the scale at which the electronic mean free path becomes comparable to the lattice spacing and the notion of quasiparticles loses its meaning [66–68].

This anomalous regime, commonly referred to as the strange metal phase, defies the foundational assumptions of Fermi liquid theory. In particular, the linear-in-T resistivity does not appear to arise from phonons, nor does it saturate at high temperatures as conventional theory would predict. In fact, in experiments where superconductivity is suppressed either by chemical means or by applying a strong magnetic field—resistivity remains linear down to the lowest measured temperatures. An example of this behavior is shown in Fig. 1.3, where the in-plane resistivity of LSCO at doping $p = 0.21$ is linear across a wide temperature range, and the zero-field extrapolated resistivity at low T continues this trend [3].

Moreover, the strange metal exhibits other transport anomalies: the inverse Hall angle follows a T^2 dependence [69], the transverse magnetoresistance violates the conventional Kohler's rule [70], and different transport coefficients seem to be governed by distinct scattering times. These observations have led to the hypothesis of multiple relaxation rates, a concept that challenges the single-quasiparticle lifetime picture of the Fermi liquid.

Another related but distinct category is that of bad metals. These are systems, often in the underdoped region of the phase diagram, where the resistivity exceeds the MIR limit but does not remain linear down to low temperatures. Instead, the resistivity shows a tendency to saturate or deviate from linearity at low T.

Though less exotic than strange metals, bad metals still lie outside the Fermi liquid framework and hint at incoherent transport, where electrons are strongly scattered and no well-defined quasiparticles exist.

It is also noteworthy that strange metallic behavior is not exclusive to cuprates. It has been observed in a wide range of strongly correlated systems, including heavy fermion materials, organic conductors, and more recently, in moiré systems such as twisted bilayer graphene [13, 14, 71]. This universality suggests that strange metallicity may represent a broader class of quantum critical or entangled matter, in which the standard quasiparticle-based picture of electronic transport breaks down entirely.

These experimental observations motivate a deeper theoretical investigation into the mechanisms behind anomalous transport. In particular, one must go beyond single-particle descriptions and focus on the role of many-body correlation effects—especially dynamical fluctuations of spin and charge—as key drivers of incoherence. In this thesis, we aim to approach these questions through the lens of minimal yet non-perturbative models of strong correlation, starting with the Hubbard model, which captures the essential physics of electron-electron interactions.

Survey of theoretical approaches on strange metals

There is a vast amount of literature on various approaches to understand the strange metallicity. In this section, we summarize a few of these approaches. One of the most successful phenomenological approaches that explains various anomalous properties of strange metals is Marginal Fermi Liquid (MFL) theory [72, 73]. MFL proposes the scattering of electrons with specific kind of bosonic fluctuations with spectral function which are momentum independent and are proportional to ω/T for $|\omega| < T$ and are constant otherwise. This spectral form implies a fermionic self-energy with $\mathrm{Im}\Sigma(\omega, T) \propto \max(|\omega|, T)$. The resulting scattering rate is linear in temperature, yielding resistivity $\rho(T) \propto T$. MFL is also able to explain other anomalous properties including specific heat, Raman scattering and optical conductivity. Though MFL is able to explain various anomalies of strange metals, it's a phenomenological theory and a microscopic description of the phenomena is missing. Much of the subsequent theoretical literature on strange metals can be viewed as attempts to embed the MFL phenomenology within a controlled microscopic framework.

One of the approaches to build a microscopic theory for strange metals is based on the quantum criticality [74–81]. This approach is inspired by the fact that the strange metals show a linear resistivity with almost no slope change across a

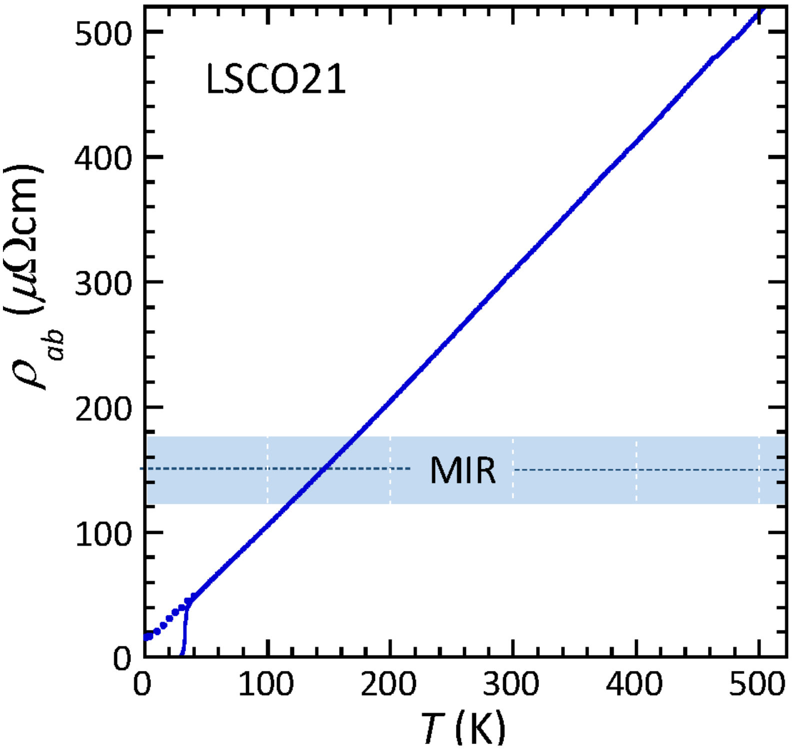

Figure 1.3: Resistivity of LSCO at a doping value of $p = 0.21$ showing a linear behaviour with temperature, the dots at low temperature are obtained by killing superconductivity and then extrapolating the resistivity in the limit $B \to 0$. [3]

wide range of temperature as well as optical and Raman response functions that exhibit universal ω/T scaling [82]. Typically, in this approach fermions are coupled to quantum critical bosonic fluctuations. However, in many of the materials the strange metal behaviour survives for a range of parameters instead of just a critical point. Parallel to Quantum critical point based theories, solvable models have been developed that realize non-Fermi-liquid states with scale invariance. The Sachdev–Ye–Kitaev (SYK) model [83, 84], originally formulated as a set of fermions with random all-to-all interactions, is exactly solvable in the large-N limit. At low energies it exhibits emergent conformal symmetry, a fermionic Green's function with power-law behavior, absence of quasiparticles, and maximal quantum chaos. Though SYK model is zero-dimensional in its original form, it has provided a conceptual laboratory for strange-metal behavior. Extensions to arrays of coupled SYK clusters or to random Yukawa models have generated lattice realizations with finite conductivity, Planckian scattering rates, and in some cases linear-T resistivity [85–91]. While SYK-inspired approaches do not yet map directly onto specific materials, they supply controlled solvable examples of strongly incoherent metallic states, with many parallels to the phenomenology of strange metals.

1.2 The Hubbard Model: A Minimal Framework for Strong Correlation

To understand the rich and often perplexing transport phenomena observed in strange and bad metals, we must turn to microscopic models that explicitly account for strong electron-electron interactions. Among the various theoretical models developed to study correlated electron systems, the Hubbard model stands out as one of the most fundamental and widely used frameworks. It captures the essential competition between kinetic energy, which favors delocalization of electrons, and Coulomb repulsion, which tends to localize them—an interplay that lies at the heart of Mott physics and strange metallicity.

The Hubbard Hamiltonian is given by:

$$H = -t \sum_{\langle ij \rangle, \sigma} (c_{i\sigma}^{\dagger} c_{j\sigma} + \text{h.c.}) + U \sum_{i} n_{i\uparrow} n_{i\downarrow} - \mu \sum_{i\sigma} n_{i\sigma}, \tag{1.1}$$

where:

- t is the nearest-neighbor hopping amplitude, controlling the kinetic energy.
- U is the on-site Coulomb repulsion energy.
- μ is the chemical potential.
- $c_{i\sigma}^{\dagger}(c_{i\sigma})$ is the creation (annihilation) operator for an electron with spin σ at site i .
- $n_{i\sigma} = c_{i\sigma}^{\dagger} c_{i\sigma}$ is the number operator.

A pictorial representation of this model is shown in Fig. 1.4, where electrons hop between neighboring lattice sites and experience a strong penalty U for occupying the same site.

This deceptively simple Hamiltonian encodes a wide array of physical phenomena depending on the filling factor and the interaction strength U/t. At half-filling and in the strong coupling limit ($U \gg t$), the system becomes a Mott insulator—a phase where insulating behavior arises not from band theory, but from the prohibition of double occupancy due to strong Coulomb repulsion. In the weak-coupling limit ($U \ll t$), the system resembles a weakly correlated metal that can be described using conventional Fermi liquid theory.

However, it is in the intermediate coupling regime when $U \sim t$; that the most intriguing and least understood phenomena occur. This is the regime relevant to cuprates and many other strongly correlated materials, where strange metal

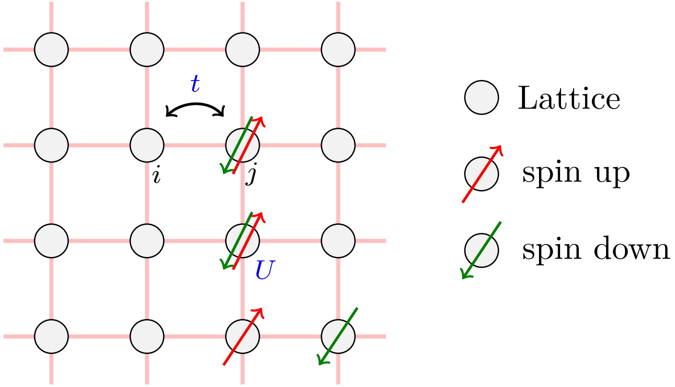

Figure 1.4: Pictorial depiction of the Hubbard model: electrons hop between sites with amplitude t and experience an on-site repulsion U when two occupy the same site.

behavior, pseudogap formation, and unconventional superconductivity emerge. In this regime, the competition between kinetic and potential energy does not permit a simple perturbative treatment, and novel non-quasiparticle dynamics begin to dominate.

Importantly, the Hubbard model also serves as a unifying framework across several dimensions and contexts. In one dimension, it can be solved exactly using the Bethe ansatz, revealing spin-charge separation. In two and three dimensions, it requires sophisticated numerical and analytical techniques such as Dynamical Mean-Field Theory (DMFT), Numerical Renormalization Group (NRG), Density Matrix Renormalization Group (DMRG), and quantum Monte Carlo methods. These tools have uncovered intricate phase diagrams exhibiting Mott transitions, spin and charge ordering, and strange metal behavior.

Beyond equilibrium properties, the Hubbard model has become increasingly central to nonequilibrium and transport studies, especially in the context of ultracold atoms in optical lattices. There, the model can be realized with remarkable control over parameters like U, t, and filling n, providing an experimental testbed for studying Hubbard physics.

In this thesis, we focus on using the Hubbard model as a minimal but powerful tool to investigate normal-state transport in the strange metal regime. In particular, we aim to go beyond single-particle Green's function methods and study how dynamical charge and spin fluctuations—encoded in higher-order correlators—contribute to resistivity and characterize the crossover from coherent to incoherent transport.

The rest of this thesis is devoted to developing, applying, and interpreting methods that allow us to probe these questions within both the infinite-U and finite-U limits of the Hubbard model. We now introduce some of the core theoretical questions that guide this investigation.

Motivating Questions and Scope of this Thesis

Despite its apparent simplicity, the Hubbard model encapsulates the essential complexity of strongly correlated systems. While it successfully reproduces broad features such as Mott insulating states and correlation-induced magnetism, a detailed understanding of its transport properties—particularly in the strange metallic regime—remains elusive. Most existing studies focus on one-particle Green's functions and their associated self-energies. However, many key physical quantities, such as electrical resistivity, spin susceptibility, and charge compressibility, depend crucially on two-particle and higher-order correlation functions. This opens an important and relatively underexplored direction in the theoretical study of correlated systems.

In this thesis, we attempt to address the following central questions:

1. **Can we understand transport in strongly correlated metals through dynamical charge and spin fluctuations?** Instead of focusing solely on single-particle self-energy effects, we explore how collective degrees of freedom—encoded in two-point correlation functions of spin and charge—shape the temperature dependence and qualitative behavior of resistivity in the Hubbard model. Can these fluctuations serve as the effective "scattering mechanism" responsible for linear-in-T resistivity?

2. **Is it possible to identify a quantum-to-classical crossover in transport behavior?** Strongly correlated materials often exhibit non-quasiparticle transport even at intermediate temperatures. Is this incoherence purely quantum in nature, or does it exhibit a crossover to classical behavior dominated by thermally activated fluctuations? We investigate this by analyzing spectral properties and energy scales of spin and charge correlators, and their role in decoherence.

3. **What physical time and energy scales demarcate coherent and incoherent transport regimes?** We aim to extract characteristic scales—such as the Fermi-liquid coherence scale T_{FL}, the effective spin and charge fluctuation bandwidths, and damping rates—that distinguish the low-T coherent Fermi-liquid from the high-T incoherent or diffusive regimes. How do these scales evolve with doping, interaction strength, and dimensionality?

4. **Can one obtain a unified understanding of resistivity from weak to strong coupling?** Existing methods like DMFT and ECFL provide results in either intermediate or strong coupling limits. We ask: how universal are the observed features such as T-linear resistivity, and to what extent can they be connected to charge and spin dynamics? Is there a deeper organizing principle behind the two-slope behavior seen in $\rho(T)$ in both weak and strong correlation regimes?

5. **How do these findings inform our understanding of real materials?** Although this thesis is primarily theoretical, its broader aim is to bridge microscopic modeling with phenomenology observed in materials such as cuprates, heavy fermion systems, and twisted bilayer graphene. Can our results suggest generic mechanisms for bad metallicity, strange transport, and the suppression of quasiparticles near the Mott transition?

These questions motivate the structure of this thesis and shape its methodology: combining analytical insight with numerical computation, emphasizing physical observables, and developing self-consistent frameworks that go beyond the one-particle picture. The answers we obtain—partial though they may be—offer a step toward unraveling the rich and often enigmatic transport behavior in the strongly correlated quantum matter.

In this thesis, we use the terms quantum and classical transport in a specific technical sense that goes beyond the colloquial meaning. The distinction is not simply between the real and imaginary parts of the response function, which are always related by Kramers–Kronig and thus not independent. Rather, our usage is based on a comparison between the characteristic fluctuation frequency scale, $\Omega(T)$, and the thermal energy, T. When $\bar{\Omega}(T) > T$, dissipation is governed primarily by intrinsically quantum fluctuations, and we refer to the regime as quantum. Conversely, when $\bar{\Omega}(T) < T$, thermal fluctuations dominate and transport acquires a classical character, even though the underlying system remains quantum-mechanical. This operational definition allows us to meaningfully distinguish between regimes of incoherent quantum transport and thermally dominated classical diffusion. Importantly, this usage should not be confused with mean-field or semiclassical approximations: even a quadratic, non-interacting fermionic system remains a quantum system in our terminology, but its transport would be classified as classical once the relevant fluctuation frequencies lie below thermal scales. Thus, our terminology emphasizes the dominant source of fluctuations driving dissipation, not the fundamental quantum or classical nature of the microscopic degrees of freedom.

1.3 Outline of Chapters

This thesis is organized to gradually build a coherent narrative, starting from the fundamental principles of linear response theory to the development of advanced theoretical techniques for investigating transport in strongly correlated systems. Each chapter is designed to address specific aspects of the overarching questions posed in the introduction, with increasing technical depth and specialization.

Chapter 2 lays the theoretical foundation by presenting a comprehensive discussion of linear response theory. This chapter begins with the physical motivation behind correlation functions and response functions, emphasizing their direct connection to measurable quantities in condensed matter experiments such as conductivity, magnetic susceptibility, and optical absorption. We derive the Kubo formula from first principles, using the interaction picture and time-dependent perturbation theory. We then formulate the response function in terms of correlation functions, retarded Green's functions, and spectral representations. This chapter also discusses the fluctuation-dissipation theorem and Kramers-Kronig relations, and includes a detailed application to the electrical conductivity of lattice models via the Peierls substitution. A classical driven, damped harmonic oscillator is also analyzed to build physical intuition about linear response and dissipation. This chapter serves as both a pedagogical introduction and a rigorous reference for the theoretical tools used throughout the thesis.

Chapter 3 is devoted to the infinite-U limit of the Hubbard model, which captures the physics of strongly correlated electrons in the limit where local double occupancy is strictly forbidden. The Hubbard model in this limit is formulated using the Hubbard X-operator formalism, which naturally enforces the constraint of no double occupancy. We construct approximate but physically motivated expressions for the single-particle Green's function and the electronic self-energy, incorporating contributions from local spin and charge fluctuations. The chapter includes a detailed discussion of how transport coefficients such as the electrical resistivity can be expressed in terms of these self-energies, and presents numerical results for resistivity and spectral weight redistribution across the coherence-incoherence crossover.

Chapter 4 shifts the focus to a numerically exact framework by introducing Dynamical Mean-Field Theory (DMFT) and the Numerical Renormalization Group

(NRG). DMFT provides a controlled approximation for high-dimensional systems by mapping the lattice problem onto a self-consistent quantum impurity model. NRG is then introduced as a powerful impurity solver capable of resolving low-energy spectral features with high accuracy. We provide a detailed account of how spectral functions and dynamical correlators are computed using NRG, including comparisons of different broadening schemes and spectral reconstruction techniques. This chapter is essential for understanding the computational machinery used in the subsequent analysis of dynamical two-particle correlations.

Chapter 5 presents the central results of the thesis: a study of spin and charge diffusion in the doped Hubbard model using the combined DMFT+NRG approach. Here, we analyze how the interplay between spin and charge fluctuations governs the coherence-incoherence crossover in electronic transport. By computing the dynamical structure factors and spectral densities of spin and charge operators, we identify characteristic energy scales such as the Fermi-liquid temperature T_{FL}, the fluctuation bandwidths, and relaxation timescales. These quantities are used to demarcate different regimes of transport: coherent quasiparticle transport at low T, an intermediate temperature incoherent regime with T-linear resistivity, and a high-temperature classical diffusive regime. This chapter demonstrates how two-particle correlations—not just single-particle lifetimes—can fundamentally shape transport in strongly correlated metals.

Chapter 6 concludes the thesis by summarizing the key insights gained into the nature of strange metallicity, bad metal behavior, and quantum incoherence. We reflect on the utility and limitations of the methods employed, especially in the context of distinguishing quantum from classical transport regimes. The chapter also outlines several promising future directions, including the extension of our approach to systems with finite U, multiorbital models, finite-dimensional cluster extensions of DMFT, and direct comparisons with experimental observables in cuprates, heavy fermion materials, and moiré systems. These avenues open the door to a more comprehensive understanding of emergent transport phenomena in quantum materials.

Chapter 2

Dynamics, Correlation, and Linear Response

In experimental condensed matter physics, many key observables such as those measured in Angle-Resolved Photoemission Spectroscopy (ARPES) [92, 93], Resonant Inelastic X-ray Scattering (RIXS) [94–96], and inelastic neutron scattering [97] are fundamentally linked to time-dependent correlation functions of quantum operators. These experimental techniques probe the excitation spectrum of a material by measuring its response to energy and momentum transfer. Theoretical interpretation of such data relies on understanding how these excitations emerge from the underlying quantum dynamics.

From a theoretical standpoint, the natural framework for making this connection is linear response theory. The central idea is to analyze how a quantum system initially in equilibrium responds to a weak, time-dependent perturbation. The perturbation is typically coupled to an operator in the Hamiltonian that corresponds to a physical quantity of interest. For example, an external electric field couples to the current operator, while a magnetic field couples to spin or magnetization.

The change in the expectation value of an observable due to this perturbation is linear in the applied field (assuming the field is weak), and is governed by a quantity known as the response function, often denoted $\chi_{AB}(t)$. This function encodes how the expectation value of operator A responds to a perturbation applied via operator B, and is expressed in terms of equilibrium correlation functions. More precisely, it is of the form:

$$\chi_{AB}(t) = -i\theta(t) \langle [A(t), B(0)] \rangle \tag{2.1}$$

where $\theta(t)$ is the Heaviside step function and the expectation value is taken with respect to the unperturbed (equilibrium) state.

In frequency space, the imaginary part of the response function is directly related to the spectral function, which determines the absorption and emission probabilities of the system at a given frequency. This quantity can be inferred from measurements in energy-resolved experiments like ARPES and RIXS. Therefore, the response function acts as a bridge between theoretical models and experimental spectra.

Moreover, the analytic structure of the response function in the complex frequency plane such as the locations of poles and branch cuts contains detailed information about the nature of the excitations. For example, poles correspond to long-lived quasiparticle modes, while branch cuts signal continua of excitations or damping processes. The response function thus reveals the collective behavior of electrons, spin degrees of freedom, and other internal excitations.

Finally, because the response function is computed using equilibrium properties of the unperturbed Hamiltonian, linear response theory allows us to connect the non-equilibrium behavior of the system to its equilibrium statistical mechanics. This provides a powerful and systematic route to interpret a wide range of experimental phenomena using first-principles theoretical models.

In this chapter, we develop the formal structure of linear response theory, beginning with the Kubo formula, followed by its spectral representation, analytic properties, fluctuation-dissipation theorems, and application to transport coefficients such as electrical conductivity.

2.1 Kubo Formula: Linear Response to External Fields

We now proceed to derive the Kubo formula [98], which provides a general framework for computing how an equilibrium quantum system responds to a weak, time-dependent external perturbation. This derivation is carried out using perturbation theory in the interaction picture and results in an explicit expression that relates the induced change in an observable to an equilibrium correlation function of operators.

Suppose the system is governed by a time-independent Hamiltonian H_0 , and we perturb it by a weak external field $h_i(\mathbf{r}, t)$ that couples linearly to an observable $A_i(\mathbf{r})$. The full time-dependent Hamiltonian is then

$$H(t) = H_0 + \int d\mathbf{r} \sum_i h_i(\mathbf{r}, t) A_i(\mathbf{r}),$$

where $A_i(\mathbf{r})$ may correspond to physical quantities like charge density or current, and $h_i(\mathbf{r}, t)$ to external probes such as electric or magnetic fields.

Setup and Notation

Let H_0 denote the equilibrium Hamiltonian of the system, which is assumed to be time-independent and expressed in the grand canonical ensemble. The system is perturbed by a weak, time-dependent external field $h_i(\mathbf{r}, t)$, which couples linearly to a quantum mechanical observable $A_i(\mathbf{r})$. The total Hamiltonian then takes the form

$$H(t) = H_0 + H_1(t), \qquad H_1(t) = \int d\mathbf{r} \sum_i h_i(\mathbf{r}, t) A_i(\mathbf{r}). \tag{2.2}$$

Time Evolution in the Interaction Picture

In quantum mechanics, the expectation value of an observable at time t is given by

$$\langle A_i(\mathbf{r}, t)\rangle = \mathrm{Tr}\left[\rho(t) A_i(\mathbf{r})\right], \tag{2.3}$$

where $\rho(t)$ is the time-dependent density matrix. We assume that the external field is turned on adiabatically and vanishes for $t \to -\infty$. Assuming adiabatic evolution and weak perturbations, we express the density matrix as

$$\rho(t) = \sum_n p_n |\psi_n(t)\rangle\langle\psi_n(t)|, \qquad p_n = \frac{e^{-\beta\epsilon_n}}{Z}, \qquad Z = \sum_n e^{-\beta\epsilon_n}, \tag{2.4}$$

where ϵ_n and $|\psi_n(t)\rangle$ are the eigenvalues and time-evolved eigenstates of the full Hamiltonian $H(t)$, respectively.

To compute $\rho(t)$, it is convenient to work in the interaction picture, where the dynamics due to H_0 is factored out. The states and operators evolve as

$$|\psi_I(t)\rangle = e^{iH_0 t}|\psi_S(t)\rangle, \;\; H_I(t) = e^{iH_0 t} H_1(t) e^{-iH_0 t}, \tag{2.5}$$

where the subscript S denotes the Schrödinger picture and I the interaction picture.

The interaction picture time evolution operator $U_I(t, t_0)$ is defined by

$$|\psi_I(t)\rangle = U_I(t, t_0)|\psi_I(t_0)\rangle, \qquad U_I(t, t_0) = T \exp\left[-i\int_{t_0}^{t} dt' H_I(t')\right], \tag{2.6}$$

with T the time-ordering operator. For weak perturbations, we expand this to first order:

$$U_I(t, -\infty) \approx 1 - i\int_{-\infty}^{t} dt' H_I(t'). \tag{2.7}$$

Using this, we write the density matrix to linear order as

$$\rho(t) = e^{-iH_0 t}U_I(t,-\infty)\ \rho_{eq}\ U_I^\dagger(t,-\infty)e^{iH_0 t}, \qquad \rho_{eq} = \frac{e^{-\beta H_0}}{Z}. \tag{2.8}$$

Inserting Eq. 2.7, we obtain

$$\delta\rho(t) = \rho(t) - \rho_{eq} = -i\int_{-\infty}^{t} dt' e^{-iH_0(t-t')}\left[H_1(t'), \rho_{eq}\right] e^{iH_0(t-t')}. \tag{2.9}$$

Deriving the Response Function

We now compute the change in the expectation value of the observable:

$$\delta\langle A_i(\mathbf{r},t)\rangle = \mathrm{Tr}\left[\delta\rho(t)A_i(\mathbf{r})\right]. \tag{2.10}$$

Using the cyclic property of the trace, this becomes

$$\delta\langle A_i(\mathbf{r},t)\rangle = -i\int_{-\infty}^{t} dt' \int d\mathbf{r}' \sum_j h_j(\mathbf{r}',t')\langle[A_i(\mathbf{r},t), A_j(\mathbf{r}',t')]\rangle_{eq}. \tag{2.11}$$

This is the Kubo formula, written in terms of the equilibrium two-point commutator. It is customary to define the retarded response function:

$$\chi^R_{A_iA_j}(\mathbf{r},t;\mathbf{r}',t') = -i\theta(t-t')\langle[A_i(\mathbf{r},t), A_j(\mathbf{r}',t')]\rangle_{eq}, \tag{2.12}$$

so that the Kubo formula takes the compact form:

$$\delta\langle A_i(\mathbf{r},t)\rangle = \int_{-\infty}^{\infty} dt' \int d\mathbf{r}' \sum_j \chi^R_{A_iA_j}(\mathbf{r},t;\mathbf{r}',t')h_j(\mathbf{r}',t'). \tag{2.13}$$

In frequency space, this becomes

$$\delta\langle A_i(\omega)\rangle = \sum_j \chi^R_{A_iA_j}(\omega)h_j(\omega), \tag{2.14}$$

where the response function $\chi^R_{A_iA_j}(\omega)$ is the Fourier transform of the retarded commutator. To make the notation succinct, we have included the r dependence of the operators and fields in the index i itself $(h_i \equiv h_i(\mathbf{r_i}))$.

This formalism provides a systematic and general method to compute the response of any observable to a weak perturbation, and plays a foundational role in the theoretical analysis of transport coefficients, susceptibilities, and spectral functions.

2.2 Correlation Function and Its Properties

The central object in linear response theory is the *correlation function*, which encodes how different observables in a quantum system are dynamically connected. These correlation functions quantify the intrinsic quantum fluctuations in equilibrium and determine how the system responds to external perturbations. In fact, the entire framework of linear response theory rests on analyzing such equilibrium fluctuations.

We define the correlation function associated with two quantum operators A_i and A_j as the expectation value of their commutator in the Heisenberg picture:

$$\chi''_{A_i A_j}(t,t') = \left\langle \left[A_i(\mathbf{r},t), A_j(\mathbf{r}',t') \right] \right\rangle \tag{2.15}$$

This object, often called the *dissipation function*, governs how energy is exchanged between the external perturbation and the system. The corresponding *retarded response function*, which directly appears in the Kubo formula, is then expressed in terms of χ'' as:

$$\chi^R_{A_i A_j}(t) = -i\theta(t)\chi''_{A_i A_j}(t) \tag{2.16}$$

Here, $\theta(t)$ is the Heaviside step function, enforcing causality: the response occurs only after the perturbation is applied.

Several important properties of $\chi''_{A_i A_j}$ follow from general principles such as time-translation invariance, hermiticity, and the cyclic property of the trace in quantum statistical mechanics. We list them below:

- **Time translation invariance:** If the Hamiltonian H_0 is time-independent, then the system is invariant under time shifts. Hence,

  $$\chi''_{A_i A_j}(t,t') = \chi''_{A_i A_j}(t-t') \tag{2.17}$$

  This means that the correlation function depends only on the time difference, not on the absolute time, reflecting the stationary nature of equilibrium.

- **Antisymmetry and Hermiticity:** Using the cyclic invariance of the trace and the definition of the commutator, one can show that

  $$\chi''_{A_i A_j}(t) = -\chi''_{A_j A_i}(-t) = \left[\chi''_{A_j^\dagger A_i^\dagger}(-t) \right]^* \tag{2.18}$$

  These identities encode fundamental physical properties:

  - The first equality expresses the antisymmetry of the commutator under exchange of operator labels and time reversal.

  - The second equality implies that the correlation function obeys a generalized Hermitian condition.

- **Frequency space relations:** Taking the Fourier transform, we obtain corresponding symmetry relations:

$$\chi''_{A_iA_j}(\omega) = -\chi''_{A_jA_i}(-\omega) \tag{2.19}$$

In particular, when $A_i = A_j$, this implies that the imaginary part of the response function is an odd function of frequency:

$$\chi''_{A_iA_i}(-\omega) = -\chi''_{A_iA_i}(\omega) \tag{2.20}$$

This property is closely related to the fact that dissipation must be odd under time reversal: energy absorption depends on the direction of time flow.

Spectral Representation

The spectral representation provides a powerful way to express the retarded response function $\chi^R_{A_iA_j}(\omega)$ in terms of a spectral density that encodes the excitation structure of the system. Doing a Fourier transform of the retarded correlation function (Eq. 2.16), we obtain

$$\chi^R_{A_iA_j}(\omega) = \int_{-\infty}^{\infty} \frac{d\omega' \, \rho_{A_iA_j}(\omega')}{\omega - \omega' + i\eta}, \tag{2.21}$$

where the spectral function $\rho_{A_iA_j}(\omega)$ is defined as

$$\rho_{A_iA_j}(\omega) = -\frac{1}{\pi}\chi''_{A_iA_j}(\omega) = -\frac{1}{\pi}\mathrm{Im}\,\chi^R_{A_iA_j}(\omega).$$

Eq. 2.21 is known as the spectral representation or Lehmann representation. The spectral function $\rho_{A_iA_j}(\omega)$ contains all the dynamical information about the system's response.

A more explicit expression for $\chi''_{A_iA_j}(\omega)$ can be derived by inserting a complete set of energy eigenstates of the unperturbed Hamiltonian H_0. Let $\{|n\rangle\}$ be the eigenstates with energies $\{\epsilon_n\}$, and define matrix elements $A^i_{nm} = \langle n|\hat{A}_i|m\rangle$. Using the closure relation $\sum_n |n\rangle\langle n| = 1$, we obtain

$$\chi''_{A_iA_j}(\omega) = \frac{\pi}{Z}\sum_{n,m}\left(e^{-\beta\epsilon_n} - e^{-\beta\epsilon_m}\right) A^i_{nm}A^j_{mn}\,\delta(\omega + \epsilon_n - \epsilon_m), \tag{2.22}$$

where $Z = \sum_n e^{-\beta\epsilon_n}$ is the partition function.

This expression shows that the correlation function $\chi''_{A_iA_j}(\omega)$ consists of delta-function peaks located at the transition energies $\omega = \epsilon_m - \epsilon_n$, weighted by the difference of Boltzmann factors. Because it directly reflects the energy absorption or emission associated with transitions between eigenstates, it is often referred to as the spectral function.

Substituting this form of $\chi''_{A_iA_j}(\omega)$ into Eq. 2.21, we obtain the Lehmann representation of the retarded response function in its most explicit form:

$$\chi^R_{A_iA_j}(\omega) = \frac{1}{Z}\sum_{n,m} \frac{e^{-\beta\epsilon_m} - e^{-\beta\epsilon_n}}{\omega + i\eta - (\epsilon_n - \epsilon_m)} A^i_{nm} A^j_{mn}. \tag{2.23}$$

We can define a generalized complex function $\chi_{A_iA_j}(z)$ for complex argument z such that

$$\chi^R_{A_iA_j}(\omega) = \chi_{A_iA_j}(z = \omega + i\eta). \tag{2.24}$$

From this spectral representation, it is evident that the retarded response function is analytic in the upper half of the complex frequency plane. This analyticity is a direct consequence of causality and will play a central role in the derivation of the Kramers-Kronig relations.

Kramers-Kronig Relations and Causality

An important consequence of the analyticity of the retarded response function $\chi^R(\omega)$ in the complex frequency plane is the emergence of the *Kramers-Kronig relations.* These relations connect the real and imaginary parts of $\chi^R(\omega)$, and encode the fundamental constraint of causality: the system cannot respond before a perturbation is applied.

In linear response theory, causality is built into the definition of the retarded response function. Specifically, $\chi^R_{A_iA_j}(t) = 0$ for $t < 0$, implying that its Fourier transform $\chi^R(\omega)$ is analytic in the upper half of the complex ω-plane. This analyticity allows us to apply Cauchy's residue theorem over a contour C enclosing the upper half-plane, as shown in Fig. 2.1. The identity reads:

$$\lim_{\eta\to 0^+} \oint_C \frac{d\omega'}{2\pi i} \frac{\chi^R(\omega')}{\omega' - \omega - i\eta} = \chi^R(\omega), \tag{2.25}$$

which follows from the analyticity of $\chi^R(\omega')$ and the fact that the only singularity inside C is the simple pole at $\omega' = \omega + i\eta$.

Assuming that $\chi^R(\omega') \to 0$ sufficiently fast as $|\omega'| \to \infty$, the contribution from the arc at infinity vanishes. The integral over the real axis then yields the principal

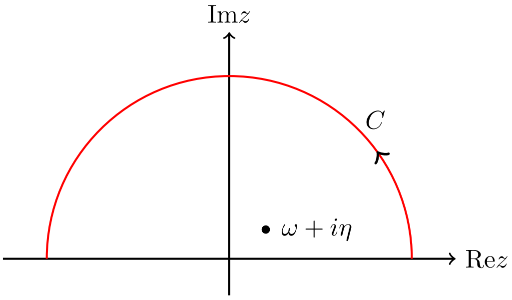

Figure 2.1: Complex ω-plane: the integration contour C encloses the upper half-plane, where $\chi^R(\omega)$ is analytic.

value representation:

$$\mathcal{P}\int_{-\infty}^{\infty}\frac{d\omega'}{\pi}\frac{\chi^R(\omega')}{\omega'-\omega} = i\chi^R(\omega). \tag{2.26}$$

Splitting $\chi^R(\omega)$ into its real and imaginary parts, and comparing both sides of Eq. 2.26, we obtain the **Kramers-Kronig relations**:

$$\mathrm{Re}\chi^R(\omega) = \mathcal{P}\int_{-\infty}^{\infty}\frac{d\omega'}{\pi}\frac{\mathrm{Im}\chi^R(\omega')}{\omega'-\omega}, \tag{2.27}$$

$$\mathrm{Im}\chi^R(\omega) = -\mathcal{P}\int_{-\infty}^{\infty}\frac{d\omega'}{\pi}\frac{\mathrm{Re}\chi^R(\omega')}{\omega'-\omega}. \tag{2.28}$$

These relations show that the real and imaginary parts of the response function are not independent: knowing one over all frequencies determines the other. Physically, this interdependence reflects the principle that the energy absorption (encoded in Imχ^R) and the phase response (encoded in Reχ^R) are two sides of the same causal response.

The Kramers-Kronig relations are indispensable in both theoretical modeling and experimental analysis. In practice, they are used to test the internal consistency of measured optical conductivities, susceptibilities, and other response functions.

Greater and Lesser Correlation Functions

In nonequilibrium and finite-temperature quantum systems, it is often useful to distinguish between different time orderings of operator products. The *greater-than* and *lesser-than* correlation functions capture this time-ordering information and form the foundation of the Keldysh formalism and nonequilibrium Green's function techniques. They also arise naturally in time-resolved spectroscopic measurements, where different physical processes correspond to forward and backward time evolution.

We define the greater and lesser correlation functions between two operators A_i and A_j as

$$C^{>}_{A_iA_j}(t) = \langle A_i(t)A_j \rangle \tag{2.29}$$

$$C^{<}_{A_iA_j}(t) = \langle A_jA_i(t) \rangle\,. \tag{2.30}$$

These functions are generally complex-valued and encode quantum fluctuations in the system. Using time-translation invariance (for time-independent H_0) and cyclicity of the trace, one can derive the following relations:

$$C^{>}_{A_iA_j}(t - i\beta) = C^{<}_{A_iA_j}(t) \tag{2.31}$$

$$C^{>}_{A_iA_j}(-t) = C^{<}_{A_jA_i}(t). \tag{2.32}$$

In frequency space, these imply:

$$C^{>}_{A_iA_j}(\omega) = e^{\beta\omega}C^{<}_{A_iA_j}(\omega) \tag{2.33}$$

$$C^{>}_{A_iA_j}(\omega) = C^{<}_{A_jA_i}(-\omega). \tag{2.34}$$

The dissipative part of the response function (defined in Eq. 2.15) is related to the antisymmetric combination of the greater and lesser correlation functions:

$$\chi''_{A_iA_j}(t) = C^{>}_{A_iA_j}(t) - C^{<}_{A_iA_j}(t) = C^{>}_{A_iA_j}(t) - C^{>}_{A_jA_i}(-t). \tag{2.35}$$

In the frequency domain, this gives:

$$\chi''_{A_iA_j}(\omega) = C^{>}_{A_iA_j}(\omega) - C^{>}_{A_jA_i}(-\omega). \tag{2.36}$$

From these identities, we obtain the **fluctuation-dissipation theorem**, which connects the system's internal quantum fluctuations to its response to external perturbations:

$$C^{>}_{A_iA_j}(\omega) = (1 + n_B(\omega))\chi''_{A_iA_j}(\omega), \quad n_B(\omega) = \frac{1}{e^{\beta\omega} - 1}. \tag{2.37}$$

This relation is of profound physical significance: it shows that the response of a system (encoded in χ'') and its spontaneous fluctuations ($C^{>}$) are not independent. Rather, they are tied by universal statistical principles and temperature.

Plus and Minus Response Functions

To further organize response theory, it is convenient to define two additional functions—often referred to as the *advanced* and *causal* (or *Keldysh*) components.

In our context, we define two time-ordered variants of the response function using the greater and lesser correlators:

$$\chi^{+}(t) = -i\theta(t)C^{>}_{A_iA_j}(t) \tag{2.38}$$

$$\chi^{-}(t) = -i\theta(t)C^{<}_{A_iA_j}(t). \tag{2.39}$$

These obey spectral representations analogous to the retarded function, with their own spectral densities:

$$\rho^{+}(\omega) = -\frac{1}{\pi}C^{>}(\omega), \quad \rho^{-}(\omega) = -\frac{1}{\pi}C^{<}(\omega), \tag{2.40}$$

leading to

$$\chi^{+}_{A_iA_j}(\omega) = \int d\omega' \frac{\rho^{+}_{A_iA_j}(\omega')}{\omega - \omega' + i\eta} \tag{2.41}$$

$$\chi^{-}_{A_iA_j}(\omega) = \int d\omega' \frac{\rho^{-}_{A_iA_j}(\omega')}{\omega - \omega' + i\eta}. \tag{2.42}$$

The spectral functions for $\chi^{\pm}$ are directly related to that of the retarded function via:

$$\rho^{+}(\omega) = \rho(\omega)(1 + n_B(\omega)) \tag{2.43}$$

$$\rho^{-}(\omega) = \rho(\omega)n_B(\omega), \tag{2.44}$$

where $n_B(\omega)$ is the Bose-Einstein distribution. These identities underscore the thermal weighting of excitations and de-excitations in a quantum system and will be crucial in subsequent chapters when we apply linear response formalism to lattice models.

2.3 Kubo Formula for Electrical Conductivity in a Lattice Model

We now apply the machinery developed so far to compute a concrete observable of great experimental relevance; electrical conductivity in the context of a tight-binding lattice model. This application is particularly important for modeling real condensed matter systems where electrons are localized on lattice sites and move through hopping processes.We consider a generic interacting electron system on a two-dimensional square lattice, illustrated in Fig. 2.2.

The Hamiltonian for the system is written as:

$$H = \sum_{ij} t_{ij} c^{\dagger}_{i\sigma} c_{j\sigma} + V, \tag{2.45}$$

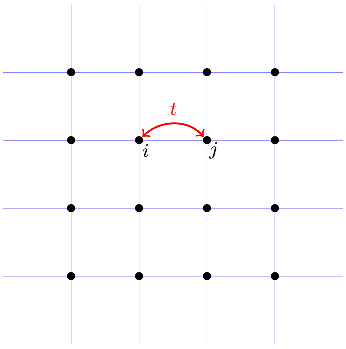

Figure 2.2: A square lattice model of electrons showing hopping between sites i and j, t is the hopping parameter.

where $c^\dagger_{i\sigma}$ creates an electron with spin σ at site i, and V denotes an interaction term (such as Hubbard or longer-range interactions). The canonical anticommutation relation holds:

$$\{c_{i\sigma}, c^\dagger_{j\sigma'}\} = \delta_{ij}\delta_{\sigma\sigma'}. \tag{2.46}$$

To evaluate the electrical conductivity, we must couple the system to an external electromagnetic (EM) field. Treating the EM field classically, we implement the Peierls substitution by minimally coupling the vector potential $\mathbf{A}(\mathbf{r}, t)$ into the hopping term:

$$H[\mathbf{A}] = \sum_{ij} t_{ij} e^{-i\int_i^j \mathbf{A}(\mathbf{r},t)\cdot d\mathbf{r}} c^\dagger_{i\sigma} c_{j\sigma} + V. \tag{2.47}$$

Assuming that $\mathbf{A}(\mathbf{r}, t)$ varies slowly over the lattice spacing, we expand the exponential in powers of $\mathbf{A}$:

$$\int_i^j \mathbf{A}(\mathbf{r}, t) \cdot d\mathbf{r} \approx \sum_{\alpha=1}^{2} \left[A^\alpha(\mathbf{r}_i, t) + A^\alpha(\mathbf{r}_j, t)\right] r^\alpha_{ij}. \tag{2.48}$$

Taking the functional derivative with respect to the vector potential gives the current operator:

$$J^\alpha(\mathbf{r}_i, t) = -\frac{\delta H}{\delta A^\alpha(\mathbf{r}_i, t)}. \tag{2.49}$$

Expanding to linear order in $\mathbf{A}$, the current operator separates into two contributions:

$$\begin{aligned} J^\alpha(\mathbf{r}_i) &= J^\alpha_p(\mathbf{r}_i) + J^\alpha_d(\mathbf{r}_i), \\ J^\alpha_p(\mathbf{r}_i) &= \frac{i}{2}\sum_j t_{ij}\left(c^\dagger_i c_j - c^\dagger_j c_i\right) r^\alpha_{ij}, \\ J^\alpha_d(\mathbf{r}_i) &= \frac{1}{2}\sum_j t_{ij}\left(c^\dagger_i c_j + c^\dagger_j c_i\right)\left[\sum_{\gamma=1}^{2} A^\gamma(\mathbf{r}_i, t) r^\gamma_{ij}\right] r^\alpha_{ij}. \end{aligned} \tag{2.50}$$

Here: - J_p^α is the paramagnetic current, linear in $\mathbf{A}$, and governs the system's dynamic response. - J_d^α is the diamagnetic current, quadratic in $\mathbf{A}$, and contributes only to the static part of the current in equilibrium.

Table 2.1: Comparison of paramagnetic and diamagnetic currents

Component	Expression	Physical Role
Paramagnetic (J_p^α)	$\frac{i}{2}\sum_j t_{ij}(c_i^\dagger c_j - c_j^\dagger c_i) r_{ij}^\alpha$	Time-dependent (dynamical) response
Diamagnetic (J_d^α)	$\frac{1}{2}\sum_j t_{ij}(c_i^\dagger c_j + c_j^\dagger c_i) A^\gamma r_{ij}^\gamma r_{ij}^\alpha$	Static response at equilibrium

In the frequency domain, the total current induced by the vector potential becomes:

$$\langle J^\alpha(\omega)\rangle = \langle J^\alpha\rangle_{eq} + \sum_\beta \chi^R_{J^p_\alpha J^p_\beta}(\omega) A^\beta(\omega), \tag{2.51}$$

where $\chi^R_{J^p_\alpha J^p_\beta}(\omega)$ is the retarded current-current response function. Noting that $\left\langle J_p^\alpha \right\rangle_{eq} = 0$ in equilibrium, we focus on the response due to $\mathbf{A}$.
Using the relation $\mathbf{E}(\omega) = -\partial_t \mathbf{A}(\omega) = i\omega \mathbf{A}(\omega)$, the conductivity tensor $\sigma_{\alpha\beta}(\omega)$ is given by:

$$\langle J^\alpha(\omega)\rangle = \sum_\beta \sigma_{\alpha\beta}(\omega) E_\beta(\omega), \tag{2.52}$$

$$\sigma_{\alpha\beta}(\omega) = \frac{\langle J_d^\alpha\rangle_{eq}\,\delta_{\alpha\beta} + \chi^R_{J^p_\alpha J^p_\beta}(\omega)}{i\omega}. \tag{2.53}$$

This is the Kubo formula for the optical conductivity of a lattice system. It clearly separates the diamagnetic term (from equilibrium expectation of J_d) and the paramagnetic term (from current-current correlations). This expression is fundamental for evaluating charge transport in interacting systems, including applications in DMFT, optical probes, and more.

2.4 Driven, Damped Harmonic Oscillator

To build intuition about the general structure of response functions, we consider a simple yet illustrative example: the classical one-dimensional damped and driven harmonic oscillator. Although this example arises in classical mechanics, the mathematical form of its response function mirrors the structure encountered in quantum systems. In particular, we will see that the real part of the response function corresponds to energy storage, while the imaginary part captures dissipation, a pattern that persists across classical and quantum systems.

The system consists of a particle of mass m subject to a harmonic restoring force $-kx$, a linear damping force $-m\gamma\dot{x}$, and a time-dependent external force $f(t)$. The equation of motion reads:

$$m\frac{d^2x}{dt^2} + m\gamma\frac{dx}{dt} + kx = f(t). \tag{2.54}$$

We define the natural frequency as $\omega_0 = \sqrt{k/m}$. Taking the Fourier transform of both sides gives:

$$x(\omega) = \frac{f(\omega)}{-\omega^2 - i\gamma\omega + \omega_0^2}. \tag{2.55}$$

The linear response function $\chi(\omega)$ is defined as the ratio of the system's response to the applied force:

$$\chi(\omega) = \frac{x(\omega)}{f(\omega)} = \frac{1/m}{-\omega^2 - i\gamma\omega + \omega_0^2}. \tag{2.56}$$

Special cases and interpretation

Undamped oscillator ($\gamma = 0$): The response diverges at the resonance frequencies $\omega = \pm\omega_0$. These are the natural frequencies at which the system oscillates freely, corresponding to the poles of $\chi(\omega)$.

Overdamped regime ($\gamma \gg \omega_0$): In the overdamped limit, we approximate:

$$\chi(\omega) \approx \frac{1/m}{\omega_0^2 - i\gamma\omega}. \tag{2.57}$$

The imaginary part of the response function characterizes dissipation:

$$\frac{\chi''(\omega)}{\omega} = \chi_0\frac{\tau^{-1}}{\omega^2 + \tau^{-2}}, \quad \chi_0 = \frac{1}{m\omega_0^2}, \quad \tau = \frac{\omega_0^2}{\gamma}. \tag{2.58}$$

This quantity is a Lorentzian function centered at $\omega = 0$, with half-width τ^{-1} and total area χ_0. It describes how the system absorbs energy from the drive at different frequencies.

Connection to quantum response functions

The structure of this response function provides valuable insight into the more general quantum theory. In quantum systems, the imaginary part of the response function plays a central role: it determines the spectral function, governs energy absorption, and encodes dissipation. The real part, by contrast, determines the reactive component of the response, reflecting energy storage.

Moreover, the combination $\chi''(\omega)/\omega$ that appears naturally here is directly analogous to the dynamical structure factor in quantum systems, which is experimentally accessible via neutron scattering and RIXS. It also appears in sum rules and fluctuation-dissipation relations. Thus, this classical example serves as a prototype for understanding the frequency-dependent response across both classical and quantum systems.

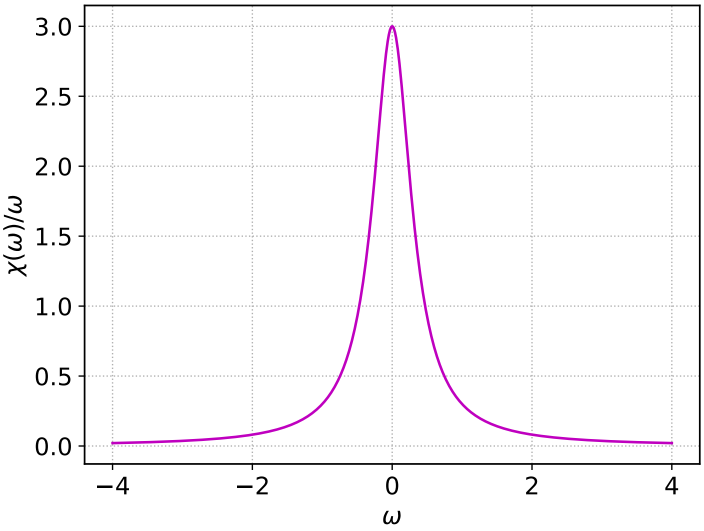

Figure 2.3: Frequency dependence of the dissipation spectrum $\chi''(\omega)/\omega$ for an overdamped oscillator. The peak is centered at $\omega = 0$ with width set by the inverse damping time τ^{-1}.

Chapter 3

Infinite-U Hubbard Model with Local Bosonic Dynamics

3.1 Introduction

Strongly correlated electronic systems form the bedrock of modern condensed matter physics, offering a fertile ground for exotic quantum phenomena that defy the paradigms established by conventional theories. Among these phenomena are high-temperature superconductivity, metallic states lacking well-defined quasiparticles, non-Fermi liquid behavior, and linear-in-temperature resistivity extending over wide thermal ranges. These emergent properties highlight the inadequacy of standard Fermi liquid theory and perturbative techniques, which rely on the adiabatic continuity between non-interacting electrons and quasiparticle excitations. The challenge lies in treating situations where electron-electron interactions are no longer weak perturbations, but dominate the physics entirely.

In Chapter 1, we introduced the Hubbard model as a foundational framework for understanding these systems. In this chapter, we focus on the paradigmatic limit of strong correlation, specifically $U/t = \infty$, where the model becomes analytically tractable and reveals universal features of strongly correlated systems. This limit is referred to as the extremely correlated Fermi liquid (ECFL) regime, as proposed by Shastry [31]. Both the free-electron limit ($U = 0$) and the ECFL limit ($U = \infty$) share a unifying feature: the only control parameter is the carrier density (expressed as the hole doping δ), rendering them suitable baselines for exploring physics across interaction strengths. For finite but large U/t, perturbative corrections in t/U lead to additional complexity, such as magnetically ordered and superconducting phases emerging from virtual double-occupancy processes.

For real materials like the cuprates, ab initio estimates suggest $U \approx 4$ eV and $t \approx 0.4$ eV [99], leading to $U/t \approx 10$, making the $U = \infty$ Hubbard model a physically motivated and analytically meaningful starting point. Over the decades, this limit has inspired a multitude of theoretical frameworks. One line of thought, pioneered by Gutzwiller and later refined by Gebhard [100] and others [101], projects out double occupancy via Gutzwiller-type wavefunctions, yielding non-canonical fermions. Another highly influential route is the Hubbard X-operator formalism [20], extensively developed by Ovchinnikov and Val'kov [36], where local states are represented by a matrix algebra of Fermi-like and Bose-like operators. These approaches go beyond canonical Fermi or Bose algebra, reflecting the intrinsic constraints imposed by strong correlations.

Within the X-operator formalism, Shastry and collaborators have developed the ECFL theory[31, 33, 34] using a Schwinger source approach, drawing inspiration from field-theoretic techniques such as those in Baym-Kadanoff [102] and Tremblay [103]. This method provides a controlled approximation scheme tailored to $U = \infty$, with a consistent treatment of dynamics and thermodynamics. It connects directly with physical observables, offering insights into the interplay between local constraints and collective excitations.

In this work, we adopt a complementary perspective by developing a self-consistent theory based on the equations of motion for the single-particle Green's function G. The theory incorporates the Dysonian self-energy Σ, which is determined by local two-particle correlation functions: specifically, the charge and spin correlators D_N and D_S. These collective modes act as dynamically generated bosonic fields that scatter the fermions, shaping the behavior of the electronic spectral function and transport properties. In the limit of infinite coordination number ($d \to \infty$), we exploit spatial locality to express Σ in terms of simple convolutions of G and D, closing the self-consistent loop.

From this analysis, two major features emerge:

First, at low temperatures, we recover a coherent Fermi liquid regime, where $\mathrm{Im}\Sigma(\omega, T) \propto \omega^2 + \pi^2 T^2$, consistent with exact sum rules and spectral properties. This Fermi liquid, however, is nonperturbative in origin—it emerges from self-consistent feedback between fermionic and bosonic dynamics, not from adiabatic continuity. The coherence temperature $T_{FL} \approx 0.002t$ is quite small, highlighting the fragility of this state in the strongly correlated limit.

Second, as temperature increases beyond T_{FL}, a crossover to an incoherent metallic regime occurs. In this regime, the resistivity becomes linear in T due to scattering off local, thermally populated charge and spin fluctuations. These fluctuations behave like diffusive, massless bosons and possess a temperature-dependent spectrum $\rho_D(\omega)$ with no intrinsic restoring frequency. This absence of a sharp energy scale sets them apart from conventional phonons or magnons. The resistivity remains linear even for $T > T_{cl} = \bar{\Omega}$ (where $\bar{\Omega}$ is the average fluctuation frequency), but with a different slope; reflecting a transition from quantum to classical fluctuation dominated transport.

Thus, the picture that emerges is one of self-generated bosonic modes governing electronic dynamics across temperature scales. These modes originate from the constraints imposed by strong correlations and cannot be modeled as independent or canonical bosons. Instead, they arise from the internal degrees of freedom of the correlated fermionic system itself.

This chapter lays the groundwork for a systematic development of this framework. We now proceed to derive the key equations governing G, Σ, and D, and present a fully self-consistent iterative scheme for computing physical quantities such as spectral functions and transport coefficients.

3.2 Theory

In the introduction chapter of this chapter, we motivated the use of the $U = \infty$ Hubbard model as an analytically controlled limit that captures key features of strongly correlated materials. We now proceed to develop the theoretical framework that forms the core of our original work.

Our primary objective in this chapter is to construct a self-consistent theory for the retarded single-particle Green's function $G^R(\omega)$ in the $U = \infty$ limit, incorporating the dynamical effects of local charge and spin fluctuations via two-particle correlation functions. The formalism we adopt is based on the X-operator representation, which respects the local constraints imposed by strong correlations and naturally accommodates both Fermi- and Bose-like excitations. We employ the equation-of-motion method to derive coupled integral equations for G, the Dysonian self-energy Σ, and the bosonic correlators D_N and D_S, which describe the dynamics of local charge and spin excitations, respectively.

This theory is formulated in the limit of infinite spatial dimensions ($d \to \infty$), where vertex corrections are suppressed and the self-energy becomes purely local. This simplification enables us to express Σ as a convolution of G and D, which is computed iteratively. The coupling between fermionic and bosonic dynamics is at the heart of this approach and leads to several emergent features that characterize the extremely correlated Fermi liquid (ECFL) regime, such as the formation of a narrow Fermi-liquid-like regime at low T and a crossover to incoherent linear-in-T transport at higher temperatures.

We now begin by detailing the Hubbard Hamiltonian in terms of X-operators and formulating the Green's function and its equation of motion. From there, we systematically derive the expressions for Σ, D_N, and D_S, and present the full set of self-consistent equations used in our analysis.

The Hubbard Hamiltonian for the $U = \infty$ scenario, adopting the precise X operator representation for physical quantities as detailed in Appendix A, (assuming energy levels ϵ_1^σ for a single particle state with spin σ and ϵ_0 for the zero particle state are equal (zero), with the system's chemical potential denoted as μ) is:

$$H = -\mu \sum_{i,\sigma} X_i^{\sigma\sigma} + \sum_{ij} t_{ij} X_i^{\sigma 0} X_j^{0\sigma}, \tag{3.1}$$

where $X_i^{\sigma\sigma}$ symbolizes the number operator, t_{ij} indicates the element of the electron jumping matrix between the sites i and j, and $X_i^{\sigma 0}$ serves as a creation operator, introducing an electron with spin σ at the site i initially free of electrons.

The focus is on the double-time, retarded Green's function for the fermionic X-operator, defined as

$$G_{ij}^{R\sigma\sigma'}(t,t') = -i\theta(t-t') \left\langle \left[X_i^{0\sigma}(t), X_j^{\sigma' 0}(t')\right]_+ \right\rangle \equiv \left\langle\left\langle X_i^{0\sigma}(t) \middle| X_j^{\sigma' 0}(t') \right\rangle\right\rangle \tag{3.2}$$

where $[\ ,\ ]_+$ denotes the anticommutator and $\langle ... \rangle$ represents the expectation value in the grand canonical ensemble. The second notation on the right-hand side offers a more concise description of the first term.

To derive $G_{ij}^{R\sigma\sigma'}(t,t')$, we utilize the equation of motion method.[1] The equation of motion for the Green's function defined in equation (3.2) is

$$i\partial_t G_{ij}^{R\sigma\sigma}(t,t') = Q\delta_{ij}\delta(t-t') - \mu G_{ij}^{R\sigma\sigma}(t,t') + Q\sum_l t_{il} G_{lj}^{R\sigma\sigma}(t,t') +^{(\mathrm{ir})} \mathcal{G}_{ij}^{R\sigma\sigma}(t,t'), \tag{3.3}$$

where $Q = \langle B_i^{\sigma\sigma} \rangle = \overline{B_i^{\sigma\sigma}}$ and ${}^{(\mathrm{ir})}\mathcal{G}_{ij}^{R\sigma\sigma}(t,t')$ is a higher-order irreducible Green's function (originating from fluctuations in the Bosonic operator $B_i^{\sigma\sigma'}(t)$) and is detailed as:

$${}^{(\mathrm{ir})}\mathcal{G}_{ij}^{R\sigma\sigma}(t,t') = \left\langle\left\langle [X_i^{0\sigma}(t), H]^{(\mathrm{ir})} | X_j^{\sigma 0}(t') \right\rangle\right\rangle = \left\langle\left\langle [X_i^{0\sigma}(t), H] - \sum_l z_{il} X_l^{0\sigma}(t) | X_j^{\sigma 0}(t') \right\rangle\right\rangle \tag{3.4}$$

The unknown constant z is defined by the condition (or constraint)

$$\langle [X_i^{0\sigma}, H] - \sum_l z_{il} X_l^{0\sigma} | X_j^{\sigma 0} \rangle = \sum_{l\sigma''} t_{il} \left\langle \left[\delta B_i^{\sigma\sigma''}(t) X_l^{0\sigma''}(t), X_j^{\sigma 0}(t)\right]_+ \right\rangle = 0. \tag{3.5}$$

---

[1] Henceforth, we focus on the spin diagonal case $\sigma = \sigma'$, as only this configuration is non-zero for paramagnetic spin isotropic systems with spin quantization along the z axis; additionally, G is independent of σ.

This condition can be thought of in the Mori- Zwanzig memory function language (see e.g. ref.([104]) and the book by Forster ([105]) as related to the 'noise' implied in their Liouvillean operator projection scheme. As elucidated in the appendix A, $B_i^{\sigma\sigma'} = \delta_{\sigma\sigma'} X_i^{00} + X_i^{\sigma'\sigma}$. This represents a local charge operator for $\sigma = \sigma'$ and a local spin flip for $\sigma \neq \sigma'$. The irreducible Green function in terms of the fluctuation operator δB takes the following form:

$$^{(\mathrm{ir})}\mathcal{G}_{ij}(\omega) = \sum_{l\sigma''} t_{il} \left\langle\left\langle \delta B_i^{\sigma\sigma''}(t) X_l^{0\sigma''}(t) \middle| X_j^{\sigma 0}(t') \right\rangle\right\rangle_\omega , \; \delta B_i^{\sigma\sigma'}(t) = B_i^{\sigma\sigma'}(t) - \left\langle B_i^{\sigma\sigma'}(t) \right\rangle . \tag{3.6}$$

The equation of motion, Eq.(3.3), when expressed in frequency space (under equilibrium conditions), transforms to:

$$G_{ij}^R(\omega) = G_{ij}^{R,MF}(\omega) + \sum_l G_{il}^{R,MF}(\omega) \frac{1}{Q} {}^{(\mathrm{ir})}\mathcal{G}_{lj}^R(\omega) \tag{3.7}$$

where the mean-field Green's function $G_{ij}^{R,MF}$ is outlined as:

$$G_{ij}^{R,MF} = \sum e^{ik\cdot(R_i - R_j)} G_k^{R,MF}(\omega) \quad and \quad G_k^{R,MF}(\omega) = \frac{Q}{(\omega + \mu - Q\epsilon_k + i0^+)}, \tag{3.8}$$

Here, $\epsilon(\vec{k}) = -2t \sum_{i=1}^{d} cos k_i$, where d is the dimension of the lattice, and k_i are the components of the wave vector $\mathbf{k}$.
The fluctuation component $^{(\mathrm{ir})}\mathcal{G}_{ij}^{R\sigma\sigma}(\omega)$, obtained through the Fourier transform (FT) of $^{(\mathrm{ir})}\mathcal{G}_{ij}^{R\sigma\sigma}(t - t')$ as defined in equation (3.6), is determined via its equation of motion concerning t'. In frequency space, the resultant expression is as follows:

$$\begin{aligned}(\omega + \mu)^{(\mathrm{ir})}\mathcal{G}_{ij}^{R\sigma\sigma} &= \sum_{l\sigma''} t_{il} \left\langle \left[\delta B_i^{\sigma\sigma''} X_l^{0\sigma''}, X_j^{\sigma 0} \right]_+ \right\rangle + Q \sum_l t_{il} {}^{(\mathrm{ir})}\mathcal{G}_{lj}^{R\sigma\sigma}(\omega) \\ &+ \sum_{ll'\sigma''\sigma'''} t_{l'j} t_{il} \left\langle\left\langle \delta B_i^{\sigma\sigma''}(t) X_l^{0\sigma''}(t) \middle| \delta B_j{}^{\sigma\sigma'''}(t') X_{l'}^{\sigma'''0}(t') \right\rangle\right\rangle_\omega \end{aligned} \tag{3.9}$$

The first term on the right in the above equation vanishes by design Eq.(3.5), as described in the projection operator formalism of Plakida ([37]). After applying a spatial Fourier transform to Eq. (3.9) we obtain:

$$^{(\mathrm{ir})}\mathcal{G}_k^R(\omega) = T_k(\omega) \frac{1}{Q} G_k^{R,MF}(\omega) . \tag{3.10}$$

In this equation, the superscripts $\sigma\sigma$ are omitted, and T is irreducible and identified as a scattering matrix defined by:

$$T_k^{\sigma\sigma}(\omega) = \left(\sum_{ll'\sigma''\sigma'''} t_{l'j} t_{il} \left\langle\left\langle \delta B_i^{\sigma\sigma''}(t) X_l^{0\sigma''}(t) \middle| \delta B_j{}^{\sigma\sigma'''}(t') X_{l'}^{\sigma'''0}(t') \right\rangle\right\rangle_\omega \right)_{FT} . \tag{3.11}$$

Implementing equation (3.10) in equation (3.7) results in an equation for G as:

$$G = G^{MF} + G^{MF}\tilde{T}G^{MF} \text{ , with the scattering matrix } \tilde{T} = \frac{T}{Q^2} \, . \tag{3.12}$$

To define self-energy, one should separate the 'proper' part in the following way.

$$T = \Sigma + \Sigma \, G^{MF} \, T \, . \tag{3.13}$$

where

$$\Sigma_{ij}(\omega) = (T_{ij}(\omega))^{(p)} \tag{3.14}$$

Here, the proper part of the T matrix ($T^{(p)}$) is the portion that cannot be decomposed into simpler parts using any form of decoupling approximation. This equation, expressed in Dyson's form, becomes:

$$G = G^{MF} + G^{MF}\Sigma G, \tag{3.15}$$

The self-energy is ,

$$\begin{aligned} \Sigma_{ij}^{R,\sigma\sigma}(\omega) &= \frac{1}{Q^2} \sum_{ll'\sigma''\sigma'''} t_{l'j} t_{il} \left\langle\left\langle \delta B_i^{\sigma\sigma''}(t) X_l^{0\sigma''}(t) \middle| \delta B_j^{\dagger\,\sigma\sigma'''}(t') X_{l'}^{\sigma'''0}(t') \right\rangle\right\rangle_{\omega}^{(p)} , \\ &= \frac{1}{Q^2} \sum_{ll'\sigma''\sigma'''} t_{l'j} t_{il} \left\langle\left\langle B_i^{\sigma\sigma''}(t) X_l^{0\sigma''}(t) \middle| B_j^{\dagger\,\sigma\sigma'''}(t') X_{l'}^{\sigma'''0}(t') \right\rangle\right\rangle_{\omega} . \end{aligned} \tag{3.16}$$

The self-energy term above, under a Bose-Fermi or DG decoupling is the same as the self-consistent Born approximation (SCBA) discussed by Plakida (see e.g. ref.[37], [38]) or the non-crossing approximation (NCA). This form closely resembles Hubbard's description [21] of the leading 'scattering correction' term or self-energy, extending beyond the mean field term presented in Eq.(3.8).

In the large d approximation, self-energy becomes site local ($i = j$), predominantly influenced by the nearest neighbor $l = l'$ to site i. With the only non-zero hopping term being $t_{il} = t/\sqrt{d}$ (where $t = 1$), the sum of l introduces a factor of d. To calculate the self-energy, a decoupling approximation is applied as follows:

$$\begin{aligned} \Sigma_{ii}^{R,\sigma\sigma}(\omega) = \frac{1}{Q^2} \Bigg[-i\theta(t-t') \Bigg(\sum_{\sigma''} \left\langle B_i^{\sigma\sigma''}(t) B_i^{\dagger\,\sigma\sigma''}(t') \right\rangle \left\langle X_i^{0\sigma''}(t) X_i^{\sigma''0}(t') \right\rangle \\ + \left\langle B_i^{\dagger\,\sigma\sigma''}(t') B_i^{\sigma\sigma''}(t) \right\rangle \left\langle X_i^{\sigma''0}(t') X_i^{0\sigma''}(t) \right\rangle \Bigg) \Bigg]_{\omega} \end{aligned} \tag{3.17}$$

The approximation error in this decoupling is also of relative order $(1/d)$.
Using the spectral representation for the correlation functions specified above and connecting them to the spectral representation of the retarded Green functions, the local self-energy $\Sigma^R(\omega)$ is formulated as:

$$\Sigma^R(\omega) = -\frac{1}{Q^2}\int_{-\infty}^{\infty} \mathrm{d}\epsilon_1 \mathrm{d}\epsilon_2 \; \rho_{_G}(\epsilon_1)\rho_{_D}(\epsilon_2) \left(\frac{\tanh\left(\frac{\beta\epsilon_1}{2}\right) + \coth\left(\frac{\beta\epsilon_2}{2}\right)}{\omega^+ - \epsilon_1 - \epsilon_2} \right) \tag{3.18}$$

$$where,\ \rho_{_G}(\epsilon_1) = -\frac{1}{\pi}\mathrm{Im}G^R(\epsilon_1), \;\; \rho_{_D}(\epsilon_2) = -\frac{1}{\pi}\mathrm{Im}D^R(\epsilon_2) \tag{3.19}$$

$$and,\ D^R(t,t') = \sum_{\sigma''} \left\langle\left\langle B^{\sigma\sigma''}(t) | B^{\dagger^{\sigma\sigma''}}(t') \right\rangle\right\rangle = -i\theta(t-t') \sum_{\sigma''} \left\langle \left[B^{\sigma\sigma''}(t), B^{\dagger^{\sigma\sigma''}}(t') \right]_- \right\rangle . \tag{3.20}$$

D^R, when expressed in terms of the number N and spin S_z operators, is outlined as (refer to Appendix B for details):

$$D^R(t,t') = \frac{1}{4}\Big\{ -i\theta(t-t') \left\langle [N(t), N(t')]_- \right\rangle \Big\} + \frac{3}{4}\Big\{ -i\theta(t-t') \left\langle [S^+(t), S^-(t')]_- \right\rangle \Big\}. \tag{3.21}$$

Given that computing $D^R_{N/S}(\omega)$ through an equation of motion approach is impractical due to the commuting nature of operators, resulting in the disappearance of equal time inhomogeneous terms [106] multiplying the delta function $\delta(t-t')$, alternative strategies are necessary.
We adopt a specific approach to compute these functions. The expression for D^R_N and D^R_S which involves the commutator can be expanded in individual terms of the commutators which we denote by D^+ and D^- below, which involve the product of respective operators and then we set up the equation of motion for D^+ and D^-. The expressions for $D^R_N(t-t') = \langle\langle N(t)|N(t')\rangle\rangle$ and $D^R_S(t-t') = \langle\langle S^+(t)|S^-(t')\rangle\rangle$ are defined as:

$$\begin{aligned} D^R_N(t-t') &= D^+_N(t-t') + D^-_N(t-t') \\ &= -i\theta(t-t')\langle N(t)N(t')\rangle - i\theta(t-t')\langle N(t')N(t)\rangle, \end{aligned} \tag{3.22}$$

$$\begin{aligned} and,\ D^R_S(t-t') &= D^+_S(t-t') + D^-_S(t-t') \\ &= -i\theta(t-t')\langle S^+(t)S^-(t')\rangle - i\theta(t-t')\langle S^-(t')S^+(t)\rangle\,. \end{aligned} \tag{3.23}$$

In the context of spectral functions, the formulation is as follows:

$$D^\alpha_\gamma(\omega) = \int_{-\infty}^{\infty} d\omega' \frac{\rho^\alpha_{_{D_\gamma}}(\omega')}{\omega - \omega' + i0^+} \tag{3.24}$$

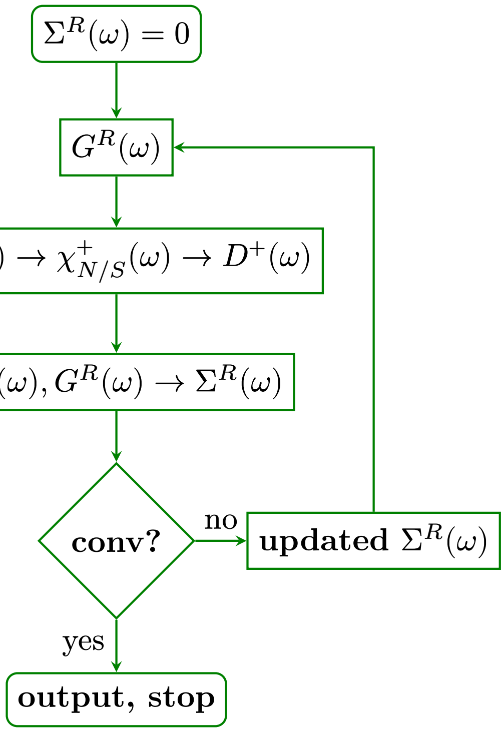

Figure 3.1: Self-consistency loop. This is a schematic illustration of the numerical scheme in which the input $G^R(\omega)$ and the output $G^R(\omega)$ should match for self consistency

where the indices α can take values of $+$ or $-$, and γ represents either N or S. The spectral functions, denoted as $\rho^{\alpha}_{D_\gamma} = -\mathrm{Im}(D^{\alpha}_{\gamma})/\pi$, adhere to the following relationships:

$$D^R_\gamma(\omega) = \sum_\alpha D^\alpha_\gamma(\omega),\ \rho_{D_{N/S}}(\omega) = \sum_\alpha \rho^\alpha_{D_{N/S}}(\omega) \tag{3.25}$$

$$\rho_{D_{N/S}}(\omega) = -\rho_{D_{N/S}}(-\omega),\ \rho^-_{D_{N/S}}(\omega) = -e^{-\beta\omega}\rho^+_{D_{N/S}}(\omega)\,, \tag{3.26}$$

$\rho^\alpha_{D_N}(\omega)$ satisfies the following sum rule:

$$\int_{-\infty}^{\infty} d\omega \rho^\alpha_{D_N}(\omega) = \alpha n \tag{3.27}$$

Following this, an equation of motion method for $D^\alpha_\gamma(\omega)$ is established, paralleling the approach above for $G^R(\omega)$ (This is detailed in Appendix B).
This yields the expressions for $D^\alpha_{N/S}(\omega)$ as:

$$\left(D^\alpha_N(\omega)\right)^{-1} = \alpha\frac{1}{n}\left(\omega - \alpha\frac{\chi^\alpha_N(\omega)}{n}\right)\,,\quad \left(D^\alpha_S(\omega)\right)^{-1} = \alpha\frac{2}{n}\left(\omega - \alpha\frac{\chi^\alpha_S(\omega)}{\frac{n}{2}}\right) \tag{3.28}$$

where $\chi^{\alpha}_{N/S}(\omega)$ is the Fourier transform of the following:

$$\chi^{+}_{S}(t) = -i\theta(t)\left\langle J_s(t)J_s(0)\right\rangle, \quad \chi^{+}_{N}(t) = -i\theta(t)\left\langle J_c(t)J_c(0)\right\rangle \tag{3.29}$$

$$\chi^{-}_{S}(t) = -i\theta(t)\left\langle J_s(0)J_s(t)\right\rangle, \quad \chi^{-}_{N}(t) = -i\theta(t)\left\langle J_c(0)J_c(t)\right\rangle \tag{3.30}$$

Here, J_s and J_c are defined as the spin and charge currents respectively:

$$J_s = \frac{1}{N}\sum_{k} v_k X^{0\sigma}_{k} X^{\bar{\sigma}0}_{k}, \quad J_c = \frac{1}{N}\sum_{k,\sigma} v_k X^{0\sigma}_{k} X^{\sigma 0}_{k} \tag{3.31}$$

where $v_k = \partial_k \epsilon_k$, with ϵ_k being the energy dispersion on the lattice.
The spectral representation for χ^{α}_{γ} is given by:

$$\chi^{\alpha}_{\gamma}(\omega) = \int_{-\infty}^{\infty} \mathrm{d}\omega' \frac{\{\frac{1+\alpha}{2} + n_B(\omega')\}\rho_{\gamma}(\omega')}{\omega - \omega' + i0^{+}} \tag{3.32}$$

$$\textit{where,}\ \ \rho_{\gamma}(\omega') = -\frac{1}{\pi}\mathrm{Im}\chi^{R}_{\gamma}(\omega') \ \ \textit{and,} \quad n_B(\omega') = \frac{1}{e^{\beta\omega'} - 1} \tag{3.33}$$

$\chi^{R}(\omega)$ for both spin and charge sectors is derived from the particle-hole bubble diagram, ignoring vertex corrections, as detailed in [107]. The relationship $\chi^{R}_{N}(\omega) = 2\chi^{R}(\omega)$ and $\chi^{R}_{S}(\omega) = \chi^{R}(\omega)$ is outlined in Appendix C, with the current-current correlation in infinite dimensions ($d = \infty$) described as follows:

$$\chi^{R}(\omega) = \frac{1}{N}\sum_{k}\int\int d\omega_1 d\omega_2 \frac{\rho_G(k,\omega_1)\rho_G(k,\omega_2)v_k^2}{\omega + \omega_1 - \omega_2 + i\eta}\left(n_F(\omega_1) - n_F(\omega_2)\right) \tag{3.34}$$

where $\rho_G(k,\omega) = -\frac{1}{\pi}\mathrm{Im}G^{R}(k,\omega)$ and $n_F(\omega)$ denotes the Fermi function. The calculation of the imaginary part of $\chi^{R}(\omega)$ utilizes the convolution/correlation theorem, with the real part derived from the Kramers-Kronig relation. The adaptation for a Bethe lattice modifies the expression to involve the transport density of states $\Phi(\epsilon)$ [39, 107], leading to a refined calculation of $\mathrm{Im}\chi^{R}(\omega)$ as detailed in the equations.

$$\mathrm{Im}\chi^{R}(\omega) = -\pi \iint \mathrm{d}\epsilon\ \mathrm{d}\omega_1\ \Phi(\epsilon)\rho_G(\epsilon,\omega_1)\rho_G(\epsilon,\omega+\omega_1)\{n_F(\omega_1) - n_F(\omega+\omega_1)\} \tag{3.35}$$

$$\Phi(\epsilon) = \frac{1}{N}\sum_{k} v_k^2 \delta(\epsilon - \epsilon_k) = \Phi_0(4 - \epsilon^2)^{3/2}$$

The process of determining $\Sigma^R, G^R, \chi^R, D^R, D^{\alpha}$, and χ^{α} involves a self-consistent scheme, which can be summarized as follows:

1. **Initialization:**
   Begin with an arbitrary selection of G^R. Using a specific equation (referred to as Eq.(3.35)), compute χ^R based on the initial G^R.

2. **C**omputation of χ^{α} and D^{α}:
   From χ^{R}, calculate χ^{α} using another equation (Eq.(3.32)). This, in turn, allows for the determination of D^{α} through Eq.(3.28).

3. **S**elf-Energy Calculation (Σ^{R}):
   The self-energy, Σ^{R}, is calculated using both D_{γ}^{R} (from Eq.(3.25)) and the initial or previously computed G^{R} (via Eq.(3.18)).

4. **U**pdate of G^{R}:
   With the newly computed Σ^{R}, update the full Green's function, G^{R}, using Eq.(3.15). This updated G^{R} is then used as the starting point for the next iteration of the process.

The cycle repeats, starting from step (1) with the newly obtained G^{R}, and continues until Σ^{R} converges within a specified tolerance. This iterative procedure, known as the self-consistency loop, ensures that the calculations for $\Sigma^{R}, G^{R}, \chi^{R}, D^{R}, D^{\alpha}$, and χ^{α} are mutually consistent and converge to a stable solution. The entire self-consistency loop is illustrated in a figure referred to here as Fig.3.1. Throughout this iterative process, adherence to the sum rule, expressed in Eq.(3.27), is maintained.

To provide a clear and comprehensive understanding of the theoretical framework, we summarize all the equations involved in self-consistency in one place. This allows one to see all the equations at a glance.

Summary of equations used in Self Consistency

$$G = G^{MF} + G^{MF}\Sigma G,\, G^{MF}(\omega) = \frac{Q}{\omega - Q\epsilon_k + i0^+}$$

$$\chi^R(\omega) = \frac{1}{N}\sum_k \int\int d\omega_1 d\omega_2 \frac{\rho_G(k,\omega_1)\rho_G(k,\omega_2)v_k^2}{\omega+\omega_1-\omega_2+i\eta}\left(n_F(\omega_1)-n_F(\omega_2)\right)$$

$$\chi^R_N(\omega) = 2\chi^R(\omega) \text{ and } \chi^R_S(\omega) = \chi^R(\omega)$$

$$\chi^\alpha_\gamma(\omega) = \int_{-\infty}^{\infty} \mathrm{d}\omega' \frac{\{\frac{1+\alpha}{2} + n_B(\omega')\}\rho_\gamma(\omega')}{\omega-\omega'+i0^+}$$

$$\left(D^\alpha_N(\omega)\right)^{-1} = \alpha\frac{1}{n}\left(\omega - \alpha\frac{\chi^\alpha_N(\omega)}{n}\right), \quad \left(D^\alpha_S(\omega)\right)^{-1} = \alpha\frac{2}{n}\left(\omega - \alpha\frac{\chi^\alpha_S(\omega)}{\frac{n}{2}}\right)$$

$$D^R_\gamma(\omega) = \sum_\alpha D^\alpha_\gamma(\omega),\, \rho_{D_{N/S}}(\omega) = \sum_\alpha \rho^\alpha_{D_{N/S}}(\omega)$$

$$\rho_{D_{N/S}}(\omega) = -\rho_{D_{N/S}}(-\omega),\, \rho^-_{D_{N/S}}(\omega) = -e^{-\beta\omega}\rho^+_{D_{N/S}}(\omega)\,,$$

$$\Sigma^R(\omega) = -\frac{1}{Q^2}\int_{-\infty}^{\infty} \mathrm{d}\epsilon_1 \mathrm{d}\epsilon_2\ \rho_G(\epsilon_1)\rho_D(\epsilon_2)\ \left(\frac{\tanh\left(\frac{\beta\epsilon_1}{2}\right) + \coth\left(\frac{\beta\epsilon_2}{2}\right)}{\omega^+ - \epsilon_1 - \epsilon_2}\right)$$

$$\mathrm{w}here,\, \rho_G(\epsilon_1) = -\frac{1}{\pi}\mathrm{Im}G^R(\epsilon_1), \quad \rho_D(\epsilon_2) = -\frac{1}{\pi}\mathrm{Im}D^R(\epsilon_2).$$

Summary of Theoretical Framework

In this section, we have developed a comprehensive and self-consistent formalism for the $U = \infty$ Hubbard model using the X-operator representation and an equation-of-motion approach tailored for large-dimensional lattices. This framework retains the local constraints of strong correlations and naturally incorporates the interplay between fermionic and bosonic degrees of freedom through dynamically generated charge and spin fluctuation correlators. By expressing the Dysonian self-energy $\Sigma^R(\omega)$ as a convolution of the fermionic Green's function $G^R(\omega)$ and bosonic correlators $D^R_{N/S}(\omega)$, we reveal a physical mechanism where local quantum fluctuations govern both spectral and transport phenomena. The inclusion of fluctuation spectra with no intrinsic restoring force leads to novel signatures—such as a non-perturbative Fermi-liquid regime at low temperatures, and a linear-in-T resistivity at higher temperatures due to classical bosonic scattering. The self-consistency loop connecting G^R, Σ^R, χ^R, and D^R captures this interdependence and offers a coherent picture of the emergent metallic state. This theoretical foundation sets the stage for our numerical investigations and physical interpretation of charge dynamics, resistivity scaling, and the crossover between quantum and classical regimes in the extremely correlated Fermi liquid.

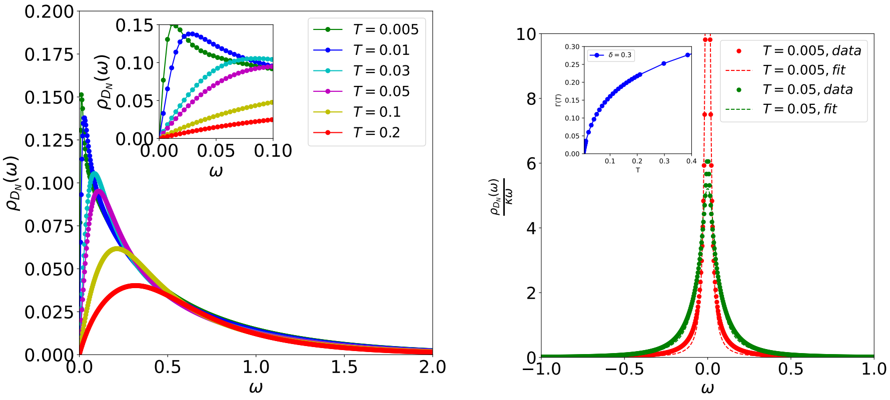

(a) (b)

Figure 3.2: (a) The evolution of $\rho_{D_N}(\omega)$ for positive frequency as a function of temperature for doping $\delta = 0.3$ (b) The normalized charge spectral function, $\frac{\rho_{D_N}(\omega)}{\omega\kappa}$, at a fixed temperatures and its fit with Lorentzian; the inset shows the Lorentzian width, $\Gamma(T)$ vs T at $\delta = 0.3$

3.3 Local Charge, Spin and Current Correlation Functions:

In this Section, we discuss the bosonic correlation functions mentioned above; these determine the electron dynamics of the infinitely strongly correlated metal. In the large d limit, charge and spin correlation functions are identical to within numerical factors having to do with the spin (1/2) of the electron. We therefore discuss here only the charge correlation function. We also discuss here the charge current current correlation function which is the 'self energy' of the charge correlation function, as seen from Equation (3.28). The real frequency spectral density $\rho_{D_N}(\omega)$ of the charge correlation function is shown in Fig 3.2(a) as a function of positive frequency ω for different temperatures T and at doping $\delta = 0.3$. This has the general properties of being real, positive for positive ω and antisymmetric with respect to its sign change.

The local charge fluctuation is a massless damped excitation, as is evident from the general shape of $\rho_{D_N}(\omega)$ (there is no sharp peak corresponding to a mass term or a restoring force ; on the other hand, its spectral density has a smooth structure with a generally broad asymmetric peak and a long tail). The charge at each site diffuses quantum mechanically in a time and temperature dependent manner; there is no net restoring force. Since in the electron phonon system, the best known model of a bosonic system coupled to electrons, the quantum scale is set by the Debye frequency ω_D determined by the nonzero restoring force it is likely that there is no such scale here, and that the occurrence of a small Fermi liquid like regime (section 3.4) is due to a different reason.

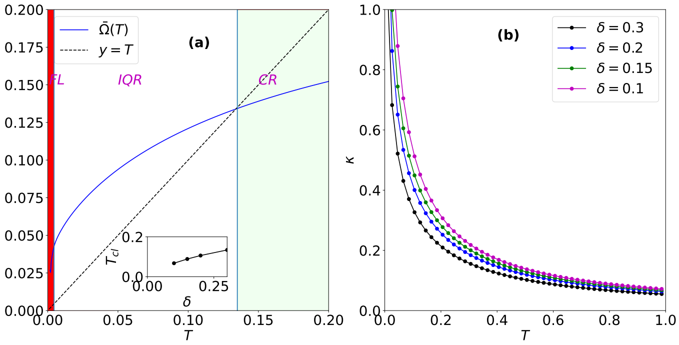

Figure 3.3: (a) The average frequency, denoted as $\bar{\Omega}(T)$, varies with temperature for a doping level of $\delta = 0.3$. In the temperature range $0 < T < 0.005$, represented by a shallow red area, the system exhibits Fermi liquid (FL) behavior. For temperatures in the range of $0.005 < T < T_{cl}(= 0.135)$, the system is within the incoherent Quantum region, crossing over to the classical regime (CR) when $T > T_{cl}$. An inset illustrates the relationship between T_{cl} and doping δ, with a dashed line indicating $Y = T$. (b) shows the charge compressibility, κ, as a function of temperature T for different doping levels.

The very existence of such a distinct bosonic fluctuation coupled to electron dynamics is a strong correlation effect, since it is defined in relation to projected fermion or X operator degrees of freedom whose specific properties are determined by strong correlation. Roughly, the diffusion spectrum Fig 3.2(b) consists of a rising part at low frequencies, a peak, and a long tail. The low frequency rise is less steep as temperature increases, as is the fall. Overall, the spectrum can be fitted roughly by a Lorentzian like form going as $\Gamma/[\omega^2 + \Gamma^2]$ with Γ being the damping constant, as shown in Fig 3.2(b). The actual spectrum decays more rapidly at higher frequencies than this form so that its normalized area is unity, and its first moment is finite. The simplified form is useful since it focuses attention on the quantity Γ (see inset of Fig. 3.2(a)) which is the damping rate of fluctuations. It is small at low temperatures, being roughly proportional to T but larger than it and one has well-defined quasiparticles (a Fermi liquid). We discuss later below the implied quantum and classical regimes in local density fluctuations.

We now infer two consequences of the actual $\rho_{D_N}(\omega)$ shown in Fig 3.2(a), one from the low frequency or quantum end, and another from using its overall spread or first moment which weights strongly the higher frequency or classical regime. At low frequencies $\rho_{D_N}(\omega)$ (ideally above $\omega = 0$, but in reality above a low nonzero value $\omega_l = 0.002t \simeq 8K$ for the large $t = 0.4eV$) is seen to be linear in ω (it is a smooth function and is antisymmetric in ω so that the leading term near $\omega = 0$ has to be linear). As observed from the inset in Fig 3.2(a) for extremely low temperatures, the slope of spectral density $(A(T))$(not shown in the figure) very close to $\omega = 0$ is almost T independent and this gives rise to canonical Fermi Liquid form of $\mathrm{Im}\Sigma(\omega, T)$(we show that this is true analytically in Appendix D). The typical energy scale of $\rho_{D_N}(\omega)$ is the average energy of the local density fluctuations or the first moment

$$\bar{\Omega}(T) = \int_{\omega_l}^{\omega_u} \omega \left(\frac{\rho_{D_N}(\omega)}{\omega\kappa} \right) d\omega \, , \text{ where } \kappa = \int_{-\infty}^{\infty} \left(\frac{\rho_{D_N}(\omega)}{\omega} \right) d\omega \, . \tag{3.36}$$

In the above equation, κ is the thermodynamic compressibility, and the upper frequency limit ω_u of the integral is very large but finite; we use $\omega_u = 30t$.

We show $\bar{\Omega}(T)$ as a function of T in Fig 3.3(a). It is small at low temperatures, roughly proportional to T but larger than it and one has well-defined quasiparticles (a Fermi liquid). As temperature increases, it increases sublinearly with T and essentially flattens out at high temperatures. The case when $\bar{\Omega}(T)$ is lower than the temperature T defines the classical limit for fluctuations. We observe that for $T > 0.13$ for doping $\delta = 0.3$, we enter into the classical regime. Below $T < 0.13$ we are in a quantum regime and we have a coherent Fermi Liquid phase at extremely low temperatures followed by a linear in T resistivity regime (which also lies in the quantum regime) which is denoted by the Incoherent Quantum Regime (IQR).

The quantities $\Gamma(T)$, $A(T)$ (not shown in the figure) and $\bar{\Omega}(T)$ defined above, are different calculated characteristics of the local charge correlation function describing its diffusion and 'stay at home' probability in frequency space. In strongly correlated lattice systems, at 'high' temperatures, quantum mechanical intersite hopping t_{ij} can be neglected, and the system is a statistical superposition of energetically degenerate states with one or no charge at a lattice site. This regime is accessed by experiments on thermopower of strongly correlated metals (see e.g. [108]) and references in the paper ref. [109]). The thermopower, which measures the entropy of charge carriers, is seen to saturate at values consistent with a Heikes-like estimate of the entropy of this classical metal; experimentally, the 'classical' regime begins at surprisingly low temperatures.

The frequency and momentum dependence of charge fluctuations has been recently explored experimentally using momentum-resolved EELS (see e.g. [110]) and RIXS (see e.g. [111]). They do find essentially nondispersive density fluctuations; namely, they are spatially local, as obtained here. In subsequent work, we will present detailed predictions of this spectrum in our theory.

The imaginary part of current-current correlation function, $\mathrm{Im}\chi_N^+(\omega)$, and the real part of the optical conductivity, $\sigma(\omega)$ are defined as:

$$\frac{\sigma(\omega)}{\pi\sigma_0} = \frac{(1 - e^{-\beta\omega})}{\omega} \mathrm{Im}\chi_N^+(\omega) \tag{3.37}$$

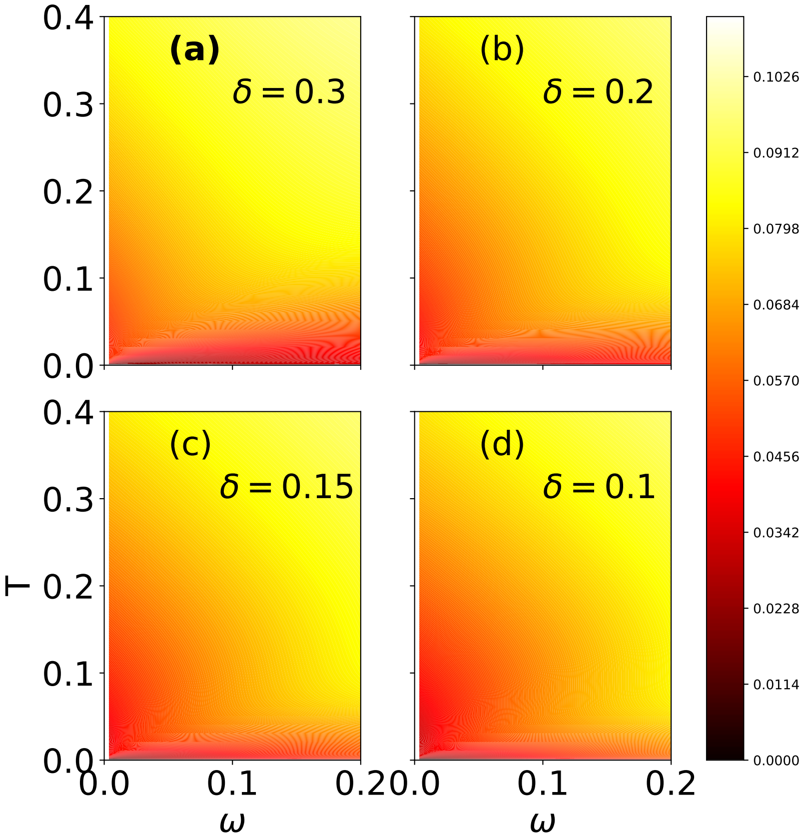

Figure 3.4: Contour plots of imaginary part of current-current correlation function $\mathrm{Im}\chi_N^+(\omega, T)$ for doping values of $\delta = 0.3, 0.2, 0.15, 0.1$.

In this expression, σ_0 can be taken to be of order $\sigma_0 = \frac{a^{2-d}e^2}{\hbar}$, with the lattice spacing a (corresponding in a quasi two-dimensional system to a sheet resistance of one quantum per plaquette). In Fig 3.4, we present contour plots of imaginary part of current-current correlation function $\mathrm{Im}\chi_N^+(\omega)$ for various doping values. The spectra display the following features: (a) For $T < \omega$, $\mathrm{Im}\chi_N^+(\omega)$ varies with ω up to a certain ω and is constant afterwards. (b) For small ω and $T > \omega$, $\mathrm{Im}\chi_N^+(\omega)$ is a constant in temperature. This region of constant $\mathrm{Im}\chi_N^+(\omega)$ reduces as doping is reduced. (c) For high T and small ω, we see another region of constant $\mathrm{Im}\chi_N^+(\omega)$. We conclude that resistivity when $\mathrm{Im}\chi_N^+(\omega)$ is independent of temperature is linear in T. As mentioned above, the region of linear T is large for large doping and starts reducing upon decreasing doping. Our approach finds two regimes of linearity in resistivity, with different slopes, one at intermediate and another at high temperatures. It should also be noted that the Planckian constant is the inverse of $\mathrm{Im}\chi_N^+(\omega)$, and it should be the same for all doping an from our results, it is not exactly one, but is close to it for higher doping but not for lower doping.

3.4 Self Energy and DC Resistivity:

In this Section, we discuss the electron self energy and the intrinsic dc electrical resistivity of the infinitely correlated metal, which is intimately linked with the electron self energy. For instance, the imaginary part of the self-energy, $\mathrm{Im}\Sigma(\omega, T)$, provides insight into the lifetime and coherence of quasiparticles, which are crucial for determining how electrons propagate through a material, and so its resistivity. We also note here (subsection A) that analytically (see Appendix D) the imaginary part of the self-energy, $\mathrm{Im}\Sigma(\omega, T)$, adheres for very low ω and T to the Fermi liquid description, scaling as $(\omega^2 + \pi^2 T^2)$. This is also seen from our self consistent result for $\mathrm{Im}\Sigma(0, T)$. This insight sets the stage for a deeper analysis of how single particle properties change with doping, for both positive and negative excitation energies (particle like and hole like) and at different temperatures. Some of the results are exhibited in Fig 3.5 parts (a) to (d), and insets therein. For example, we show that in the Fermi liquid (very low temperature) regime the quasiparticle residue Z (typically of order 0.1 to 0.2) increases roughly linearly with increasing hole doping. We also plot the local single particle spectral density and see the quasiparticle like low excitation energy peak in it disappearing as temperature increases and the electron system becomes an incoherent liquid of Fermi like excitations.

We next discuss (subsection B) dc resistivity using the well known large d form for the result [107] which neglects vertex corrections. At low temperatures, it is seen to have the classic Fermi liquid form, going as T^2 (in correspondence with the result above for the same region, namely that $\mathrm{Im}\Sigma(\omega, T)$ goes as $\omega^2 + \pi^2 T^2$). It transitions via a long crossover region straddling both the incoherent quantum regime and the 'classical' metal regime (Section 3.3) into linear resistivity behaviour. We also see no signs of resistivity saturation; the resistivity continues to rise linearly with the same slope, beyond the Mott-Ioffe Regel (MIR) quantum limit.

We believe that the defining characteristics of the extremely strongly correlated metal, mentioned above, are due to the influence of local bosonic charge and spin fluctuations which are strongly coupled to electrons. They determine the electron self energy (Section 3.2) and have a sizeable, nearly constant, strength over a large frequency region at most temperatures.

Scattering Rate and Local Bosonic Correlation Functions

In Figure 3.5(a), start going into the details of $-\mathrm{Im}\Sigma(\omega)$, examining how it varies with frequency (ω) across diverse doping levels at a notably low temperature of $T = 0.005$. This analysis uncovers a fascinating transition in behavior around

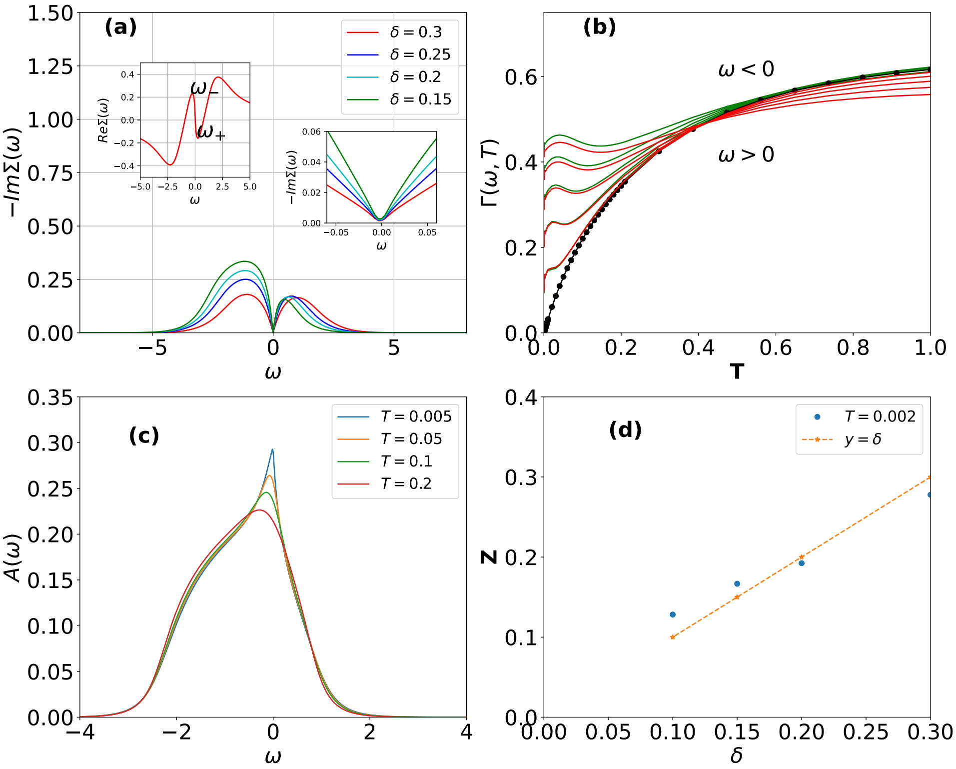

Figure 3.5: (a) $-\mathrm{Im}\Sigma(\omega)$ at $T = 0.005$ for various doping levels. The left inset shows $\Re\Sigma(\omega)$, linear in ω for $\omega_- < \omega < \omega_+$. The right inset is $-\mathrm{Im}\Sigma(\omega)$ near $\omega = 0$ showing ω^2 behavior . (b) $-\mathrm{Im}\Sigma(\omega_c, T)$ versus T at $\delta = 0.2$ for $\omega_c = -0.5, -0.4, ..., -0.1$ (green), $\omega_c = 0.0$ (thick black), and $\omega_c = 0.1, 0.2, ..., 0.5$ (red). (c) Spectral function at doping $\delta = 0.2$ at various temperatures. (d) Variation of Quasiparticle weight with doping at $T = 0.002$.

$\omega = 0$, where the pattern evolves from square-like to linear. Such a transformation underscores the pivotal role of local charge dynamics in modulating electron scattering processes. Interestingly, when comparing the degree of particle-hole asymmetry in our findings with those obtained from Dynamical Mean Field Theory (DMFT) and Shastry's work, ours exhibit a lesser asymmetry. Furthermore, within the same graphical representation, we shift our focus to the real component of the self-energy, $\mathrm{Re}\Sigma(\omega)$. Here, we identify a linear section extending between two critical points, ω_- and ω_+, with the latter's value notably adjusting in response to variation in doping levels.

Venturing into Figure 3.5(b), our exploration extends to the imaginary component of self-energy at a specific frequency, evaluated as a function of temperature. This provides insight into the behavior of the scattering rate under finite frequencies. Notably, for hole-like excitations (where $\omega < 0$), the scattering rate consistently exceeds that of electron-like excitations (where $\omega > 0$). As temperature increases, the relationship between $\mathrm{Im}\Sigma$ and T for various positive frequencies unveils a cross-

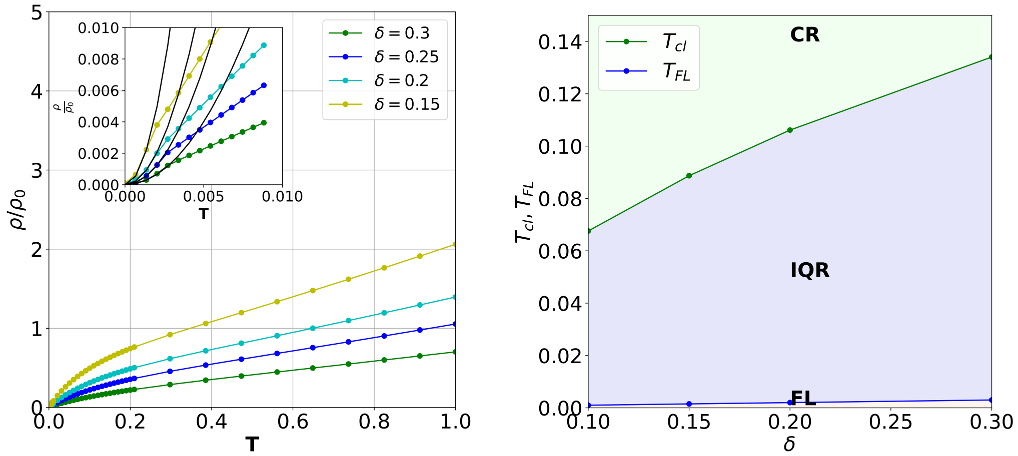

(a)

(b)

Figure 3.6: (a) Temperature dependence of resistivity for several doping levels δ in the unit of $\rho_0(= 1/\sigma_0)$. The inset shows the low-temperature resistivity vs. T, revealing the T^2 behavior with the black line representing the parabolic fit. (b) Different temperature regimes: FL (yellow) for $T < T_{FL}$, incoherent quantum regime (IQR) for $T_{FL} < T < T_{cl}$, and $T > T_{cl}$ a classical regime (CR).

ing threshold. Beyond it, the scattering rate inversely correlates with frequency, implying that at higher temperatures, low-energy, electron-like excitations with finite positive ω values enjoy longer lifespans compared to those precisely at $\omega = 0$. While the overall trends are the same as DMFT predictions, some of our findings differ; for example, the $\Gamma(\omega, T)$ crossing is at much larger values of ω and T.

In Figure 3.5(c), the progression of the spectral function with varying temperatures is presented, focusing specifically on a doping level of $\delta = 0.2$. This visualization allows us to observe how temperature influences the spectral features, revealing important insights into the decoherence effects on the electronic structure at this particular level of doping. On the other hand, Figure 3.5(d) is dedicated to illustrating the behavior of the quasi-particle residue across a range of doping levels at a particular low temperature (T$= 0.002$) where the system is a Fermi liquid. This aspect of the study sheds light on the correlation between doping concentration and the quasi-particle strength, elucidating how the electronic properties of the system evolve with changes in doping.

DC Resistivity and the Influence of Local Bosonic Correlation Functions

In Figure 3.6(a), we exhibit the relationship between resistivity (ρ) and temperature (T) for various levels of doping. At the lowest temperatures, the system demonstrates typical Fermi-liquid behavior, characterized by a quadratic increase in resistivity with temperature. This trend is clearly depicted in the inset of Figure 3.6(a), in which the low temperature region is shown, enlarged, illustrating the coherent interactions among particles. These interactions are mediated by local charge bosons (charge excitations), which play a critical role in the coherent Fermi liquid like resistivity behaviour of the the system at low temperatures as well. As temperature increases, crossing into the Incoherent Quantum Regime (IQR), we observe a linear rise in resistivity. This change signals a crossover from coherent to incoherent or chaotic behavior, despite the continued influence of local charge excitations on the system's dynamics.

Analyzing the resistivity outcomes more closely, we distinguish three separate temperature domains as outlined in the data: $0 < T < T_{FL}$, where T_{FL} signifies the temperature boundary above which Fermi-liquid behavior is no longer observed; $T_{FL} < T < T_{IQR}$, marking the range within the Incoherent Quantum Regime characterized by a linear increase in resistivity; and $T > T_{cl}$, representing temperatures beyond which the system exhibits incoherent behavior (see Section 2). These domains are graphically represented as functions of doping in Figure 3.6(b), where the temperature thresholds T_{FL} and T_{cl} are plotted against doping levels. It's observed that T_{FL} changes linearly with doping, indicating a direct correlation between doping levels and the Fermi-liquid to non-Fermi-liquid crossover temperature. In contrast, the variation of T_{cl} with doping does not follow a simple linear pattern, underscoring the complex interplay between doping and the material's crossover to incoherent electronic states.

This extensive exploration into self-energy, electron scattering, and resistivity, all through the lens of local charge excitations, uncovers the complex dynamics in extremely correlated electron systems. Its impact is seen to vary in a characteristic way with temperature, frequency, and doping on electron behavior, crossing over from coherent to incoherent or chaotic states, and presents a thorough framework for comprehending the diverse phenomena observed in these complex materials, centering around the role of local charge excitations.

3.5 Strengths and Limitations of our Method

The method developed in this chapter tries to present a physical picture of transport in $U = \infty$ Hubbard model through explicit coupling of boson like excitations of the system with the fermionic degrees. We are able to capture the essential local fluctuations of the system in a large d limit, it gives us a FL at low temperatures and linear in T resistivity at intermediate and high temperatures. The method presented is a real frquency (time) formalism and doesn't rely on analytic continuation unlike quantum monte carlo based approaches. Furthermore, since there is no restoring force or characteristic frequency of the bosonic mode, the characteristic temperature can be low, determined solely by when the long time or low energy quantum coherence due to these diffusive local fluctuations becomes ineffective. However, our results may not directly correlate with observations from specific systems; one fact is the higher crossover temperature compared to empirical findings for the onset of the strange metal regime. Additionally, since all strongly correlated systems have a large but finite U , there is quite likely to be a new low-energy scale related to it, specifically the intersite spin coupling scale J_{ij}, which sets a new small temperature scale, of relative order t/U. Another limitation of our method is that it treats spin and charge fluctuations on the same footing and there is no qualitative difference between them, However this is not true in real systems as well as more exact methods.

Chapter 4

Dynamical Mean Field Theory : Numerical Renormalization Group

Dynamical mean field theory (DMFT) is a powerful non-perturbative framework for investigating strong electron correlation effects in lattice systems with local interactions. It represents a major conceptual advance in the study of many-body physics, particularly in contexts where traditional weak-coupling approaches such as Fermi liquid theory and perturbation theory break down. The central idea of DMFT is to replace the full lattice problem with a self-consistently determined quantum impurity model embedded in a dynamical bath. In its single-site formulation, DMFT is exact in the limit of infinite spatial dimensions ($d \to \infty$), where non-local correlations become negligible and only local quantum fluctuations survive.

This mapping reduces a complex many-body lattice problem (with local interaction) like the Hubbard model to a simpler quantum impurity model, such as the single-impurity Anderson model (SIAM), while still capturing essential dynamical effects arising from local interactions. The bath into which the impurity is embedded is not static but is determined self-consistently from the lattice itself, creating a feedback loop between the impurity and its environment. This self-consistency is the hallmark of DMFT and endows it with the ability to capture local quantum fluctuations accurately.

Single-site DMFT excels at describing local dynamical phenomena, including the formation of local moments, Mott metal-insulator transitions, and the emergence of quasiparticles near the Fermi level. However, it neglects short-range spatial correlations, which can be crucial near phase boundaries or for describing ordered states. Cluster extensions of DMFT [60, 112–114], such as DCA or CDMFT aim to remedy this limitation by including a finite number of spatial degrees of freedom. The success of DMFT is perhaps most dramatically demonstrated in its treatment of the Mott transition in the Hubbard model [115–117]. As the on-site Coulomb repulsion U increases relative to the bandwidth, DMFT captures the continuous evolution from a metallic state with quasiparticles to a gapped Mott insulating state, even at half-filling. Furthermore, DMFT has been successfully combined with density functional theory (DFT) to account for electronic correlations in real materials, leading to hybrid approaches such as DFT+DMFT or DMFT+U.

4.1 DMFT self-consistency

To set up the DMFT equations concretely, we consider the single-band Hubbard model, whose Hamiltonian contains a kinetic hopping term and a local Coulomb repulsion:

$$H = -t \sum_{\langle ij \rangle \sigma} c^{\dagger}_{i\sigma} c_{j\sigma} + U \sum_{i} n_{i\uparrow} n_{i\downarrow} - \mu \sum_{i\sigma} n_{i\sigma} \tag{4.1}$$

where t is the nearest-neighbor hopping, U the on-site interaction strength, and μ the chemical potential.

Using Grassmann fields, we can write the action associated with this model as

$$S = \int_0^{\beta} d\tau \left[\sum_{i\sigma} c^{\dagger}_{i\sigma} \partial_{\tau} c_{i\sigma} - t \sum_{\langle ij \rangle \sigma} c^{\dagger}_{i\sigma} c_{j\sigma} - \mu \sum_{i\sigma} n_{i\sigma} + U \sum_{i} n_{i\uparrow} n_{i\downarrow} \right] \tag{4.2}$$

The partition function is given by the path integral over all Grassmann fields:

$$Z = \int \prod_{i} Dc^{\dagger}_{i\sigma} Dc_{i\sigma} e^{-S} \tag{4.3}$$

To derive the DMFT equations, one selects a representative site (site 0) and integrates out all other degrees of freedom. The result is an effective action S_{eff} for site 0:

$$S_{\text{eff}} = -\int_0^{\beta} \int_0^{\beta} d\tau d\tau' \sum_{\sigma} c^{\dagger}_{0\sigma}(\tau) \mathcal{G}_0^{-1}(\tau - \tau') c_{0\sigma}(\tau') + U \int_0^{\beta} d\tau n_{0\uparrow}(\tau) n_{0\downarrow}(\tau) \tag{4.4}$$

Here, $\mathcal{G}_0^{-1}(\tau - \tau')$ plays the role of a dynamical Weiss mean field, encoding the hybridization of the impurity with its environment. In frequency space, for a general lattice, it is given by

$$\mathcal{G}_0^{-1}(i\omega_n) = i\omega_n + \mu - \sum_{ij} t^2 \left(G_{ij} - \frac{G_{i0} G_{0j}}{G_{00}} \right) \tag{4.5}$$

The interacting Green's function at the impurity site is defined as

$$G(\tau) = -\left\langle T_{\tau} c_0(\tau) c_0^{\dagger} \right\rangle_{S_{\text{eff}}} \tag{4.6}$$

This satisfies the Dyson equation

$$G(i\omega_n) = \left[\mathcal{G}_0^{-1}(i\omega_n) - \Sigma(i\omega_n)\right]^{-1} \tag{4.7}$$

where $\Sigma(i\omega_n)$ is the local impurity self-energy.

The self-consistency condition in DMFT states that the impurity Green's function must equal the local Green's function of the lattice:

$$G(i\omega_n) = \sum_k \frac{1}{i\omega_n + \mu - \epsilon_k - \Sigma(i\omega_n)} \tag{4.8}$$

For the Bethe lattice, which has a semicircular density of states $\rho(\epsilon) = \frac{2}{\pi D^2}\sqrt{D^2 - \epsilon^2}$, the expression for $\mathcal{G}_0^{-1}$ (Eq. 4.5) simplifies to:

$$\mathcal{G}_0^{-1}(i\omega_n) = i\omega_n + \mu - t^2 G(i\omega_n) \tag{4.9}$$

and the local lattice Green's function simplifies to

$$G(i\omega_n) = \int_{-D}^{D} d\epsilon \frac{\rho(\epsilon)}{i\omega_n + \mu - \epsilon - \Sigma(i\omega_n)} \tag{4.10}$$

where $D = 2t$ is the half-bandwidth.

There are many ways to solve the DMFT self-consistency, including continuous time quantum monte carlo (CTQMC), Numerical renormalization Group (NRG), approximate solvers like Iterated perturbation theory (IPT)and Non Crossing approximation (NCA) to mention a few. Each of the methods have their advantages and disadvantages. For examples, CTQMC is an exact solver however since it is an imaginary time method, we need to do numerical analytic continuation of the data to real time or frequency which is an ill posed problem, also CTQMC is a numerically expensive method. Approximate solvers are very cheap when it comes to the computation cost, but these are not exact and might only work in certain parameter regimes of the model. NRG provides solution to the problem directly on the real time/frequency axis, and it is also computationally less expensive than CTQMC.

In this work, we adopt the Numerical Renormalization Group (NRG) as our solver of choice, due to its ability to access real-frequency spectra directly and capture fine low-energy features crucial for understanding strongly correlated metallic states. However, we acknowledge that for intermediate or high-temperature properties, methods like CTQMC may offer better accuracy.

In the following section, we provide a detailed description of the NRG method and demonstrate how it is used in practice to solve the DMFT equations.

4.2 Numerical Renormalization Group

The Numerical Renormalization Group (NRG) is a non-perturbative, real-frequency technique pioneered by Kenneth Wilson in the 1970s to tackle quantum impurity problems. Its original motivation was to resolve the longstanding puzzle associated with the *Kondo effect*, a phenomenon observed in dilute magnetic alloys where conduction electrons interact with a small number of localized magnetic moments. The hallmark of the Kondo effect is a resistivity minimum at low temperatures, counter to the expectations from conventional scattering theories.

The Kondo model, which captures the essential physics of this behavior, describes a localized spin-1/2 magnetic impurity interacting antiferromagnetically with a sea of conduction electrons. The effective Hamiltonian features an exchange coupling J between the impurity and conduction spins. Kondo's perturbative analysis showed that the scattering rate $\gamma(T)$ due to spin-flip processes increases logarithmically as the temperature decreases, specifically as $\gamma(T) \sim \log(D/T)$, where D is the conduction bandwidth. This prediction qualitatively explained the resistivity minimum but led to a theoretical divergence as $T \to 0$, now known as the *Kondo problem*.

Wilson's breakthrough was to devise a controlled renormalization scheme capable of accessing the low-energy fixed point of the Kondo model. His NRG approach demonstrated that at very low temperatures, the magnetic impurity becomes *screened* by conduction electrons, forming a many-body spin singlet. This non-perturbative screening suppresses further spin-flip scattering, causing the resistivity to saturate instead of diverge. The screened state acts like a static, non-magnetic impurity, leading to strong elastic scattering but no magnetic contribution at low T. This insight laid the foundation for understanding a wide range of impurity phenomena, including the emergence of local Fermi liquid behavior.

Building on Wilson's work, the NRG method was later extended to the *Single Impurity Anderson Model* (SIAM), which offers a more general framework incorporating charge fluctuations in addition to spin degrees of freedom.

Single-Impurity Anderson Model

The Single Impurity Anderson Model (SIAM), introduced by P.W. Anderson in 1961, is a fundamental model to describe localized electronic levels hybridizing with a conduction band, especially useful for understanding magnetic impurities in metals, quantum dots, and the central impurity problem in DMFT. The Hamiltonian is structured as follows:

$$\begin{aligned}
H_{\text{SIAM}} &= H_{\text{bath}} + H_{\text{imp}} + H_{\text{hyb}}, \\
H_{\text{bath}} &= \sum_{k,\sigma} \epsilon_k c^\dagger_{k,\sigma} c_{k,\sigma}, \\
H_{\text{imp}} &= \sum_{\sigma} \epsilon_d n_{d,\sigma} + U n_{d,\uparrow} n_{d,\downarrow}, \\
H_{\text{hyb}} &= \sum_{k,\sigma} v_k \left(c^\dagger_{k,\sigma} d_\sigma + d^\dagger_\sigma c_{k,\sigma} \right).
\end{aligned} \tag{4.11}$$

Here, H_{bath} describes a conduction electron reservoir, H_{imp} represents the impurity orbital with onsite energy ϵ_d and Coulomb repulsion U, and H_{hyb} encodes hybridization between the impurity and conduction electrons through tunneling amplitudes v_k.

The physics of SIAM encapsulates both charge and spin fluctuations. At weak hybridization or large U, the impurity level forms a localized magnetic moment, and the system enters a Kondo regime at low temperatures. For smaller U, charge fluctuations dominate, and the model reduces to a broadened resonant level.

To study its electronic properties, one typically computes the impurity Green's function, defined as:

$$G_{d\sigma}(t) = -i\theta(t) \left\langle \left\{ d_\sigma(t), d^\dagger_\sigma \right\} \right\rangle, \tag{4.12}$$

whose Fourier transform satisfies a Dyson equation:

$$G^{-1}_{d\sigma}(\omega) = \mathcal{G}^{-1}_{d\sigma}(\omega) - \Sigma_{d\sigma}(\omega), \tag{4.13}$$

$$\mathcal{G}^{-1}_{d\sigma}(\omega) = \omega - \epsilon_d - \Delta(\omega), \quad \Delta(\omega) = \sum_k \frac{v_k^2}{\omega + i\eta - \epsilon_k}. \tag{4.14}$$

The $\Delta(\omega)$ encodes the effect of the conduction bath on the impurity. Its imaginary part,

$$\Gamma(\omega) = -\frac{1}{\pi} \text{Im}\Delta(\omega), \tag{4.15}$$

known as Hybridization function is the level broadening or decay rate of an impurity electron into the bath. This function plays a central role in characterizing the Kondo screening and the width of the resonance peak at the Fermi energy.

In subsequent sections, we will show how the NRG algorithm discretizes this problem and iteratively diagonalizes the resulting Hamiltonian to access dynamical quantities such as the spectral function and thermodynamic observables over a wide range of temperatures and energy scales.

Logarithmic Discretization

One of the central challenges in solving quantum impurity problems such as the Kondo or Anderson models lies in accurately capturing low-energy excitations near the Fermi level, where strong correlations dominate. Wilson's key insight was to discretize the conduction band on a *logarithmic energy scale*, thereby isolating low-energy physics while retaining computational tractability. This procedure is known as **logarithmic discretization**.

Assume that the conduction band has an energy range $\epsilon \in [-D, D]$, where D is the half-bandwidth. To enhance resolution near $\epsilon = 0$, the Fermi energy, the band is partitioned into intervals that shrink geometrically toward zero using a discretization parameter $\Lambda > 1$. The grid points are placed at $\pm\Lambda^{-n}$ for $n = 1, 2, 3, \ldots, N$, defining intervals:

$$I_n^{\pm} = [\pm\Lambda^{-n}, \pm\Lambda^{-n+1}].$$

Within each interval $I_n^{\pm}$, a single representative state is retained, effectively coarse-graining the conduction band. These representative states are chosen such that the discretized hybridization function $\Gamma^{\text{disc}}(\omega)$ (Fig. 4.1) approximates the continuous $\Gamma(\omega)$ accurately:

$$\Gamma^{\text{disc}}(\omega) = \sum_{n,\pm} \gamma_{\pm n}^2 \delta(\omega - \xi_{\pm n}).$$

Here, $\gamma_{\pm n}$ are effective hybridization amplitudes and $\xi_{\pm n}$ are representative energies for each bin. A natural and commonly used choice is:

$$\gamma_{\pm n}^2 = \int_{I_{\pm n}} d\epsilon\, \Gamma(\epsilon), \tag{4.16}$$

$$\xi_{\pm n} = \frac{\int_{I_{\pm n}} d\epsilon\, \epsilon\Gamma(\epsilon)}{\int_{I_{\pm n}} d\epsilon\, \Gamma(\epsilon)}. \tag{4.17}$$

This discretization exponentially enhances resolution at low energies, which is essential for accurately capturing emergent many-body phenomena such as the Kondo resonance or the Fermi liquid coherence peak.

Wilson Chain

The logarithmic discretization results in a so-called **star geometry**, in which the impurity couples directly to many decoupled energy shells. However, this form is not suitable for iterative diagonalization. Wilson's second major contribution was to map this geometry to a **semi-infinite tight-binding chain**, known as the **Wilson chain**.

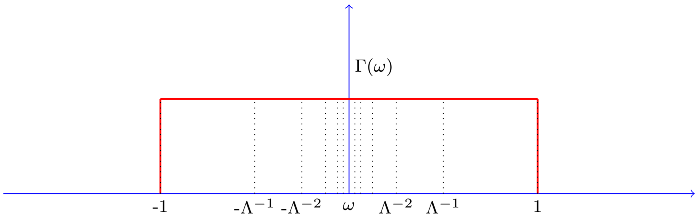

Figure 4.1: Logarithmic discretization for a box shaped hybridization function with $D = 1$.

This transformation is performed by tridiagonalizing the discretized conduction electron Hamiltonian via a Lanczos or Gram-Schmidt procedure, yielding a one-dimensional chain:

$$H_{\text{chain}} = \sum_{\sigma} t_{\text{imp}} \left(d_{\sigma}^{\dagger} f_{0\sigma} + f_{0\sigma}^{\dagger} d_{\sigma} \right) + \sum_{l=0}^{\infty} \sum_{\sigma} \left[t_l \left(f_{l\sigma}^{\dagger} f_{l+1\sigma} + \text{h.c.} \right) + \epsilon_l f_{l\sigma}^{\dagger} f_{l\sigma} \right].$$

Here:

- $d_{\sigma}^{\dagger}$ creates an electron on the impurity,
- $f_{l\sigma}^{\dagger}$ creates an electron at site l of the Wilson chain,
- t_l are hopping amplitudes between neighboring sites,
- ϵ_l are on-site potentials, often zero in the particle-hole symmetric case.

The crucial feature of the Wilson chain (Fig 4.2) is that the hopping amplitudes decay exponentially with site index:

$$t_l \sim \Lambda^{-l/2}.$$

This exponential decay reflects the energy scale separation introduced by the logarithmic discretization. It provides the foundation for the **iterative diagonalization** method: adding a new site corresponds to introducing a much smaller energy scale, and the higher-energy states from earlier steps can be truncated without significantly affecting the low-energy physics.

The Wilson chain transforms the quantum impurity problem into a renormalization group flow along the chain, enabling systematic analysis of the crossover from high-temperature (weak-coupling) to low-temperature (strong-coupling) fixed points. This structure underlies the success of the Numerical Renormalization Group in capturing the emergent low-energy behavior of strongly correlated impurity models.

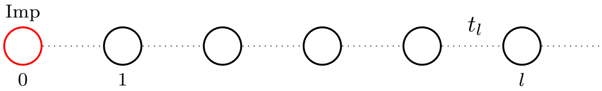

Figure 4.2: Wilson chain where $l = 0$ site (red colored) represents impurity, t_l is the hopping parameter between sites $l - 1$ and l.

Iterative Diagonalization

The Wilson chain obtained after logarithmic discretization of the conduction band forms the starting point for the **Numerical Renormalization Group (NRG)** procedure. The essence of NRG lies in solving the chain *iteratively*, exploiting the exponential decay of energy scales introduced by the logarithmic discretization. The full Hamiltonian for a chain of length L can be written as:

$$H_L = H_{\text{imp}} + H_{\text{hyb}} + \sum_{\ell=0}^{L-1} \sum_{\sigma} \left(\epsilon_\ell f_{\ell\sigma}^\dagger f_{\ell\sigma} + t_\ell f_{\ell\sigma}^\dagger f_{\ell+1\sigma} + \text{h.c.} \right), \tag{4.18}$$

where H_{imp} includes the impurity terms and H_{hyb} is the hybridization between impurity and the first chain site.
The iterative diagonalization proceeds as follows:

1. Begin with a short Wilson chain (typically of length $l = 0$ or $l = 1$) and exactly diagonalize the Hamiltonian.

2. Add one more site to the chain, increasing the chain length from $l \to l + 1$.

3. Diagonalize the enlarged Hamiltonian H_{l+1} in the full Hilbert space of the chain, whose size grows exponentially: $\dim(\mathcal{H}_{l+1}) = d^{l+1}$, where d is the local Hilbert space dimension (e.g., $d = 4$ for spinful fermions per site).

4. Retain only the N_{keep} lowest energy eigenstates. This **truncation** is justified by the energy scale separation: the added site represents physics at exponentially lower energy scales, so high-energy states from earlier iterations are unlikely to contribute significantly.

5. Repeat the process by adding further sites, building up the Wilson chain step by step.

Mathematically, the truncated basis at step l is denoted:

$$H_l \left|\alpha\right\rangle^{(l)} = E_\alpha^{(l)} \left|\alpha\right\rangle^{(l)}, \qquad \alpha = 1, \ldots, N_{\text{keep}}.$$

These low-lying eigenstates form the basis for the next iteration. Crucially, the NRG procedure does not attempt to diagonalize the full many-body problem at once. Instead, it uses a renormalization group logic: solve a hierarchy of effective Hamiltonians defined on chains of increasing length, keeping only the relevant low-energy degrees of freedom at each step.

Energy Scale Separation. The justification for truncation relies on the fact that the hopping amplitudes $t_l \sim \Lambda^{-l/2}$ decay rapidly. Therefore, the energy scale introduced by adding site $l+1$ is $\sim \Lambda^{-l/2}$, which is exponentially smaller than the energy gap of the previous chain. This justifies using the lowest-energy sector of H_l to construct H_{l+1}.

Flow Diagrams and Fixed Points. One of the most powerful outputs of NRG is the construction of the so-called **NRG flow diagram**. At each iteration, the rescaled excitation energies:

$$\widetilde{E}_\alpha^{(l)} = \Lambda^{(l-1)/2}(E_\alpha^{(l)} - E_0^{(l)})$$

are plotted against iteration l. These energies are renormalized so that the scale of the lowest energy levels remains comparable across iterations. The flow diagram reveals the RG trajectory of the system: high-energy iterations describe the ultraviolet (UV) regime, while late iterations approach infrared (IR) fixed points. For instance, in the Kondo model, the flow begins in the local moment regime and ends in a strong-coupling screened singlet regime.

Thermodynamics. At each iteration, thermodynamic quantities such as impurity entropy, specific heat, or susceptibility can be computed from the truncated spectrum using the partition function:

$$Z^{(l)} = \sum_\alpha e^{-\beta E_\alpha^{(l)}}, \qquad S^{(l)} = -\sum_\alpha p_\alpha \log p_\alpha,$$

where $p_\alpha = e^{-\beta E_\alpha^{(l)}}/Z^{(l)}$. By associating a temperature $T_l \sim \Lambda^{-l/2}$ with each iteration, one can map out thermodynamic behavior over many decades of temperature.

Accuracy and Limitations. The choice of truncation parameter N_{keep} controls the tradeoff between computational cost and accuracy. Larger values give better precision but increase memory and time requirements. Typical NRG implementations keep $N_{\text{keep}} \sim 500 - 1000$ states. The energy scale separation becomes less reliable at high temperatures or for sharp spectral features at intermediate scales.

In summary, iterative diagonalization in NRG systematically builds up the low-energy physics of quantum impurity models. It provides access to both thermodynamics and dynamics across many orders of magnitude in energy, with exceptional resolution near the Fermi level.

4.3 Dynamical Correlations in NRG

A major strength of the Numerical Renormalization Group (NRG) lies in its ability to compute real-frequency dynamical quantities with high resolution at low energies. These include spectral functions, Green's functions, susceptibilities, and various correlation functions. In this section, we outline how dynamical correlations are computed in NRG and describe two complementary frameworks: the *Density Matrix NRG* (DM-NRG) and the *Full Density Matrix NRG* (FDM-NRG).

Spectral Functions and the Lehmann Representation

Let A and B be two generic fermionic or bosonic operators (e.g., d_σ and $d_\sigma^\dagger$). The retarded Green's function is defined by:

$$G_{AB}(t) = -i\theta(t)\langle[A(t), B(0)]_\pm\rangle, \tag{4.19}$$

where the ± sign refers to fermionic (anticommutator) or bosonic (commutator) statistics. Fourier transforming to frequency space, we obtain:

$$G_{AB}(\omega) = \int_{-\infty}^{\infty} \frac{\rho_{AB}(\omega')}{\omega - \omega' + i\eta}\, d\omega', \tag{4.20}$$

where $\rho_{AB}(\omega)$ is the *spectral function* defined by:

$$\rho_{AB}(\omega) = -\frac{1}{\pi}\,\mathrm{Im}\, G_{AB}(\omega). \tag{4.21}$$

Using the Lehmann representation, the spectral function can be written in terms of the eigenstates $|n\rangle$ and $|m\rangle$ of the full many-body Hamiltonian:

$$\rho_{AB}(\omega) = \sum_{mn} \frac{e^{-\beta E_n}}{Z}\left(\langle n|A|m\rangle\langle m|B|n\rangle\delta(\omega - E_m + E_n) \mp \langle n|B|m\rangle\langle m|A|n\rangle\delta(\omega + E_m - E_n)\right), \tag{4.22}$$

where $Z = \sum_n e^{-\beta E_n}$ is the partition function and $\beta = 1/k_B T$.

DM-NRG: Reduced Density Matrix Method

The DM-NRG method [118] computes spectral functions using a reduced density matrix constructed at a specific iteration N corresponding to a low temperature $T_N \sim \Lambda^{-N/2}$. The steps are as follows:

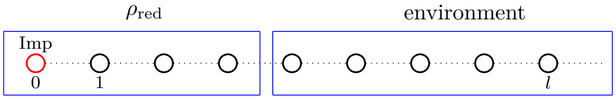

Figure 4.3: Reduced density matrix obtained by tracing out "environment" degrees of freedom of the chain

- Diagonalize the Wilson chain iteratively up to iteration N to obtain the eigenstates $|m\rangle_N$ and eigenenergies E_m^N.
- Construct the thermal density matrix:

$$\hat{\rho} = \sum_m \frac{e^{-\beta E_m^N}}{Z} |m\rangle_N \langle m|_N \,. \tag{4.23}$$

- Trace out the environment degrees of freedom (Fig. 4.3) (i.e., chain sites $l > L$) to obtain the reduced density matrix:

$$\hat{\rho}_{\text{red}} = \text{Tr}_{\text{env}}\, \hat{\rho}. \tag{4.24}$$

- Evaluate the spectral function using this reduced density matrix in the Lehmann representation.

While effective at low temperatures, DM-NRG suffers from the problem that only a single shell (energy scale) contributes to each frequency, leading to violations of spectral sum rules and thermodynamic inconsistencies.

FDM-NRG: Full Density Matrix Approach

To resolve the limitations of DM-NRG, the *Full Density Matrix NRG* (FDM-NRG) was introduced [119]. This method uses the complete Anders-Schiller basis [120], built from all discarded states at every iteration. The central idea is that discarded states form an approximately complete basis for the full Hilbert space:

$$\sum_{l,\alpha,e_l} |\alpha, e_l\rangle_D \langle \alpha, e_l|_D \approx \mathbb{I}, \tag{4.25}$$

where $|\alpha, e_l\rangle_D$ represents a discarded state at iteration l with an environment configuration e_l.

The density matrix is then expressed as:

$$\hat{\rho} = \sum_l w_l \hat{\rho}_{\text{D}}^{(l)}, \tag{4.26}$$

where $w_l = d^{N-l} Z_l / Z$ is a weight factor and $\hat{\rho}_{\mathrm{D}}^{(l)}$ is the thermal density matrix over the discarded states of iteration l.

The spectral function is then computed as:

$$\rho_{AB}(\omega) = \sum_l w_l \rho_{AB}^{(l)}(\omega), \tag{4.27}$$

ensuring exact satisfaction of spectral sum rules and thermodynamic consistency.

Broadening and Continuum Reconstruction

Since the raw spectral function from NRG consists of discrete delta peaks (from transitions between eigenstates), a broadening procedure is required to obtain a smooth spectrum. The commonly used broadening kernel $K(\omega, E)$ interpolates between log-Gaussian (for $|\omega| \gg T$) and Gaussian (for $|\omega| \lesssim T$) forms:

$$\begin{aligned} K(\omega, E) = {} & \frac{\theta(\omega E)}{\alpha |\omega| \sqrt{\pi}} \exp\left(- \left(\frac{\log(\omega/E)}{\alpha} - \gamma \right)^2 \right) h(|\omega|) \\ & + \frac{1}{\omega_0 \sqrt{\pi}} \exp\left(- \left(\frac{\omega - E}{\omega_0} \right)^2 \right) (1 - h(|\omega|)), \end{aligned} \tag{4.28}$$

$$h(\omega) = \exp\left(- \left(\frac{\log(\omega/\omega_0)}{\alpha} \right)^2 \right), \qquad \gamma = \alpha/4. \tag{4.29}$$

Here, α is the broadening parameter, and $\omega_0 \sim T$ is the crossover energy scale. The choice of broadening function is crucial for balancing frequency resolution and smoothness.

Advantages of NRG for Dynamics

- **Real-frequency data**: Unlike Monte Carlo methods, NRG works directly in the real frequency domain.
- **Low-temperature resolution**: NRG excels at resolving sharp features (e.g., Kondo resonance) near the Fermi level at $T \ll T_K$.
- **Thermodynamic consistency**: FDM-NRG ensures exact fulfillment of sum rules and thermodynamic quantities.
- **Versatility**: Spectral functions for fermionic, bosonic, or mixed operators can all be computed.

In the next chapter, we shall illustrate how these methods are applied to compute physical observables within DMFT, including impurity spectral functions, self-energy, and conductivity.

Chapter 5

Spin-Charge Dynamics and the Coherent to incoherent Crossover in the Hubbard Model

In the preceding chapter, we developed the theoretical and numerical infrastructure underlying the Numerical Renormalization Group (NRG) method, and outlined how it functions as an impurity solver within the framework of Dynamical Mean Field Theory (DMFT). In this chapter, we move from formulation to application: our goal is to implement the NRG-based DMFT self-consistency loop for the one-band Hubbard model and to analyze the resulting physical observables with a focus on spin and charge dynamics.

Beyond presenting computational results, we aim to extract clear physical insights into the nature of correlated electron behavior, especially across the Mott metal-insulator transition (MIT), the coherence-incoherence crossover, and the evolution of spectral properties with temperature. The key idea driving this chapter is that spin and charge excitations do not necessarily behave in tandem: their dissipation mechanisms, coherence scales, and transport properties exhibit subtle, and sometimes striking, differences. We attempt to clarify these dynamics using NRG's strength in resolving low-energy features with high fidelity.

5.1 Introduction: Motivation and Context

The correlation-driven Mott metal-insulator transition (MIT) [8, 116, 121–124] has long been a central topic in condensed matter physics. While bandwidth- and filling-controlled MITs are by now reasonably well understood from a one-particle perspective [125–127], the behavior of two-particle observables—namely, the collective, dynamical fluctuations of spin and charge remains an active and challenging area of research.

Experimental advances over the past two decades have elevated this question to the forefront. In particular, resonant inelastic X-ray scattering (RIXS) [128–134] and momentum-resolved electron energy loss spectroscopy (m-EELS) [110, 134] have enabled unprecedented access to frequency- and momentum-resolved charge and spin dynamics. While RIXS provides simultaneous information about spin and charge responses, m-EELS predominantly probes the dynamic dielectric function $1/\epsilon(\mathbf{q}, \omega)$, offering a complementary window into collective charge modes.

These developments demand a detailed theoretical understanding of two-particle dynamics in the vicinity of the MIT. Yet, many analytical tools struggle to compute irreducible vertices or dynamical susceptibilities with controlled accuracy. In this light, numerical methods—in particular Dynamical Mean Field Theory (DMFT)—have emerged as leading candidates for providing such insights. The DMFT approximation becomes particularly effective near the MIT, where spatial fluctuations are suppressed, and the problem becomes locally dominated.

An associated, and arguably deeper, puzzle is the nature of the quantum-to-classical crossover near the MIT. In many correlated materials—such as Sr_2RuO_4—a coherence scale T_{coh} of order 10–20 K is observed, below which quasiparticle excitations acquire coherence, while above it, the system enters an incoherent, often anomalous metallic state. DMFT and ECFL studies [31, 39] have successfully captured various aspects of this crossover, particularly for one- and multiband Hubbard models. But the fate of two-particle responses—specifically, how spin and charge fluctuations evolve across this crossover—remains insufficiently explored.

While continuous-time quantum Monte Carlo (CTQMC) is a powerful and widely used impurity solver in DMFT, it faces significant challenges at low temperatures due to both computational cost and the ill-posed nature of analytic continuation. In contrast, NRG is ideally suited for studying spectral and dynamical properties at low frequencies and temperatures. Despite this, NRG-based DMFT implementations have been underutilized for probing collective spin and charge dynamics, particularly in the context of two-particle responses like susceptibilities and diffusion spectra.

Objectives of this Chapter

In this chapter, we address the above gaps by using NRG as a robust impurity solver to investigate spin and charge dynamics in the single-band Hubbard model within DMFT. Our study is guided by two main goals:

1. To trace the evolution of spin and charge fluctuations across the Mott transition at very low temperatures.
2. To characterize their behavior across the coherence-incoherence crossover, identifying distinct coherence scales for spin and charge and their implications for transport.

We employ both the Density Matrix NRG (DMNRG) and the Full Density Matrix NRG (FDM-NRG) formulations, analyzing their relative strengths and limitations in resolving low-frequency spectral features. Through the lens of dynamical susceptibilities, characteristic frequency scales, spectral shape diagnostics (such as kurtosis), Kullback-Leibler divergence, and diffusion constants, we seek to articulate a coherent physical picture of how local bosonic (spin/charge) modes emerge, evolve, and eventually decohere in strongly correlated electron systems.

We conclude by discussing the implications of our findings for broader classes of models—particularly multiorbital or cluster extensions of DMFT—where non-Fermi liquid behavior may persist to the lowest temperatures due to partial Mott localization or orbital-selective phenomena.

5.2 Model and Method

In this section, we summarize the minimal ingredients and computational tools used to study the spin and charge dynamics within the single-band Hubbard model. Since the model and its physical motivation have already been thoroughly introduced in earlier chapters, we focus here on the specific implementation of DMFT and the NRG impurity solver as applied to our problem.

We begin by restating the Hubbard Hamiltonian for reference:

$$\mathcal{H} = -t \sum_{\langle ij \rangle, \sigma} (c^\dagger_{i\sigma} c_{j\sigma} + \text{h.c.}) + U \sum_i n_{i\uparrow} n_{i\downarrow} - \mu \sum_{i\sigma} n_{i\sigma}, \tag{5.1}$$

where t is the nearest-neighbor hopping amplitude, U is the local Coulomb repulsion, and μ is the chemical potential. $c^{(\dagger)}_{i\sigma}$ are the standard fermionic creation and annihilation operators, and $n_{i\sigma} = c^\dagger_{i\sigma} c_{i\sigma}$.

The Dynamical Mean Field Theory (DMFT) maps the lattice model onto a self-consistent quantum impurity model embedded in a dynamical bath. Within this formalism, the local Green's function is given by:

$$G(\omega) = \int d\epsilon\, \rho(\epsilon) \left[\omega + \mu - \epsilon - \Sigma(\omega)\right]^{-1}, \tag{5.2}$$

where $\rho(\epsilon)$ is the non-interacting density of states, and $\Sigma(\omega)$ is the local self-energy. The self-consistency condition is imposed through the so-called Weiss field, or non-interacting impurity Green's function:

$$\mathcal{G}_0^{-1}(\omega) = \omega + \mu - \Delta(\omega), \tag{5.3}$$

with $\Delta(\omega)$ the hybridization function describing the coupling between the impurity and the bath.

For all calculations presented in this work, we employ a Bethe lattice with a semi-elliptic density of states, $\rho(\epsilon) = \frac{2}{\pi D^2}\sqrt{D^2 - \epsilon^2}$, where $D = 2t$ is the half-bandwidth. The hybridization function then simplifies to $\Delta(\omega) = t^2 G(\omega)$.

To solve the quantum impurity problem, we utilize the Numerical Renormalization Group (NRG). NRG discretizes the conduction bath logarithmically using a discretization parameter $\Lambda > 1$ and maps the impurity model onto a semi-infinite Wilson chain. The hopping amplitudes along this chain decay exponentially with site index, $\sim \Lambda^{-l/2}$, enabling a natural separation of energy scales. At each iteration, the Hamiltonian is diagonalized by retaining only the lowest-lying eigenstates, allowing access to low-energy physics in a controlled manner.

The Green's function $G_{AB}(t)$ for two operators A and B is computed via the real-time correlation function:

$$G_{AB}(t) = -i\theta(t)\langle [A(t), B]_{\pm} \rangle, \tag{5.4}$$

with the ± sign denoting commutator or anticommutator depending on the bosonic or fermionic nature of the operators. The spectral function is obtained from its Fourier transform:

$$G_{AB}(\omega) = \int_{-\infty}^{\infty} \frac{\rho_{AB}(\omega_1)}{\omega - \omega_1}\, d\omega_1, \tag{5.5}$$

where the spectral density is $\rho_{AB}(\omega) = -\frac{1}{\pi}\mathrm{Im} G_{AB}(\omega)$.

For the local fermionic Green's function, A and B are chosen as c and $c^\dagger$, yielding the electronic density of states $A(\omega)$. Similarly, the local charge and spin susceptibilities are defined via the number operator n and the spin operator s:

$$n = \sum_{\sigma=\uparrow,\downarrow} c_\sigma^\dagger c_\sigma, \tag{5.6}$$

$$s = c_\uparrow^\dagger c_\uparrow - c_\downarrow^\dagger c_\downarrow, \tag{5.7}$$

leading to

$$\chi_n(\omega) = \int_{-\infty}^{\infty} dt\, e^{i\omega t} \left(-i\theta(t) \langle [n(t), n] \rangle \right), \tag{5.8}$$

$$\chi_s(\omega) = \int_{-\infty}^{\infty} dt\, e^{i\omega t} \left(-i\theta(t) \langle [s(t), s] \rangle \right). \tag{5.9}$$

Spectral functions are broadened using a log-Gaussian kernel to extract continuous spectra from the discrete NRG data. We apply a hybrid kernel smoothly interpolating between log-Gaussian and Gaussian forms, as described in the main text. Parameters used include $\alpha = 0.1 - 0.5$, and calculations are performed using the NRG Ljubljana code with $\Lambda = 2$, $N_z = 8$. A refined self-energy trick improves convergence and resolution.

In the subsequent sections, we present the results for spin and charge spectral functions obtained via both DMNRG and FDM-NRG. We also define and analyze the diffusion spectrum $P_{n/s}(\omega)$:

$$P_{n/s}(\omega) = \frac{\mathrm{Im}\chi_{n/s}(\omega)}{\pi\omega\chi_{n/s}}, \tag{5.10}$$

which captures the frequency-resolved energy dissipation of spin and charge excitations. All frequency and temperature scales are normalized by the half-bandwidth D throughout.

5.3 Half-Filled Hubbard Model

Comparative Analysis of Diffusion Spectra Using DMNRG and FDM Methods

In this subsection, we undertake a detailed comparative analysis of the spin and charge diffusion spectra, $P_{n/s}(\omega)$, computed using two complementary variants of the Numerical Renormalization Group: the Density Matrix NRG (DMNRG) and the Full Density Matrix (FDM) approach. Each method has distinct advantages: DMNRG is known for its high resolution at low temperatures, while FDM is more versatile across a broader temperature range. Here, we focus on the low-temperature regime with $T/D = 0.001$, under half-filling conditions, and critically assess how well each method captures the low-frequency structure and overall spectral profile.

Figure 5.1 shows the evolution of the spin diffusion spectrum (SDS), $P_s(\omega)$, as a function of U/D for the metallic phase of the half-filled Hubbard model at $T/D = 0.001$. It is well established that a weakly correlated Landau Fermi liquid (LFL) evolves smoothly into a strongly correlated LFL with increasing U/D. The hallmark of this crossover is the emergence of a narrow lattice Kondo resonance, which reflects the coherent propagation of heavy quasiparticles. This behavior stems from the many-body screening of local magnetic moments by conduction electrons—the so-called lattice Kondo effect. When the temperature exceeds the coherence scale T_{coh}, the Kondo singlet is thermally destroyed, reviving local moment fluctuations and suppressing the resonance.

The spin diffusion spectrum evolves in tandem with this crossover. At weak coupling (small U/D), $P_s(\omega)$ displays a broad lineshape, signifying the absence of robust local moments. As U/D increases, itinerance is suppressed, and local moments begin to form, enhancing low-energy spin fluctuations. Consequently, the spectrum narrows and peaks sharply at $\omega = 0$. In the Mott insulating regime ($U/D > 3.0$), $P_s(\omega)$ collapses into a delta function at zero frequency. This reflects the site-local, degenerate magnetic fluctuations of the Mott state, which are uncorrelated in space due to the local nature of DMFT. It is worth noting that in more refined treatments with non-local correlations, such local moments would be expected to form singlets at low energies, thereby gapping out this feature.

Figure 5.1(a) presents the DMNRG results, showing continuous and smooth spectral evolution across the interaction range. The method reliably captures the progressive narrowing of the spectrum and the enhancement of low-frequency spectral weight. This underscores DMNRG's accuracy and stability in resolving low-energy physics. By contrast, the FDM-derived spectra in Fig. 5.1(b) reproduce the gross features but exhibit a pronounced and unphysical dip at $\omega = 0$. This artifact, arising from inaccuracies in the low-frequency slope of the dynamical susceptibility, is amplified upon computing $P_s(\omega) = \mathrm{Im}\chi_s(\omega)/\pi\omega\chi_s$, as the denominator diverges at small ω.

This comparison highlights the strengths and limitations of each method. DMNRG provides a high-fidelity representation of the diffusion spectrum at low temperatures and energies, while FDM, although robust for higher T, requires caution when interpreting results near $\omega = 0$. For problems where low-energy precision is essential—such as coherence-incoherence crossovers and transport anomalies—DMNRG emerges as the more reliable tool.

Analysis of the Charge Diffusion Spectrum

The charge diffusion spectrum, presented in Fig. 5.2, exhibits markedly distinct characteristics compared to its spin counterpart. At low temperature $T/D = 0.001$, and for small-to-moderate U/D, the charge diffusion spectrum $P_n(\omega)$ at half-filling shows a two-subband structure. This structure broadens as U/D increases, accompanied by a steady suppression of spectral weight at low frequencies. As the system enters the strongly correlated Fermi liquid (FL) regime, a remarkable transformation occurs: $P_n(\omega)$ develops a sharp, narrow split-peak centered around $\omega = 0$, which coexists with high-energy, incoherent Hubbard-like

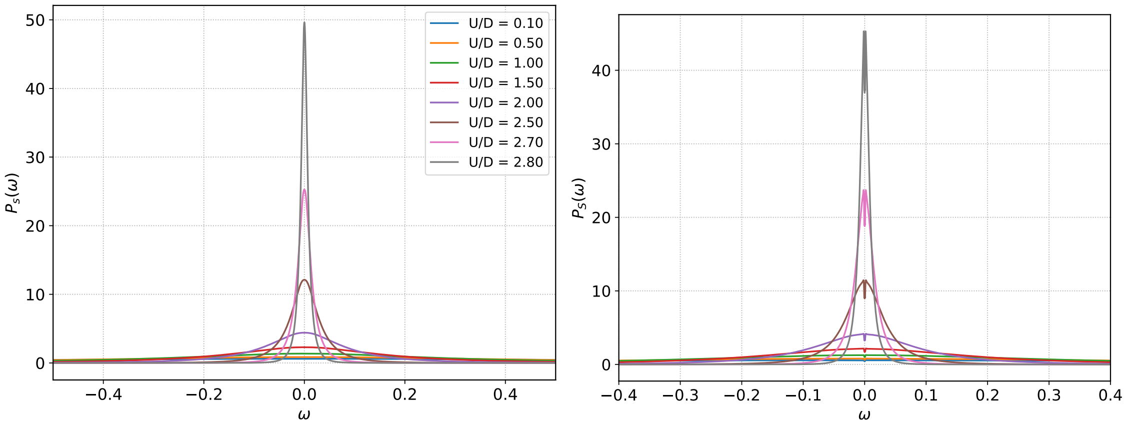

(a) (b)

Figure 5.1: (a) Spin diffusion spectrum for half-filling using DMNRG at $T/D = 0.001$. (b) Spin diffusion spectrum for half-filling using FDM at $T/D = 0.001$.

bands. Interestingly, while the width of this low-energy feature decreases with U/D, its height remains approximately constant. This spectral evolution mirrors the development of a sharp Kondo resonance in the one-fermion spectrum and reflects the emergence of long-lived, heavy quasiparticles.

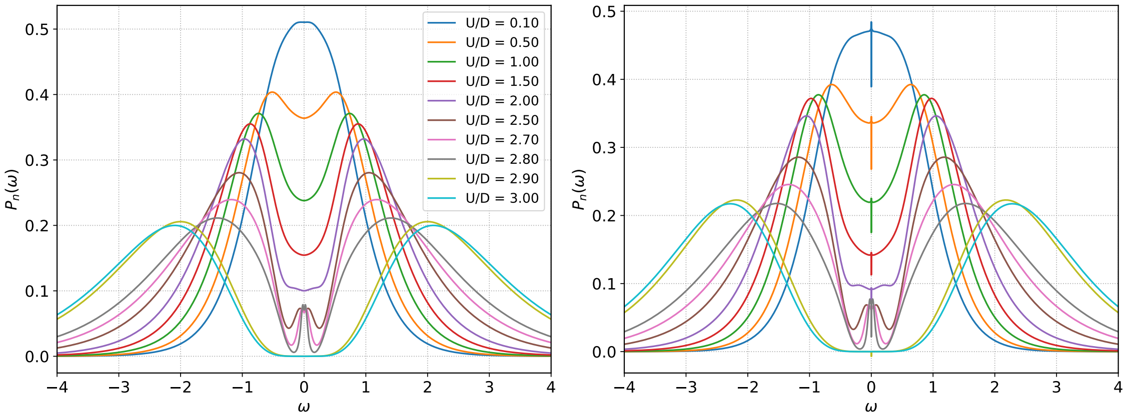

(a) (b)

Figure 5.2: (a) Charge diffusion spectrum for half-filling using DMNRG at $T/D = 0.001$. (b) Charge diffusion spectrum for half-filling using FDM at $T/D = 0.001$.

This behavior can be understood in terms of the underlying symmetry structure of the half-filled Hubbard model. The true symmetry group is $O(4)/\mathbb{Z}_2 = SU(2)_{\text{spin}} \times SU(2)_{\text{charge}}$, where the charge sector is associated with the pseudospin operators $\tau^+ = c_\uparrow^\dagger c_\downarrow^\dagger$, $\tau^- = c_\downarrow c_\uparrow$, and $\tau^z = (1 - n_\uparrow - n_\downarrow)/2$. These operators generate an SU(2) algebra and are related to spin operators by a particle-hole transformation on one spin species.

At small U/D, strong itinerance driven by t prevents the coherent formation of charge pseudospins, and this is reflected in the broad, incoherent two-band structure of $P_n(\omega)$. As U/D increases, reduced itinerance allows charge pseudospins to "preform" and undergo a Kondo-like screening process. Importantly, this does not require conventional spin-Kondo screening but merely that the quasiparticles become sufficiently heavy for charge-pseudospin dynamics to manifest. When the charge-pseudospin fluctuation timescale $\tau_{ch} \sim \hbar/(k_B T^{ch}_{\mathrm{coh}})$ becomes comparable to the fermion hopping timescale $\tau \sim \hbar/D$, charge fluctuations can be dynamically quenched.

Achieving full Landau Fermi liquid behavior requires both spin and charge pseudospin fluctuations to be quenched, leading to two distinct coherence scales: T^{s}_{coh} for spin and T^{ch}_{coh} for charge, with $T_{\mathrm{FL}} = T^{s}_{\mathrm{coh}} < T^{ch}_{\mathrm{coh}}$. This two-step process is reflected in resistivity measurements, which exhibit three regimes: a bad metal phase with $\rho_{dc}(T) \sim \rho_0 + A_1 T$, a quantum-incoherent regime with $\rho_{dc}(T) \sim A_2 T$, and a low-temperature Fermi liquid phase with $\rho_{dc}(T) \sim BT^2$. Our results suggest that these regimes correspond to: (i) no pseudospin quenching, (ii) charge pseudospin quenched but spin unquenched, and (iii) both sectors quenched.

In the insulating phase at $U/D = 0.29$ and 0.30, $P_n(\omega)$ shows a clear suppression near $\omega = 0$, signifying a charge gap characteristic of the Mott insulator. This gap is approximately twice the single-particle DOS gap, as shown in Fig. 5.3, indicating the energy cost of particle-hole excitations.

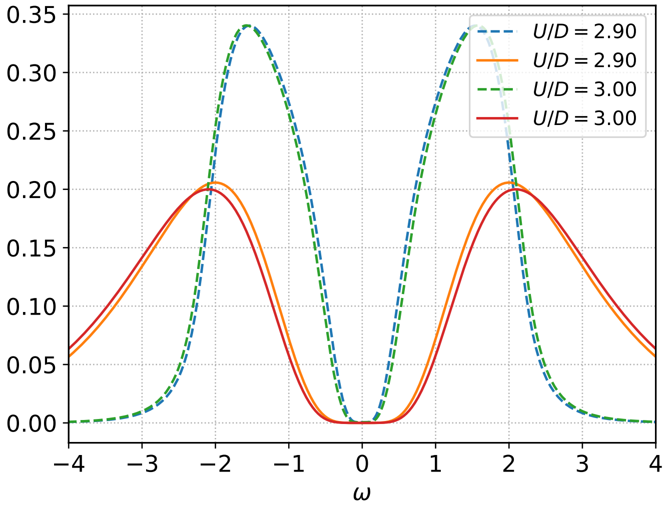

Figure 5.3: Energy gap comparison for single-particle DOS and charge diffusion spectra. Dotted lines represent the single-particle density of states, and solid lines represent the charge diffusion.

Turning to the comparative evaluation of DMNRG and FDM, we observe in

Fig. 5.2 that DMNRG yields a smoother and physically consistent spectrum with a low-frequency peak that accurately captures the emergence of coherence. In contrast, FDM results display a persistent spurious dip near $\omega = 0$ across all tested U values. This artifact stems from slope errors in the charge susceptibility, which get amplified upon division by ω in the definition of $P_n(\omega)$. A detailed analysis of this low-frequency behavior and strategies for artifact reduction in FDM are discussed in Appendices E and F.

While FDM remains valuable for broader spectral studies, it lacks the precision required for quantitative low-frequency physics. In contrast, DMNRG proves superior in resolving coherent features central to transport and dynamical correlation studies in strongly correlated systems.

5.4 Doped Hubbard Model

We now turn to the doped Mott insulating regime of the Hubbard model at interaction strength $U = 4.0$, focusing on doping concentrations $\delta = 0.1, 0.15, 0.2$, and 0.25. Our primary goal is to explore how spin and charge diffusion spectra evolve with temperature in these doped regimes. Figure 5.4 shows representative results for $\delta = 0.1$, obtained using Full Density Matrix Numerical Renormalization Group (FDM-NRG) combined with Pade analytic continuation, using a broadening parameter $\eta/D = 0.05$ for stable and accurate results.

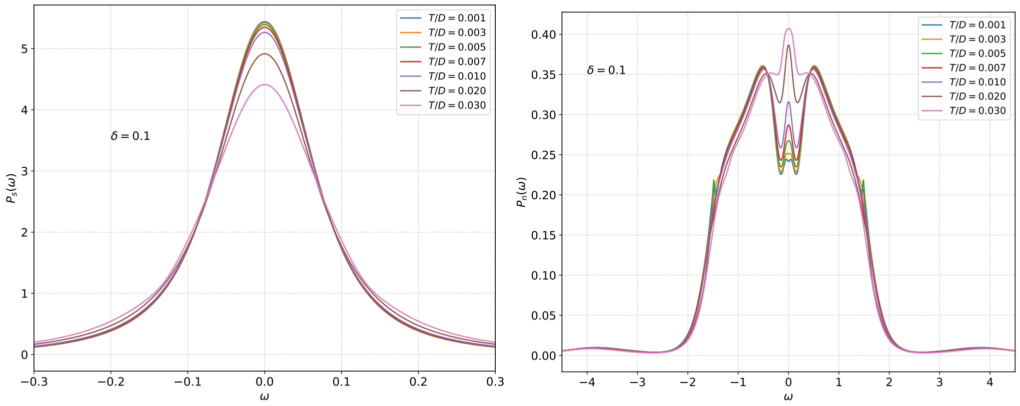

(a) (b)

Figure 5.4: (a) Spin diffusion spectrum and (b) charge diffusion spectrum at various temperatures for $\delta = 0.1$ obtained through Pade analytic continuation ($\eta/D = 0.05$).

The spin diffusion spectrum (SDS) shows a dominant peak centered at $\omega = 0$, indicating robust low-energy spin excitations. In contrast, the charge diffusion spectrum (CDS) reveals a more intricate structure, with distinct peaks spanning both low and high energy ranges. Figure 5.5 displays the single-particle density of states (DOS) for comparison, highlighting the presence of a sharp quasiparticle peak—hallmark of Fermi liquid (FL) behavior—at similar doping.

A remarkable feature in both SDS and CDS is the emergence of *isosbestic points*: characteristic frequencies $\omega_s \approx 0.07$ for spin and $\omega_c \approx 0.5$ for charge, at which the spectra remain essentially unchanged with temperature. The existence of such T-invariant crossing points is a hallmark of spectral weight redistribution driven by thermal fluctuations, and serves as a fingerprint of coherent-to-incoherent crossover dynamics. In the SDS, the spectral evolution with doping largely mirrors the undoped case, albeit with enhanced damping due to mobile carriers. The CDS, on the other hand, exhibits pronounced low-energy restructuring—a clear deviation from the half-filled case.

Doping explicitly breaks particle-hole symmetry, and reduces the full $SU(2) \times SU(2)$ symmetry of the half-filled Hubbard model to $U(1) \times SU(2)$. The chemical potential term $\mu \sum_i n_i$ couples directly to charge but not spin, acting as an external field that alters the phase landscape. This suppresses violent charge-phase fluctuations and enables more coherent low-energy charge dynamics. In the large-U Kondo regime, the CDS features a distinct low-energy peak, enhanced compared to half-filling. As temperature increases, this peak broadens and becomes overdamped, reflecting thermally driven destruction of charge pseudospin coherence.

The weight reduction of the low-energy CDS peak with temperature again underscores the prerequisite of well-formed one-fermion excitations for coherent low-energy charge fluctuations. As T increases, spectral weight shifts from high to low energy in a manner that becomes progressively incoherent. Meanwhile, in the SDS, thermal smearing weakens the central peak and transfers spectral weight to higher energies beyond the isosbestic point. While a complete sum-rule based derivation is left for future work, we speculate that these isosbestic points are connected to sum rules involving charge compressibility and local moment conservation.

To quantitatively characterize the crossover from coherent to incoherent behavior, we employ four complementary diagnostics: characteristic frequency scale $\Omega_{n/s}$, Kullback-Leibler divergence (KLD), kurtosis, and diffusion constant. Each measure probes different aspects of the spectral structure—mean fluctuation energy, deviation from reference distributions, sharpness or flatness of spectra, and transport properties respectively. Together, they provide a multi-faceted understanding of how spin and charge excitations evolve under doping and temperature.

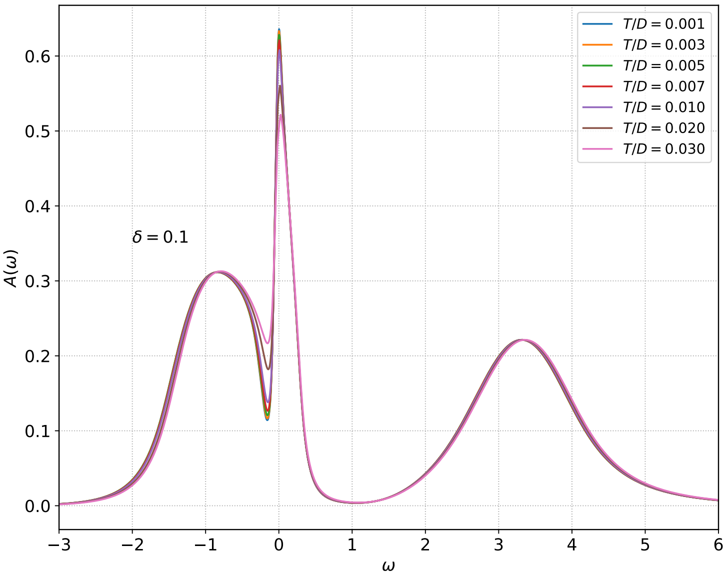

Figure 5.5: Density of states at various temperatures for $\delta = 0.10$.

Characteristic Frequency Scale and Quantum-Classical Transitions

The diffusion spectrum $P_{n/s}(\omega)$ is symmetric about zero and captures both absorption and emission processes of local, bosonic-like spin and charge excitations. To quantify the mean energy scale of these fluctuations, we compute the positive-frequency-weighted average:

$$\Omega_{n/s} = \int_0^\infty d\omega\, \omega\, P_{n/s}(\omega). \tag{5.11}$$

This quantity acts as a thermometer for quantum-to-classical transitions. By comparing $\Omega_{n/s}$ to $k_B T$, we assess the temperature at which fluctuations lose coherence and become classical. Figure 5.6 shows the doping evolution of $\Omega_{n/s}$, while Fig. 5.7 displays the corresponding inverse static susceptibilities.

Our findings reveal a clear hierarchy: spin excitations become classical at lower temperatures than their charge counterparts. This separation implies a two-stage coherence loss—first spin, then charge—highlighting a crucial mechanism behind non-Fermi liquid behavior. In particular, the coexistence of incoherent spin backgrounds with quantum-coherent charge dynamics can manifest as linear-T resistivity. At higher T, when even charge coherence breaks down, this leads to a second, more diffusive linear-T regime—the so-called "bad metal." Below both coherence scales, full Fermi liquid behavior is recovered.

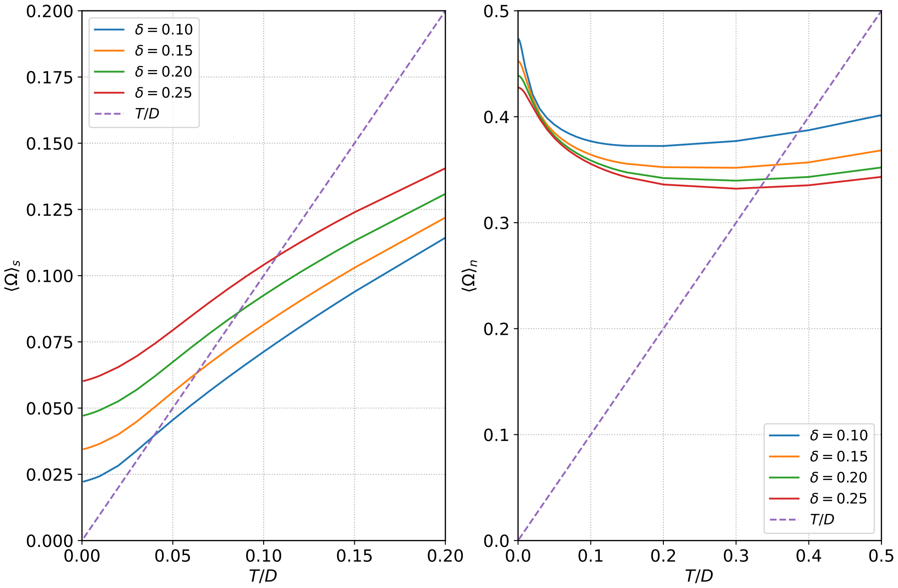

Figure 5.6: Average frequency scale $\Omega_{n/s}$ of spin and charge fluctuations at $U = 4$ for dopings $\delta = 0.1, 0.15, 0.2, 0.25$.

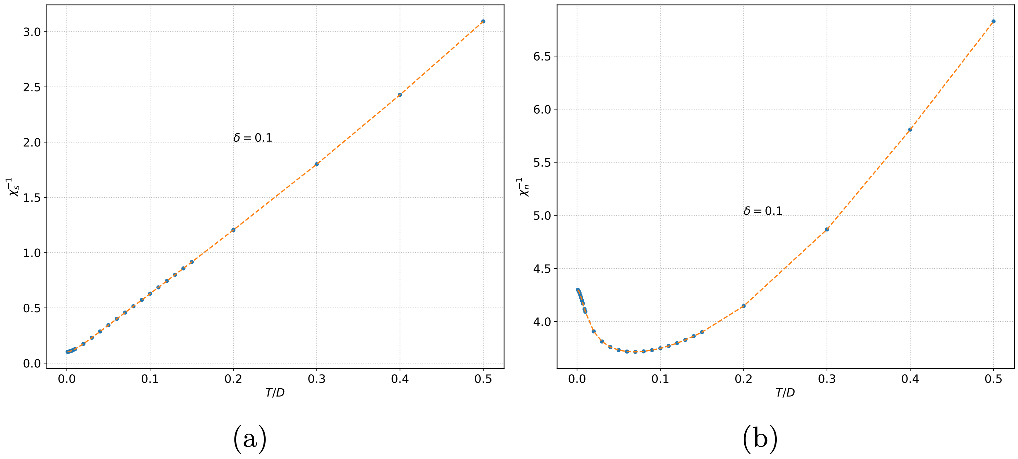

(a) (b)

Figure 5.7: Temperature dependence of (a) inverse spin susceptibility and (b) inverse charge susceptibility at $\delta = 0.1$.

Kullback-Leibler Deviation Analysis

Analyzing the diffusion spectrum $P_{n/s}(\omega)$ through the Kullback-Leibler (KL) divergence provides deeper insights beyond those offered by the characteristic frequency scale $\Omega_{n/s}$. While $\Omega_{n/s}$ captures the energy scale at which quantum-to-classical transitions occur, the KL divergence highlights how the overall distribution shifts across temperature regimes, offering a more detailed picture of the system's evolution.

The KL divergence is particularly useful for identifying anomalous temperature ranges in the cdrossover regions that may not align neatly with the expected Fermi liquid or incoherent behavior. This analysis can reveal intermediate or mixed regimes that $\Omega_{n/s}$ might overlook, providing an additional layer of understanding about the system's behavior. By measuring how $P_{n/s}(\omega)$ departs from a reference state, such as a Fermi liquid distribution, the KL divergence can pinpoint subtle deviations that characterize the crossover from coherent to incoherent behavior.

Furthermore, the KL divergence is sensitive to the finer features of the diffusion spectra, such as variations in width, shape, and peak positions, which may not be fully captured by $\Omega_{n/s}$. This sensitivity allows for a more detailed assessment of how energy dissipation and transport properties evolve with temperature. For instance, differences in the way spin and charge spectra respond to temperature changes can be highlighted, shedding light on the underlying interactions and correlation effects that influence transport and scattering processes. Given a reference probability distribution $P(\omega)$, the KL Divergence with respect to another distribution $Q(\omega)$ is defined as

$$KLD(P||Q) = \int_{-\infty}^{\infty} d\omega P(\omega) \log \frac{P(\omega)}{Q(\omega)} \tag{5.12}$$

Fig. 5.8 illustrates the KL deviation for spin and charge when compared to their respective Fermi liquid reference distributions. The analysis shows that the spin KLD remains aligned with the Fermi liquid reference up to a crossover temperature lower than that for charge, indicating that charge excitations maintain coherent quasiparticle-like quantum behavior over a broader temperature range. This reflects the separate scales associated with persistence of quantum coherence in charge and spin dynamics before both eventually transit to a more classical, diffusive state.

In contrast, the charge KLD begins to deviate from the Fermi liquid reference at a higher temperature, suggesting that charge excitations lose their coherent, Fermi liquid character at T higher than that for spin excitations. This difference in the temperature behavior of spin and charge KLDs has significant implications for understanding transport properties in strongly correlated systems, indicating a quicker breakdown of quantum coherence for spin fluctuations as T increases.

The KL deviation offers a complementary perspective to $\Omega_{n/s}$ by providing a quantitative measure of how closely the system's state at a given T matches an established regime, such as a Fermi liquid or an incoherent state. This added layer of analysis can help uncover subtle shifts and complex crossovers that the characteristic frequency scale alone might not reveal, thereby helping enhance our understanding of the intricate interplay between spin and charge dynamics in the doped Hubbard model.

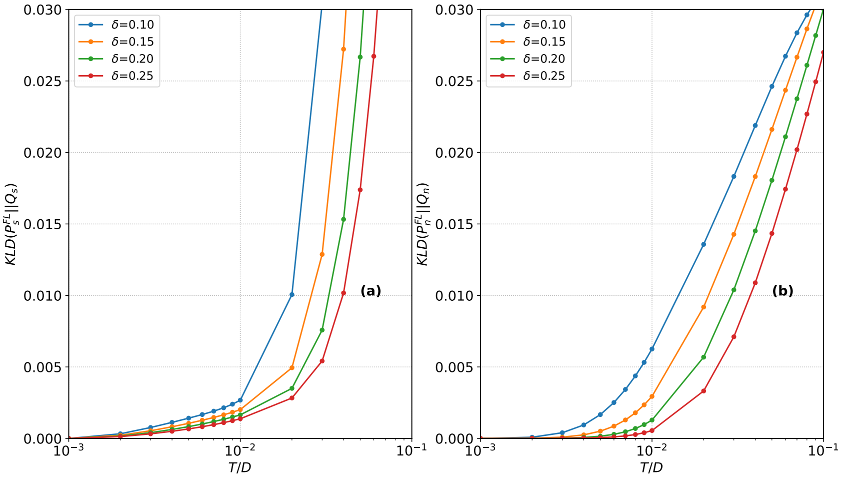

Figure 5.8: (a) KL divergence for spin diffusion spectra with reference distribution in FL phase.(b) KL divergence for charge diffusion spectra with reference distribution in FL phase.

Understanding Kurtosis in the Diffusion Spectrum

Examining the kurtosis of spin and charge diffusion spectra provides valuable insights that go beyond those offered by the characteristic frequency scale $\Omega_{n/s}$ and the KL divergence. While $\Omega_{n/s}$ and KL divergence offer a broad understanding of energy scales and deviations from reference distributions, kurtosis delves deeper into the shape and tail behavior of the spectrum, shedding light on the nature of excitations within the system.

Kurtosis, defined as:

$$Kurt = \frac{\int_{-\infty}^{\infty} \omega^4 P_{n/s}(\omega) d\omega}{\left(\int_{-\infty}^{\infty} \omega^2 P_{n/s}(\omega) d\omega\right)^2}, \quad \text{Excess Kurtosis} = Kurt - 3 \tag{5.13}$$

quantifies the sharpness or "tailedness" of a distribution. High kurtosis indicates a spectrum with pronounced peaks and heavy tails, signifying concentrated energy dissipation or fluctuations around specific frequencies. Conversely, low kurtosis suggests a flatter, more evenly distributed spectrum, pointing to a more uniform spread of excitations. This analysis provides a detailed view of the system's behavior across temperature changes, highlighting aspects that characteristic frequency scales and KL divergence do not capture.

While $\Omega_{n/s}$ provides an average measure of excitation energy and the KL divergence helps identify deviations from reference states to illustrate how distributions shift away from known behaviors, neither metric addresses the distribution's sharpness or tailedness directly. This is where kurtosis brings additional insights. For

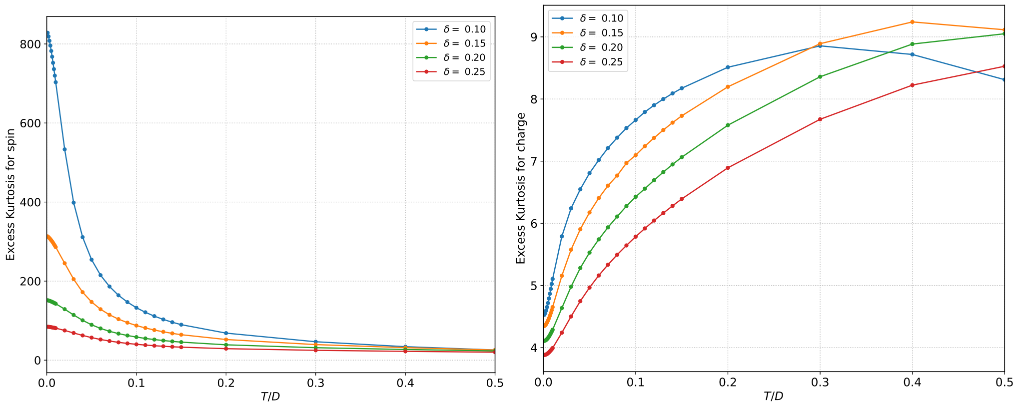

(a) (b)

Figure 5.9: Excess kurtosis for spin and charge diffusion spectra at $U = 4$

example, high kurtosis at low temperatures indicates sharp, coherent excitations characteristic of a Fermi liquid state. As temperature increases, a decrease in kurtosis could imply a broadening of the distribution, signaling the shift to more diffuse excitations typical of an incoherent or classical state.

The kurtosis analysis also helps differentiate the temperature response of spin and charge excitations. This complements findings from the KL divergence, indicating not only when spin and charge begin to diverge from Fermi liquid behavior but also how the distribution properties change as they move toward incoherence.

Overall, kurtosis complements the analysis by showing when the system retains sharp excitations or transitions to a more uniform distribution with temperature. This helps understanding the stability of spin and charge excitations as they move from quantum coherence to classical diffusion. When combined with insights from $\Omega_{n/s}$ and the KL divergence, kurtosis offers a comprehensive view of how spin and charge dynamics evolve across temperature regimes. Since kurtosis can be experimentally extracted from charge- and spin-fluctuation spectra and related to the corresponding dynamical susceptibilities, these connections could be testable.

Fig. 5.9 illustrates the kurtosis for spin and charge diffusion spectra. The results indicate that spin kurtosis is significantly higher at low temperatures, reflecting sharp, well-defined excitations typical of coherent Fermi liquid behavior. As temperature rises, spin kurtosis decreases, indicating a broadening of the distribution as the system transitions to a more classical or incoherent state. Conversely, the kurtosis for charge begins at a separate temperature, implying more evenly distributed, less sharply defined excitations. This accords with indications from other measures above, and supports a two-stage recovery of quasiparticle coherence.

Finally, charge kurtosis is around 100 times smaller than spin kurtosis, further underscoring the distinct nature of spin and charge dynamics. It shows that spin excitations dominate and are more prone to maintaining coherent, sharp features at low temperatures, while charge excitations demonstrate more gradual changes and broader distributions as temperature varies. In view of this, it is now quite remarkable that the system manages to achieve full quantum coherence (below T_{FL}) at all. Our choice of measures, we believe, go a meaningful way toward providing some understanding of this process.

Inverse Diffusion Constant Analysis

The diffusion constants for charge and spin are given by [135]:

$$D_n = \frac{\sigma(0)}{\chi_n}, \quad D_s = \frac{\sigma(0)}{4\chi_s} \tag{5.14}$$

where $\sigma(0)$ represents the dc conductivity. The temperature-dependent resistivity, defined as $\rho_{dc} = \frac{1}{\sigma(0)}$, is shown for various doping levels in Fig.5.10.

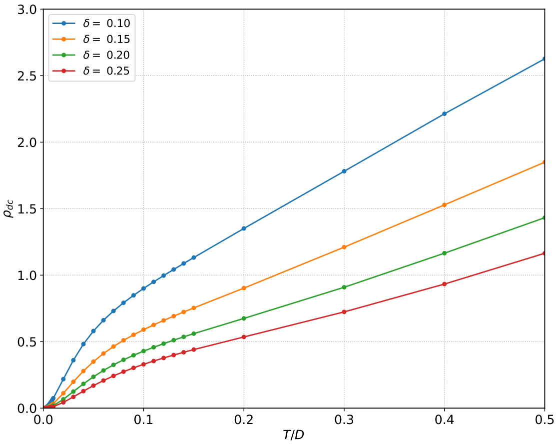

Figure 5.10: Variation of resistivity with Temperature for various doping values at $U = 4$

Examining the inverse of the diffusion constants, $D^{-1}_{n/s}$, derived from transport properties bridges the microscopic features of the diffusion spectrum $P_{n/s}(\omega)$ with the macroscopic behavior of the system. While the characteristic frequency scale $\Omega_{n/s}$, KLD, and kurtosis provide insights into the energy scales, coherence, and distribution properties of the spectrum, D^{-1} offers a more direct measure of transport phenomena such as the resistivity.

In Fig. 5.11, we illustrate the temperature dependence of the inverse diffusion constant for both spin and charge. The behavior for spin shows an initial increase

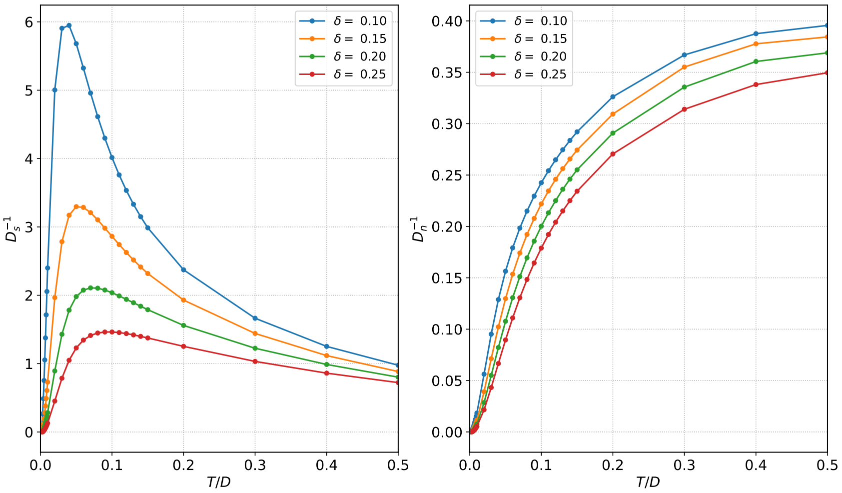

Figure 5.11: Inverse of spin and charge diffusion constant at $U = 4$.

as temperature rises, indicating a growing resistance to transport. This increase is followed by a decrease and eventual saturation at higher temperatures, suggesting a stabilization of spin transport in a more classical regime. In contrast, the inverse diffusion constant for charge consistently increases with temperature before plateauing, implying an increasing resistance that levels off at higher temperatures. Notably, the inverse diffusion constant for charge is about ten times lower than that for spin across the temperature range, highlighting a fundamental difference in transport behavior between the two.

These observations underscore the distinct dynamics governing spin and charge transport. The distinct temperature dependencies suggest that spin excitations may be more prone to coherence loss and scattering, transitioning through regimes of varying transport resistance. In comparison, charge excitations show a smoother shift towards saturation, maintaining a higher degree of mobility despite temperature changes. This disparity aligns with the findings from kurtosis and KLD analyses.

The diffusion constant D itself represents how freely spin or charge moves through the system, linking directly to transport efficiency. The spectrum $P_{n/s}(\omega)$ encapsulates energy dissipation and fluctuation behavior, revealing the scattering mechanisms that influence D. By exploring D^{-1}, we can discern how the specific features of $P_{n/s}(\omega)$—such as peaks, width, and tails—contribute to transport. High kurtosis in $P_{n/s}(\omega)$ suggests concentrated energy dissipation around certain frequencies, leading to reduced scattering and higher mobility (lower D^{-1}). A broader spectrum, by contrast, implies increased scattering and diffusion, resulting in a higher D^{-1} and decreased transport efficiency.

The analysis of D^{-1} in relation to $P_{n/s}(\omega)$ provides further evidence of the decoupling between spin and charge transport. For example, if spin D^{-1} increases more significantly than that of charge with temperature, it signals that spin excitations transit to an incoherent state at a rate distinct from their charge counterparts. This complements kurtosis and KLD findings, which indicate how spin and charge fluctuations achieve quantum coherence at separate scales. This difference is critical for understanding the non-Fermi liquid behavior and it's eventual crossover to a Landau FL, often observed in strongly correlated systems.

This plays a crucial role in interpreting D^{-1} alongside $P_{n/s}(\omega)$, KLD, and kurtosis. As temperature increases, a rising D^{-1} paired with a decreasing kurtosis suggests a transition from sharp, coherent quasiparticle excitations to incoherently diffusing modes. Thus, taken together, these measures offer a comprehensive characterization of how dynamic charge and spin fluctuations evolve and shape the transport properties across the Mott transition in the local approximation for the one-band Hubbard model.

Chapter 6

Summary and Conclusion

6.1 Summary

In this thesis, we investigated the Hubbard model in the strong coupling regime with a dual approach: an analytical treatment based on the limit of infinite onsite repulsion $U = \infty$ in which we developed an approximate self-consistent approach, and a numerical treatment at finite U using the Dynamical Mean Field Theory (DMFT) framework implemented with the Numerical Renormalization Group (NRG) as the impurity solver. The aim was to explore the nature of electron transport and fluctuation dynamics, particularly the crossover from coherent to incoherent regimes and to illuminate the underlying mechanisms driving anomalous transport behavior such as linear-in-T resistivity in correlated metals.

In the first part, we developed a new ECFL-based self-consistent scheme in the $U = \infty$ limit using the Hubbard X-operator formalism. Exploiting the simplifications that emerge in the infinite-dimensional ($d \to \infty$) limit, we derived closed-form expressions for the Dysonian self-energy Σ as a convolution of the single-particle Green's function G with local charge and spin fluctuation correlators, D_N and D_S. These correlators were obtained by expressing them in terms of relevant current-current correlation function using equation of motion. The current-current correlations are in turn obtained by evaluating bubble diagram since the vertex corrections vanish in high dimensions ($d = \infty$). This formulation revealed how incoherent, site-local, and bosonic number and spin fluctuations dynamically affect electron propagation.

A central result of the ECFL analysis was the emergence of a temperature-driven crossover from a coherent Fermi liquid to an incoherent quantum regime (IQR) followed by a "bad metal" regime. Also, we were able to identify energy scales differentiating the quantum and classical regimes of transport. We find that the

IQR hosts linear resistivity in temperature and the resistivity is due to scattering of electrons due to incoherent quantum local charge fluctuations. This region is reminiscent of a strange metal.

Since our treatment of infinite U Hubbard model doesn't differentiate between charge and spin fluctuation. In the second part of the thesis, we numerically studied the Hubbard model at finite U within the DMFT framework using NRG as an impurity solver. In our study, we find that the spin fluctuations become classical at lower temperatures compared to charge fluctuations. In other words, a two-stage decoherence process emerges: spin incoherence precedes charge incoherence. This staggered incoherence leads to the breakdown of Fermi liquid behavior in stages, providing a microscopic basis for strange metallicity and bad metallic transport.

To probe the nature of this crossover and the associated incoherence, we analyzed various metrics: characteristic frequency scales ($\Omega_{n/s}$), Kullback-Leibler divergence (KLD), kurtosis, and inverse diffusion constants. These observables not only confirmed the separation between spin and charge coherence scales but also allowed us to distinguish between quantum-coherent, quantum-incoherent, and classical transport regimes. Spin degrees of freedom were found to become classical at lower temperatures compared to charge, highlighting the differential decoherence and its imprint on transport properties. The kurtosis, in particular, showed drastically sharper features in spin fluctuations compared to charge, indicating a spin-dominated coherence scale.

In the doped Mott insulator, our analysis uncovered isosbestic points (frequencies at which the response functions are invariant with temperature) in both spin and charge spectra suggesting sum-rule constraints or hidden conservation laws at play. These findings prompt further exploration of connections to Luttinger's theorem, compressibility and moment sum rules, and the broader structure of spectral weight transfer across interaction and temperature regimes.

6.2 Conclusion

The combined analytical and numerical investigations presented in this thesis provide a comprehensive picture of spin and charge dynamics in the one-band Hubbard model in both the infinite and finite-U limits. The infinite-U, large-dimensional limit allowed us to formulate a tractable theory where local spin and charge fluctuations emerge as collective bosonic modes influencing electronic coherence. This theory, while approximate, captures essential aspects of strongly correlated transport, particularly the loss of coherence with increasing temperature and the emergence of non-Fermi liquid behavior.

However, this simplification; while powerful, comes with important caveats. In the infinite-U limit, the current is computed within the bubble approximation, which does not distinguish between spin and charge contributions to the current. This makes it difficult to treat spin and charge currents on equal footing and thus suppresses potentially richer vertex-mediated processes that could become important at finite U. Extending the theory to finite-U systems in the same spirit would therefore require going beyond the bubble approximation by including at least partial vertex corrections or self-consistently treating current operators within a two-particle formalism.

In particular, the NRG-based DMFT results suggest that spin and charge fluctuations develop distinct spectral characteristics and coherence scales, and hence should ideally be treated as separate degrees of freedom in transport calculations. Such a treatment would necessitate the development of an extended self-consistent scheme that dynamically couples single-particle self-energies with two-particle response functions—perhaps through the Bethe-Salpeter equations with local vertex functions derived from impurity solvers.

Moreover, our findings indicate that strange metal behavior, characterized by a broad, incoherent continuum of excitations, lack of quasiparticle peaks, and linear-in-T resistivity; may originate from the overlap of quantum-incoherent spin and charge dynamics that have not yet settled into coherent quasiparticle states. This insight could be critical for understanding emergent metallic phases in multi-orbital systems and high-temperature superconductors, where non-Fermi liquid signatures often appear without long-range order.

A promising direction for future work is to generalize the ECFL-based approach to finite U using systematic $1/U$ expansions around the $U = \infty$ limit. Another possibility is to incorporate momentum- or orbital-selectivity into the analysis to study orbital-selective Mott phases (OSMP), where coherence survives in some sectors but not others. Such a “two-fluid” approach may naturally unify the bad metal, strange metal, and Mott insulator regimes in a single coherent framework.

In summary, this thesis offers a multipronged examination of spin and charge dynamics in the Hubbard model and underscores the importance of treating these degrees of freedom distinctly; both conceptually and computationally. The separation of coherence scales, the identification of diffusion crossovers, and the sensitivity of transport to bosonic fluctuation spectra suggest a fundamentally dynamic origin for non-Fermi liquid behavior. Understanding these processes is crucial not only for theoretical modeling but also for interpreting experimental signatures in strongly correlated materials.

Appendix A

X Operators

For a lattice system with one orbital per site, a general state can be described completely in terms of the orbital states at a site i. This set consists of states $|0\rangle$, $|\sigma\rangle$, $|\bar{\sigma}\rangle$ and $|2\rangle$; namely those with no electron, one electron with spin $\sigma(\uparrow)$ or $\bar{\sigma}(\downarrow)$, and two electrons$(\uparrow\downarrow)$. The X operators introduced by Hubbard [20] are all the matrix elements in this Hilbert space; e.g. $X_i^{\sigma 0}$ is $|\sigma\rangle\langle 0|$ for states at site i. They are local Fermi like or Bose like field operators (not canonical Fermi or Bose operators), depending on whether they describe change in local electron number by unity (odd numbers in general) or by zero (even numbers in general) (see the book by Ovchinnikov and Val'kov [36] is on the X operators and its application in condensed matter physics). Commutators/anticommutators of X operators at different sites vanish, while for the the same site, they do not. These results are uniquely determined by the definition of X operators. The results of on site commutation/anticommutation are not c numbers as for canonical fermions and bosons, but are X operators.

The X operators obey the commutation relation

$$\left[X_i^{\alpha\beta}, X_j^{\gamma\delta}\right]_\pm = \left(X_i^{\alpha\delta}\delta_{\beta\gamma} \pm X_i^{\gamma\beta}\delta_{\delta\alpha}\right)\delta_{ij}, \tag{A.1}$$

since at a given site one has

$$X_i^{\alpha\beta}X_i^{\gamma\delta} = \delta_{\beta\gamma}X_i^{\alpha\delta}. \tag{A.2}$$

The basic commutator involving X arises from the Heisenberg equation of motion for the X-operator. It is

$$\begin{aligned} i\partial_t X_i^{\alpha\beta} = i\dot{X}_i^{\alpha\beta} = \left[X_i^{\alpha\beta}, H\right]_- &= -\mu\sum_\sigma\left(X_i^{0\sigma}\delta_\beta\sigma - X_i^{\sigma\beta}\delta_{\sigma\alpha}\right) \\ &\quad + \sum_{jm} t_{jm}\left(\left[X_i^{\alpha\beta}, X_j^{0\sigma}\right]_\pm X_m^{\sigma 0} \pm X_j^{0\sigma}\left[X_m^{\sigma 0}, X_i^{\alpha\beta}\right]_\pm\right). \end{aligned} \tag{A.3}$$

where the upper and lower set of signs are for bosonic and fermionic operators respectively.[1]

The case of $\alpha = 0$ and $\beta = \sigma$, namely the fermionic operator $X_i^{0\sigma}$ is relevant for the equation of motion of the single particle Green's function. We have

$$\left[X_i^{0\sigma}, X_j^{\sigma'0}\right]_+ = \delta_{ij}(\delta_{\sigma\sigma'}X_i^{00} + X_i^{\sigma'\sigma}) = \delta_{ij}B_i^{\sigma\sigma'} \tag{A.4}$$

where $B_i^{\sigma\sigma'}$ is a bosonic operator centred at i. It is a charge fluctuation operator for $\sigma = \sigma'$ and a spin fluctuation operator for $\sigma \neq \sigma'$. Using the compact notation ref.[31], this can be written as

$$\left[X_i^{0\sigma}, X_j^{\sigma'0}\right]_+ = \delta_{ij}(\delta_{\sigma\sigma'}I - \sigma\sigma' X_i^{\bar{\sigma}\bar{\sigma}'}) \tag{A.5}$$

$$i\dot{X}_i^{0\sigma}(t) = -\mu X_i^{0\sigma}(t) + \sum_{m\sigma'} t_{mi} B_i^{\sigma\sigma'}(t) X_m^{0\sigma'}(t), \tag{A.6}$$

and

$$\left[B_i^{\sigma_1\sigma_2}, X_j^{0\sigma_3}\right]_- = -\sigma_1\sigma_2\left[X_i^{\bar{\sigma}_1\bar{\sigma}_2}, X_j^{0\sigma_3}\right]_- = -\sigma_1\sigma_2\delta_{ij}X_i^{0\bar{\sigma}_2}\delta_{\bar{\sigma}_1\sigma_3}. \tag{A.7}$$

In equation (A.6),we notice that there is a novel, local spin flip term due to hopping (last term on the right) present only because of correlation. This involves a spin flip at say site i and a number change (of the spin flipped electron) at site j connected with it via hopping. In the following, we assume (as is common) that $t_{im} = t_{mi}$.

The equation of motion for bosonic operators is illustrated with the example of $\dot{X}_i^{\bar{\sigma}\sigma}$ for which $\alpha = \bar{\sigma}$, $\beta = \sigma$. We have

$$-\dot{X}_i^{\bar{\sigma}\sigma} = \sum_m t_{im}(X_m^{0\sigma}X_i^{\bar{\sigma}0} - X_i^{0\sigma}X_m^{\bar{\sigma}0}). \tag{A.8}$$

For the extremely strongly correlated Fermi liquid (ECFL) where $(U/t) \to \infty$ the doubly occupancy state $|2\rangle$ can be neglected since it has an infinitely high energy. In this limit, the relations satisfied by the Hubbard operators can be written as

$$X_i^{00} + \sum_\sigma X_i^{\sigma\sigma} = I,\, X_i^{\sigma\sigma} + X_i^{\bar{\sigma}\bar{\sigma}} = N_i,\, X_i^{\sigma\sigma} - X_i^{\bar{\sigma}\bar{\sigma}} = 2S_i^z, \tag{A.9}$$

$$X_i^{00} + \sum_\sigma \sigma X_i^{\sigma\sigma} = I - \frac{N_i}{2} + \sigma S_i^z. \tag{A.10}$$

---

[1] We use the (nearly standard) convention that $[A, B]_\pm$ is an anticommutator for the + sign and the commutator for the - sign.

where I is the identity operator, and N_i and S_i^z are respectively the number and the z component of spin operators at site i. Since the system is homogeneous, the thermodynamic average at any site i is independent of i. We define n and m as the average number and the average z component of the magnetization, namely $n = \langle N_i \rangle$ and $m = \langle S_i^z \rangle$. We assume that the system is paramagnetic, so that $m = 0$ and $\langle X^{\bar{\sigma}\bar{\sigma}} \rangle = \langle X^{\sigma\sigma} \rangle = n/2$, and that it is spin isotropic. A commonly occurring quantity is

$$\langle B_i^{\sigma\sigma} \rangle = \left\langle I - \frac{N_i}{2} + S_i^z \right\rangle = \left(1 - \frac{n}{2}\right) = \left(\frac{1+\delta}{2}\right) = Q. \tag{A.11}$$

Appendix B

Equation of motion for D_N^+ and D_S^+

D^R in terms of the N and S_z operators can be derived using $B^{\sigma\sigma} = X^{00} + X^{\sigma\sigma} = 1 - \frac{N}{2} + S_z,\ B^{\sigma\bar{\sigma}} = X^{\sigma\bar{\sigma}} = S^+$ for B-operator.

$$D^R(t,t') = \langle\langle B^{\sigma\sigma}(t)|B^{\sigma\sigma}(t')\rangle\rangle + \langle\langle B^{\sigma\bar{\sigma}}(t)|B^{\bar{\sigma}\sigma}(t')\rangle\rangle \tag{B.1}$$

$$\begin{aligned} D^R(t,t') = \frac{1}{4}\langle\langle N(t)|N(t')\rangle\rangle + \langle\langle S_z(t)|S_z(t')\rangle\rangle + \langle\langle S^+(t)|S^-(t')\rangle\rangle \\ - \frac{1}{2}\langle\langle N(t)|S_z(t')\rangle\rangle - \frac{1}{2}\langle\langle S_z(t)|N(t')\rangle\rangle \end{aligned} \tag{B.2}$$

$$D^R(t,t') = \frac{1}{4}\langle\langle N(t)|N(t')\rangle\rangle + \frac{3}{2}\langle\langle S^+(t)|S^-(t')\rangle\rangle - \frac{1}{2}\langle\langle N(t)|S^z(t')\rangle\rangle - \frac{1}{2}\langle\langle S^z(t)|N(t')\rangle\rangle \tag{B.3}$$

Since $\langle\langle S^+|S^-\rangle\rangle = \langle\langle S_x|S_x\rangle\rangle + \left\langle\left\langle S_y|S_y\right\rangle\right\rangle = 2\langle\langle S_z|S_z\rangle\rangle$ in isotropic phase. The third and fourth terms would vanish in the paramagnetic phase.

$$D^R(t,t') = \frac{1}{4}\langle\langle N(t)|N(t')\rangle\rangle + \frac{3}{2}\langle\langle S^+(t)|S^-(t')\rangle\rangle \tag{B.4}$$

Since,

$$\begin{aligned} D_N^+(t-t') &= -i\theta(t-t')\langle N(t)N(t')\rangle \\ D_S^+(t-t') &= -i\theta(t-t')\langle S^+(t)S^-(t')\rangle \end{aligned} \tag{B.5}$$

To develop the equation of motion for D_N^+ we start by differentiating it with respect to t

$$\begin{aligned} & i\partial_t D_N^+(t-t') = \delta(t-t')\left\langle NN\right\rangle - i\theta(t-t')\left\langle i\dot{N}(t)N(t')\right\rangle \\ \Longrightarrow\ & i\partial_t D_N^+(t-t') = \delta(t-t')n - i\theta(t-t')\left\langle i\dot{N}(t)N(t')\right\rangle \\ \Longrightarrow\ & i\partial_t D_N^+(t-t') = \delta(t-t')n + \tilde{D}_N^+(t-t') \end{aligned} \tag{B.6}$$

where n is the number density and

$$\tilde{D}_N^+(t-t') = -i\theta(t-t')\left\langle i\dot{N}(t)N(t')\right\rangle \tag{B.7}$$

Now, we develop an equation of motion for $\tilde{D}_N^+$ by differentiating it with respect to t'

$$i\partial_{t'}\tilde{D}_N^+(t-t') = -\delta(t-t')\left\langle i\dot{N}(t)N(t)\right\rangle + i\theta(t-t')\left\langle \dot{N}(t)\dot{N}(t')\right\rangle \tag{B.8}$$

First term in the above expression is zero which can be easily seen from the fact that the number operator acting on number basis (in which we are taking the trace) will give us the same state so $\left\langle \dot{N}N\right\rangle = \left\langle \dot{N}\right\rangle$ which is 0 in equilibrium , so we get

$$\begin{aligned} i\partial_{t'}\tilde{D}_N^+(t-t') &= i\theta(t-t')\left\langle \dot{N}(t)\dot{N}(t')\right\rangle \\ i\partial_{t'}\tilde{D}_N^+(t-t') &= -\chi_{JJ}^+(t-t') \end{aligned} \tag{B.9}$$

where we have defined

$$\chi_{JJ}^+(t-t') = -i\theta(t-t')\left\langle \dot{N}(t)\dot{N}(t')\right\rangle \tag{B.10}$$

We define the Fourier transform as (in the same manner for all the terms)

$$D_N^+(t-t') = \frac{1}{2\pi}\int \mathrm{d}(t-t')\, e^{-i\omega(t-t')} D_N^+(\omega) \tag{B.11}$$

Fourier transforming and combining equations (B.6) and (B.9) we get

$$D_N^+(\omega) = \frac{1}{\left[\frac{\omega}{n} - \frac{\chi_{JJ}^+(\omega)}{n^2}\right]} \tag{B.12}$$

Similarly, for D_S^+

$$\begin{aligned} i\partial_t D_S^+(t-t') &= \delta(t-t')\left\langle S^+S^-\right\rangle + \tilde{D}_S^+(t-t') \\ \left\langle S^+S^-\right\rangle &= 2\left\langle S^zS^z\right\rangle = \frac{\left\langle X^{\sigma\sigma} + X^{\bar{\sigma}\bar{\sigma}}\right\rangle}{2} = \frac{n}{2} \\ \Longrightarrow\ i\partial_t D_S^+(t-t') &= \delta(t-t')\frac{n}{2} + \tilde{D}_S^+(t-t') \end{aligned} \tag{B.13}$$

where

$$\tilde{D}_S^+(t-t') = -i\theta(t-t')\left\langle i\dot{S}^+(t)S^-(t')\right\rangle \tag{B.14}$$

$$i\partial_{t'}\tilde{D}_S^+(t-t') = -\delta(t-t')\left\langle i\dot{S}^+S^-\right\rangle + i\theta(t-t')\left\langle \dot{S}^+(t)\dot{S}^-(t')\right\rangle \tag{B.15}$$

To determine the $\left\langle i\dot{S}^+S^-\right\rangle$ we go back to the definition $S^+ = X^{\sigma\bar{\sigma}}$ and $S^- = X^{\bar{\sigma}\sigma}$. using Heisenberg equation of motion, we find

$$i\dot{X}^{\sigma\bar{\sigma}} = \sum_j t_{ij}\Big(X_i^{\sigma 0}X_j^{0\bar{\sigma}} - X_i^{0\bar{\sigma}}X_j^{\sigma 0}\Big) \tag{B.16}$$

using this relation, we can find $i\dot{S}^+S^- = i\dot{X}^{\sigma\bar{\sigma}}X_i^{\bar{\sigma}\sigma}$ to be

$$i\dot{S}^+S^- = \sum_j t_{ij}\Big(X_i^{\sigma 0}X_j^{0\sigma} - X_j^{\sigma 0}X_i^{0\sigma}\Big) \tag{B.17}$$

rhs of the above equation is same as the current operator, hence $\left\langle i\dot{S}^+S^-\right\rangle = 0$. so, we have

$$\begin{aligned}
i\partial_{t'}\tilde{D}_S^+(t-t') &= i\theta(t-t')\left\langle \dot{S}^+(t)\dot{S}^-(t')\right\rangle \\
i\partial_{t'}\tilde{D}_S^+(t-t') &= -\chi^+_{J_sJ_s}(t-t') \\
\chi^+_{J_sJ_s}(t-t') &= -i\theta(t-t')\left\langle \dot{S}^+(t)\dot{S}^-(t')\right\rangle
\end{aligned} \tag{B.18}$$

Fourier transforming and combining equations (B.13) and (B.18) , we get

$$D_S^+(\omega) = \frac{1}{\left[\frac{\omega}{n/2} - \frac{\chi^+_{J_sJ_s}(\omega)}{n^2/4}\right]} \tag{B.19}$$

Appendix C

Current current correlation function for spin and charge

In imaginary time, we can write the time ordered current-current correlation functions for charge and spin as

$$\chi_N(\tau,\tau') = -\left\langle T_\tau J_c(\tau) J_c(\tau')\right\rangle, \quad \chi_S(\tau,\tau') = -\left\langle T_\tau J_s(\tau) J_s(\tau')\right\rangle \tag{C.1}$$

$$J_c = \frac{1}{N}\sum_{k,\sigma} v_k X_k^{0\sigma} X_k^{\sigma 0}, \quad J_s = \frac{1}{N}\sum_{k} v_k X_k^{0\sigma} X_k^{\bar{\sigma}0} \tag{C.2}$$

T_τ is the time ordering operator. The contribution to bubble diagram in imaginary frequency is

$$\chi_N(i\nu_n) = \frac{1}{N}\sum_{\sigma,k,m} v_k^2 G^{\sigma\sigma}(k,i\omega_m) G^{\sigma\sigma}(k,i\nu_n+i\omega_m) \tag{C.3}$$

$$\chi_S(i\nu_n) = \frac{1}{N}\sum_{k,m} v_k^2 G^{\sigma\sigma}(k,i\omega_m) G^{\bar{\sigma}\bar{\sigma}}(k,i\nu_n+i\omega_m) \tag{C.4}$$

$i\omega_n = \frac{(2n+1)\pi}{\beta}$, $i\nu_n = \frac{2n\pi}{\beta}$ and β is inverse temperature. Since in the paramagnetic phase $G^{\sigma\sigma} = G^{\bar{\sigma}\bar{\sigma}}$

$$\chi_N(i\nu_n) = \frac{2}{N}\sum_{k,m} v_k^2 G^{\sigma\sigma}(k,i\omega_m) G^{\sigma\sigma}(k,i\nu_n+i\omega_m) \tag{C.5}$$

$$\chi_S(i\nu_n) = \frac{1}{N}\sum_{k,m} v_k^2 G^{\sigma\sigma}(k,i\omega_m) G^{\sigma\sigma}(k,i\nu_n+i\omega_m) \tag{C.6}$$

By writing the spectral representation for the Green's function $G(k,i\omega_n)$ and doing analytic continuation, we obtain

$$\chi^R(\omega) = \frac{1}{N}\sum_k \iint \mathrm{d}\omega_1 \mathrm{d}\omega_2 \frac{\rho_G(k,\omega_1)\rho_G(k,\omega_2) v_k^2}{\omega+\omega_1-\omega_2+i\eta}\{n_F(\omega_1)-n_F(\omega_2)\} \tag{C.7}$$

and $\chi_N^R(\omega) = 2\chi^R(\omega)$, $\chi_S^R(\omega) = \chi^R(\omega)$.

Appendix D

Self energy low temperature behaviour

The low temperature and low frequency behaviour of the scattering function, $\Gamma(\omega, T)$ is

$$\begin{aligned}\Gamma(\omega,T) &= -\Im\Sigma(\omega,T) = \pi\int_{-\infty}^{\infty}\mathrm{d}y\ \rho_G(\omega-y)\ \rho_D(y)\ \left[n_F(y-\omega)+n_B(y)\right]\\ &\approx \pi\int_{-\infty}^{\infty}\mathrm{d}y\ \rho_G(-y)\ \rho_D(y)\ \left[n_F(y)+\tfrac{\omega^2}{2}n_F^{''}(y)+n_B(y)\right] = I_1+I_2\end{aligned}$$

where

$$I_1 = \pi\int_{-\infty}^{\infty}\mathrm{d}y\ \rho_G(-y)\ \rho_D(y)\ \left[n_F(y)+n_B(y)\right]$$
$$= \pi\int_{0}^{\infty}\mathrm{d}y\ \left(\rho_G(-y)+\rho_G(y)\right)\ \rho_D(y)\ \left(n_F(y)+n_B(y)\right)$$

$\rho_D(y)$ is an odd function. We can expand around $y = 0$, $\rho_D(y) = Ay$, we obtain

$$I_1 = 2A\pi\rho_G(0)\int_0^{\infty}\mathrm{d}y\ y\ \left(n_F(y)+n_B(y)\right) = \frac{\pi}{2}A\rho_G(0)\pi^2T^2 \tag{D.1}$$

And

$$I_2 = -\frac{\pi\omega^2}{2}\int_{-\infty}^{\infty}\mathrm{d}y\ \rho_G(-y)\ \rho_D(y)\ \left(-n_F^{''}(y)\right) = \frac{\pi\omega^2}{2}A\rho_G(0) \tag{D.2}$$

$\Gamma(\omega, T)$ at low temperature and low frequency is

$$\Gamma(\omega,T) = \tfrac{\pi}{2}\rho_G(0)A(\pi^2T^2+\omega^2) \tag{D.3}$$

Appendix E

Evaluating Low-Frequency Behavior with Cumulative Distribution Functions

To quantify the accuracy of low-frequency behavior in the charge and spin diffusion spectra, we analyze the cumulative distribution function $C(\omega)$:

$$C(\omega) = \int_0^{\omega} d\omega' \, \mathrm{Im}\chi(\omega'), \tag{E.1}$$

where $\mathrm{Im}\chi(\omega)$ is the imaginary part of the susceptibility for both charge and spin. In a metallic phase, characterized as a Fermi liquid, $\mathrm{Im}\chi(\omega)$ is expected to display a linear behavior at low frequencies, resulting in a log-log plot slope of $C(\omega)$ approaching 2, indicative of a quadratic dependence.

The DMNRG results for $C(\omega)$, shown in Fig. E.1(a), confirm the expected behavior, maintaining a low-frequency slope close to 2, consistent down to 10^{-6}. The slope analysis in Figs. E.2 and E.4 corroborates this, showing consistency across various U values in the metallic phase. By contrast, the FDM results in Fig. E.1(b) show deviations at low frequencies, mirroring the numerical artofacts found above.

Similar result for spin, depicted in Fig. E.3, reinforces these findings. The DMNRG data in Fig. E.3(a) uphold the expected low-frequency behavior, while FDM results in Fig. E.3(b) exhibit deviations, further highlighting the limitations of FDM.

The consistency of these results confirms DMNRG's superior accuracy in capturing low-frequency spectral behavior, while FDM exhibits numerical artifacts that affect the slope and, consequently, the diffusion spectrum.

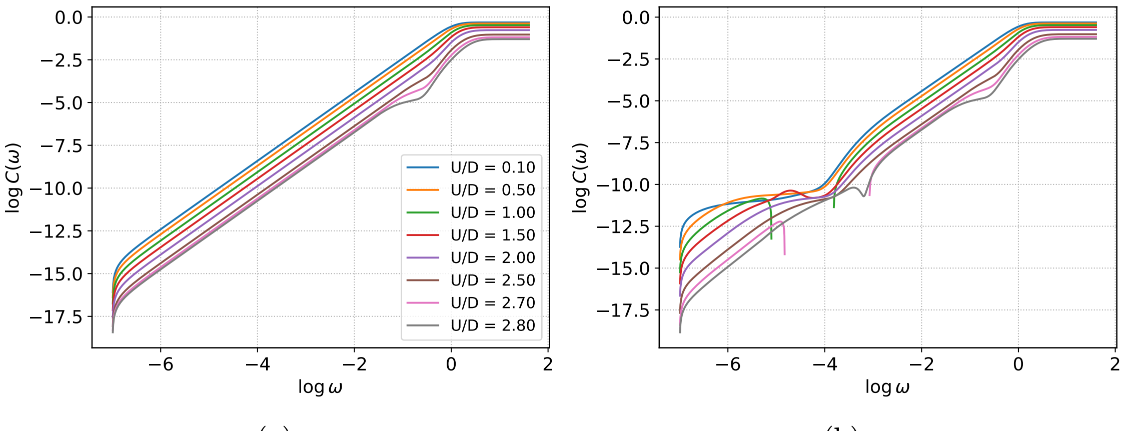

(a)

(b)

Figure E.1: (a) Cumulative distribution function $C(\omega)$ for the charge diffusion spectrum at half-filling using DMNRG at $T/D = 0.001$. (b) Cumulative distribution function for the charge diffusion spectrum using FDM at $T/D = 0.001$.

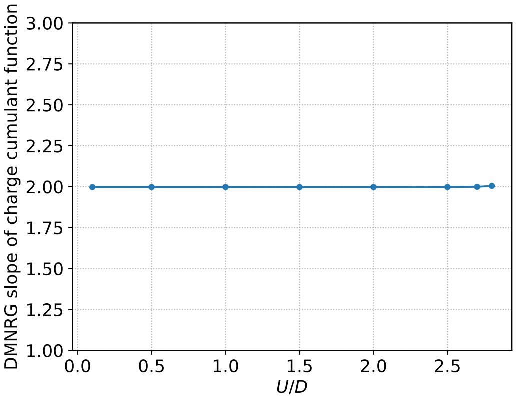

Figure E.2: Fitted slope of $\log C(\omega)$ for the charge cumulant function for $\log \omega$ between -6 and -2 for DMNRG data, illustrating the consistency of the slope across various U values in the metallic phase.

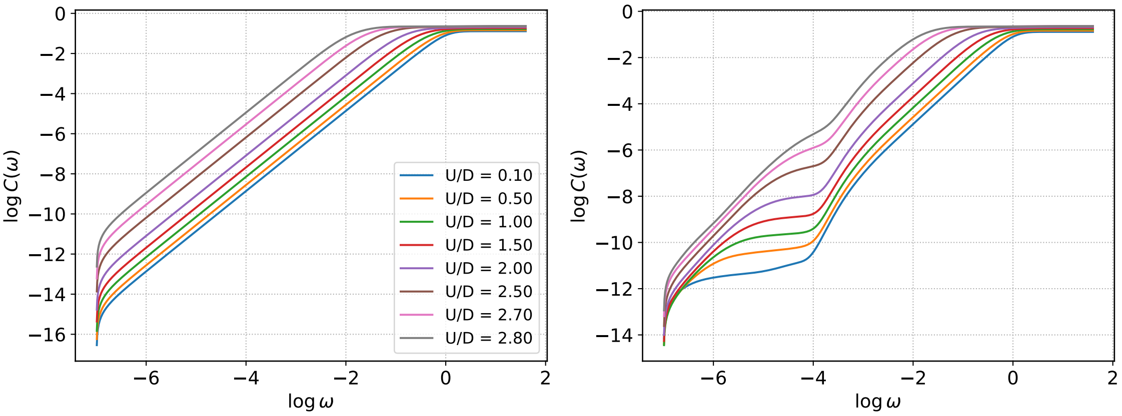

(a) (b)

Figure E.3: (a) Cumulative distribution function $C(\omega)$ for the spin diffusion spectrum at half-filling using DMNRG at $T/D = 0.001$. (b) Cumulative distribution function for the spin diffusion spectrum using FDM at $T/D = 0.001$.

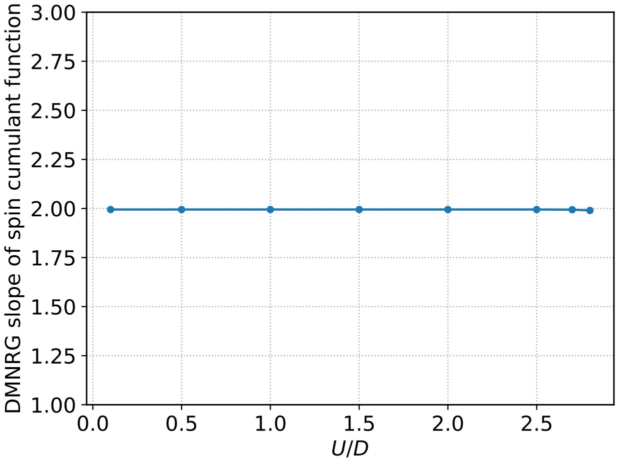

Figure E.4: Fitted slope of $\log C(\omega)$ for the spin cumulant function for $\log\omega$ between -6 and -2 for DMNRG data, illustrating the consistency of the slope across various U values in the metallic phase..

Appendix F

Optimizing the Diffusion Spectrum: Mitigating Artifacts in the FDM Approach

To deepen our understanding of the diffusion spectra and the numerical challenges associated with the Full Density Matrix (FDM) method, we closely examine how the results evolve when calculated across various parameter schemes, We now focus on mitigating the spurious dip observed in FDM results. Specifically, we analyze the charge diffusion spectrum at $\eta = 0$, as illustrated in Fig. 5.2(b). A pronounced dip near $\omega = 0$ is evident, which does not appear in the DMNRG-derived results. We vary the parameter η to observe its effect on the charge diffusion spectrum. Fig. F.1 demonstrates the impact of increasing η on the spurious dip. As η increases, the dip diminishes, indicating that adjusting η can minimize numerical artifacts. Our analysis suggests that an optimal η value of 0.001 strikes a balance, effectively removing the dip while maintaining the essential characteristics of the spectrum. This optimized result aligns closely with the DMNRG results for $\eta = 0$, demonstrating that careful tuning of η can mitigate artifacts without compromising the physical accuracy of the spectrum.

The analysis extends to the spin diffusion spectrum. Unlike the charge spectrum, the spin spectrum's spurious dip can be corrected with smaller adjustments to η, as seen in Fig. F.2. Thus, charge response calculations in FDM are more sensitive to numerical artifacts than their spin counterparts, reflecting differences in how these channels respond to the same numerical treatments.

Figs. 5.2(b) and E.3(b) reinforce that while DMNRG accurately captures the expected diffusion spectra without artificial dips, the FDM approach faces challenges, particularly for $\omega < T$ where quantum and thermal fluctuations dominate. This limitation is due to FDM's inherent difficulties in precisely representing the

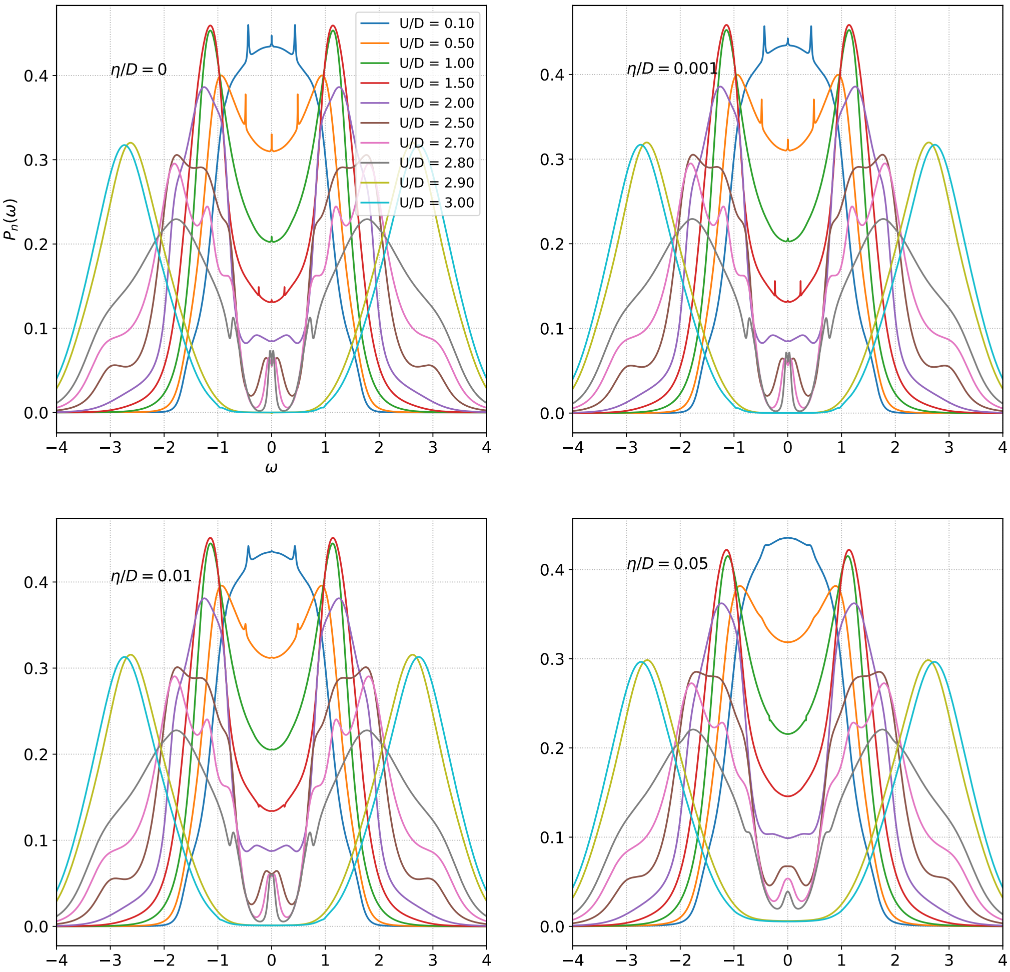

Figure F.1: Charge diffusion spectrum using Pade analytic continuation for four different values of η at half-filling at $T/D = 0.001$.

slope of the susceptibility at small frequencies, leading to artifacts in the diffusion spectrum.

Further examination using data obtained through analytical continuation (Figs. F.1 and F.2) provides additional clarification. Even with very small broadening values η, the analytically continued data does not display the spurious dips seen in the FDM results, reinforcing the conclusion that these dips are numerical artifacts rather than physical phenomena.

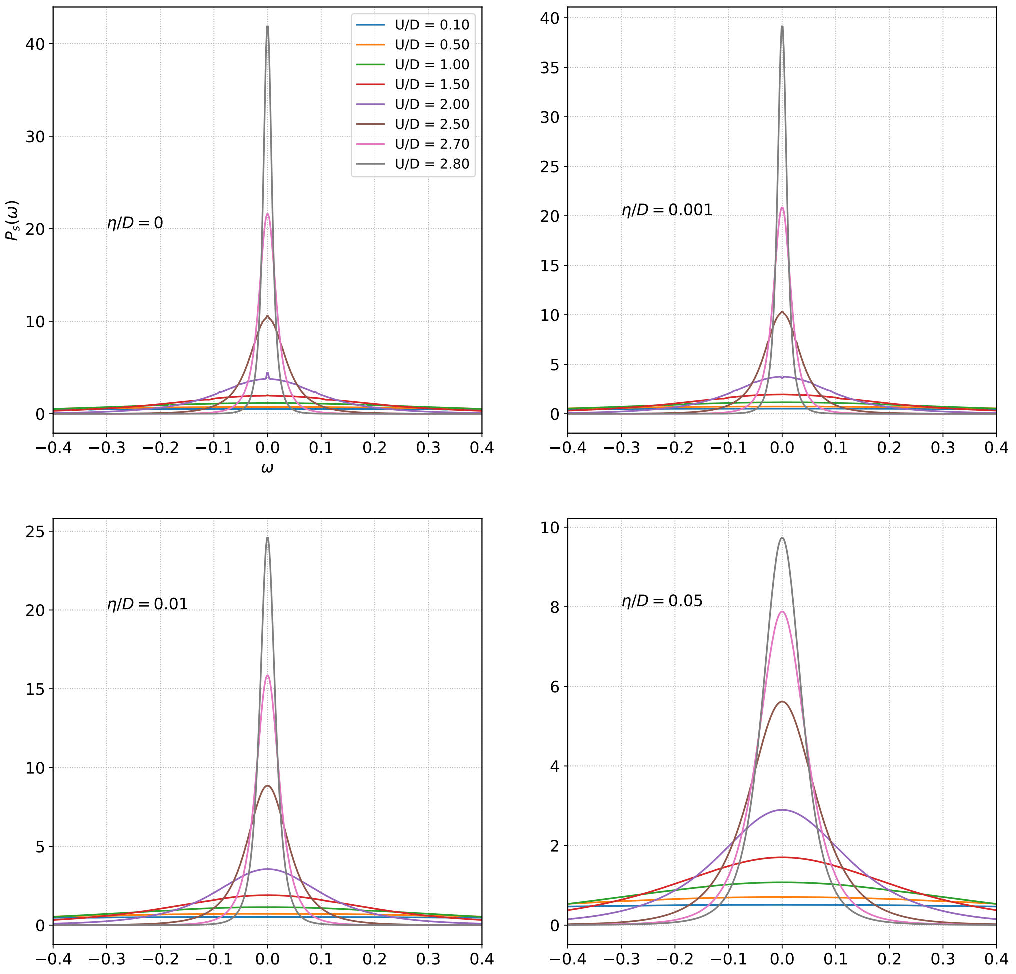

Figure F.2: Spin diffusion spectrum using Pade analytic continuation for four different values of η at half-filling at $T/D = 0.001$.

Bibliography

[1] Bernhard Keimer, Steven A Kivelson, Michael R Norman, Shinichi Uchida, and J Zaanen. From quantum matter to high-temperature superconductivity in copper oxides. *Nature*, 518(7538):179–186, 2015.

[2] Robert A Cooper, Y Wang, Baptiste Vignolle, OJ Lipscombe, Stephen M Hayden, Yoichi Tanabe, Tadashi Adachi, Yoji Koike, Minoru Nohara, Hidenori Takagi, et al. Anomalous criticality in the electrical resistivity of la2–x sr x cuo4. *Science*, 323(5914):603–607, 2009.

[3] Philip W Phillips, Nigel E Hussey, and Peter Abbamonte. Stranger than metals. *Science*, 377(6602):eabh4273, 2022.

[4] Jun Kondo. Resistance minimum in dilute magnetic alloys. *Progress of Theoretical Physics*, 32(1):37–49, 07 1964.

[5] AA Abrikosov. Electron scattering on magnetic impurities in metals and anomalous resistivity effects. *Physics Physique Fizika*, 2(1):5, 1965.

[6] Kenneth G. Wilson. The renormalization group: Critical phenomena and the kondo problem. *Rev. Mod. Phys.*, 47:773–840, Oct 1975.

[7] Horst L. Stormer, Daniel C. Tsui, and Arthur C. Gossard. The fractional quantum hall effect. *Rev. Mod. Phys.*, 71:S298–S305, Mar 1999.

[8] N. F. MOTT. Metal-insulator transition. *Rev. Mod. Phys.*, 40:677–683, Oct 1968.

[9] Yuan Cao, Valla Fatemi, Ahmet Demir, Shiang Fang, Spencer L Tomarken, Jason Y Luo, Javier D Sanchez-Yamagishi, Kenji Watanabe, Takashi Taniguchi, Efthimios Kaxiras, et al. Correlated insulator behaviour at half-filling in magic-angle graphene superlattices. *Nature*, 556(7699):80–84, 2018.

[10] Xiaobo Lu, Petr Stepanov, Wei Yang, Ming Xie, Mohammed Ali Aamir, Ipsita Das, Carles Urgell, Kenji Watanabe, Takashi Taniguchi, Guangyu

Zhang, et al. Superconductors, orbital magnets and correlated states in magic-angle bilayer graphene. *Nature*, 574(7780):653–657, 2019.

[11] Marec Serlin, CL Tschirhart, Hryhoriy Polshyn, Yuxuan Zhang, Jiacheng Zhu, Kenji Watanabe, Takashi Taniguchi, L Balents, and AF Young. Intrinsic quantized anomalous hall effect in a moiré heterostructure. *Science*, 367(6480):900–903, 2020.

[12] Youngjoon Choi, Jeannette Kemmer, Yang Peng, Alex Thomson, Harpreet Arora, Robert Polski, Yiran Zhang, Hechen Ren, Jason Alicea, Gil Refael, et al. Electronic correlations in twisted bilayer graphene near the magic angle. *Nature physics*, 15(11):1174–1180, 2019.

[13] Hryhoriy Polshyn, Matthew Yankowitz, Shaowen Chen, Yuxuan Zhang, K Watanabe, T Taniguchi, Cory R Dean, and Andrea F Young. Large linear-in-temperature resistivity in twisted bilayer graphene. *Nature Physics*, 15(10):1011–1016, 2019.

[14] Yuan Cao, Debanjan Chowdhury, Daniel Rodan-Legrain, Oriol Rubies-Bigorda, Kenji Watanabe, Takashi Taniguchi, T Senthil, and Pablo Jarillo-Herrero. Strange metal in magic-angle graphene with near planckian dissipation. *Physical review letters*, 124(7):076801, 2020.

[15] J George Bednorz and K Alex Müller. Possible high t c superconductivity in the ba- la- cu- o system. *Zeitschrift für Physik B Condensed Matter*, 64(2):189–193, 1986.

[16] P. Hohenberg and W. Kohn. Inhomogeneous electron gas. *Phys. Rev.*, 136:B864–B871, Nov 1964.

[17] W. Kohn and L. J. Sham. Self-consistent equations including exchange and correlation effects. *Phys. Rev.*, 140:A1133–A1138, Nov 1965.

[18] LD Landau. On the theory of the fermi liquid. *Sov. Phys. JETP*, 8(1):70, 1959.

[19] J. Hubbard. Electron correlations in narrow energy bands. *Proceedings of the Royal Society of London. Series A. Mathematical and Physical Sciences*, 276(1365):238–257, nov 1963.

[20] J Hubbard . Electron correlations in narrow energy bands. ii. the degenerate band case. *Proceedings of the Royal Society of London. Series A. Mathematical and Physical Sciences*, 277(1369):237–259, 1964.

[21] J Hubbard. Electron correlations in narrow energy bands iii. an improved solution. *Proceedings of the Royal Society of London. Series A. Mathematical and Physical Sciences*, 281(1386):401–419, 1964.

[22] J. E. Hirsch. Two-dimensional hubbard model: Numerical simulation study. *Phys. Rev. B*, 31:4403–4419, Apr 1985.

[23] S. R. White, D. J. Scalapino, R. L. Sugar, E. Y. Loh, J. E. Gubernatis, and R. T. Scalettar. Numerical study of the two-dimensional hubbard model. *Phys. Rev. B*, 40:506–516, Jul 1989.

[24] T. Schäfer, F. Geles, D. Rost, G. Rohringer, E. Arrigoni, K. Held, N. Blümer, M. Aichhorn, and A. Toschi. Fate of the false mott-hubbard transition in two dimensions. *Phys. Rev. B*, 91:125109, Mar 2015.

[25] Ettore Vitali, Hao Shi, Mingpu Qin, and Shiwei Zhang. Computation of dynamical correlation functions for many-fermion systems with auxiliary-field quantum monte carlo. *Phys. Rev. B*, 94:085140, Aug 2016.

[26] H. J. Schulz. Incommensurate antiferromagnetism in the two-dimensional hubbard model. *Phys. Rev. Lett.*, 64:1445–1448, Mar 1990.

[27] R. Frésard, M. Dzierzawa, and P. Wölfle. Slave-boson approach to spiral magnetic order in the hubbard model. *Europhysics Letters*, 15(3):325, jun 1991.

[28] P. A. Igoshev, M. A. Timirgazin, A. A. Katanin, A. K. Arzhnikov, and V. Yu. Irkhin. Incommensurate magnetic order and phase separation in the two-dimensional hubbard model with nearest- and next-nearest-neighbor hopping. *Phys. Rev. B*, 81:094407, Mar 2010.

[29] N. E. Bickers, D. J. Scalapino, and S. R. White. Conserving approximations for strongly correlated electron systems: Bethe-salpeter equation and dynamics for the two-dimensional hubbard model. *Phys. Rev. Lett.*, 62:961–964, Feb 1989.

[30] Arne Neumayr and Walter Metzner. Renormalized perturbation theory for fermi systems: Fermi surface deformation and superconductivity in the two-dimensional hubbard model. *Phys. Rev. B*, 67:035112, Jan 2003.

[31] B. Sriram Shastry. Extremely correlated quantum liquids. *Phys. Rev. B*, 81:045121, Jan 2010.

[32] S. Shears, E. Perepelitsky, M. Arciniaga, and B. S. Shastry. Extremely correlated fermi liquid theory for the $u = \infty, d = \infty$ hubbard model to $o(\lambda^3)$. *Phys. Rev. B*, 106:035108, Jul 2022.

[33] B. Sriram Shastry. Extremely correlated fermi liquids. *Phys. Rev. Lett.*, 107:056403, Jul 2011.

[34] B. Sriram Shastry. Extremely correlated fermi liquids: The formalism. *Phys. Rev. B*, 87:125124, Mar 2013.

[35] Silke Paschen and Qimiao Si. Quantum phases driven by strong correlations. *Nature Reviews Physics*, 3(1):9–26, 2021.

[36] S G Ovchinnikov and V V Val'kov. *Hubbard Operators in the Theory of Strongly Correlated Electrons.* Imperial College Press, 2004.

[37] Nikolay M. Plakida. *Projection Operator Method*, pages 173–202. Springer Berlin Heidelberg, Berlin, Heidelberg, 2012.

[38] NM Plakida and VS Oudovenko. Electron spectrum in high-temperature cuprate superconductors. *Journal of Experimental and Theoretical Physics*, 104:230–244, 2007.

[39] Xiaoyu Deng, Jernej Mravlje, Rok Žitko, Michel Ferrero, Gabriel Kotliar, and Antoine Georges. How bad metals turn good: Spectroscopic signatures of resilient quasiparticles. *Phys. Rev. Lett.*, 110:086401, Feb 2013.

[40] J. Bardeen, L. N. Cooper, and J. R. Schrieffer. Microscopic theory of superconductivity. *Phys. Rev.*, 106:162–164, Apr 1957.

[41] H. Ding, T. Yokoya, J. C. Campuzano, T. Takahashi, M. Randeria, M. R. Norman, T. Mochiku, K. Kadowaki, and J. Giapintzakis. Spectroscopic evidence for a pseudogap in the normal state of underdoped high-t_c superconductors. *Nature*, 382:51–54, 1996.

[42] A. G. Loeser, Z.-X. Shen, D. S. Dessau, D. S. Marshall, C. H. Park, P. Fournier, and A. Kapitulnik. Excitation gap in the normal state of underdoped bi$_2$sr$_2$cacu$_2$o$_{8+\delta}$. *Science*, 273:325–329, 1996.

[43] M. R. Norman, H. Ding, M. Randeria, J. C. Campuzano, T. Yokoya, T. Takeuchi, T. Takahashi, T. Mochiku, K. Kadowaki, P. Guptasarma, and D. G. Hinks. Destruction of the fermi surface in underdoped high-t_c superconductors. *Nature*, 392:157–160, 1998.

[44] Ch. Renner, B. Revaz, J.-Y. Genoud, K. Kadowaki, and Ø. Fischer. Pseudogap precursor of the superconducting gap in under- and overdoped $\mathrm{bi_2sr_2cacu_2o_{8+\delta}}$. *Phys. Rev. Lett.*, 80:149–152, 1998.

[45] A. Kanigel, M. R. Norman, M. Randeria, U. Chatterjee, S. Souma, A. Kaminski, H. M. Fretwell, S. Rosenkranz, M. Shi, T. Sato, T. Takahashi, Z. Z. Li, H. Raffy, D. Hinks, L. Ozyuzer, and J. C. Campuzano. Evolution of the pseudogap from fermi arcs to the nodal liquid. *Nat. Phys.*, 2:447–451, 2006.

[46] T. Valla, A. V. Fedorov, J. Lee, J. C. Davis, and G. D. Gu. The ground state of the pseudogap in cuprate superconductors. *Science*, 314:1914–1916, 2006.

[47] G. Ghiringhelli, M. Le Tacon, M. Minola, S. Blanco-Canosa, C. Mazzoli, N. B. Brookes, G. M. De Luca, A. Frano, D. G. Hawthorn, F. He, T. Loew, M. Moretti Sala, D. C. Peets, M. Salluzzo, E. Schierle, R. Sutarto, G. A. Sawatzky, E. Weschke, B. Keimer, and L. Braicovich. Long-range incommensurate charge fluctuations in $\mathrm{(y,nd)ba_2cu_3o_{6+x}}$. *Science*, 337:821–825, 2012.

[48] J. Chang, E. Blackburn, A. T. Holmes, N. B. Christensen, J. Larsen, J. Mesot, R. Liang, D. A. Bonn, W. N. Hardy, A. Watenphul, M. V. Zimmermann, E. M. Forgan, and S. M. Hayden. Direct observation of competition between superconductivity and charge density wave order in $\mathrm{yba_2cu_3o_{6.67}}$. *Nat. Phys.*, 8:871–876, 2012.

[49] N. Doiron-Leyraud, C. Proust, D. LeBoeuf, J. Levallois, J.-B. Bonnemaison, R. Liang, D. A. Bonn, W. N. Hardy, and L. Taillefer. Quantum oscillations and the fermi surface in an underdoped high-t_c superconductor. *Nature*, 447:565–568, 2007.

[50] P. A. Lee, N. Nagaosa, and X.-G. Wen. Doping a mott insulator: Physics of high-temperature superconductivity. *Rev. Mod. Phys.*, 78:17–85, 2006.

[51] H. Alloul, T. Ohno, and P. Mendels. 89y nmr evidence for a pseudogap in the normal state of underdoped yba2cu3o6+x. *Phys. Rev. Lett.*, 63:1700–1703, 1989.

[52] W. W. Warren, R. E. Walstedt, G. F. Brennert, R. J. Cava, R. Tycko, R. F. Bell, and G. Dabbagh. Cu spin dynamics and superconducting precursor

effects in planes above tc in yba2cu3o6.7. *Phys. Rev. Lett.*, 62:1193–1196, 1989.

[53] T. Timusk and B. Statt. The pseudogap in high-temperature superconductors: an experimental survey. *Rep. Prog. Phys.*, 62:61–122, 1999.

[54] A. Damascelli, Z. Hussain, and Z.-X. Shen. Angle-resolved photoemission studies of the cuprate superconductors. *Rev. Mod. Phys.*, 75:473–541, 2003.

[55] S. Hüfner, M. A. Hossain, A. Damascelli, and G. A. Sawatzky. Two gaps make a high-temperature superconductor? *Rep. Prog. Phys.*, 71:062501, 2008.

[56] Ø. Fischer, M. Kugler, I. Maggio-Aprile, C. Berthod, and C. Renner. Scanning tunneling spectroscopy of high-temperature superconductors. *Rev. Mod. Phys.*, 79:353–419, 2007.

[57] V. J. Emery and S. A. Kivelson. Importance of phase fluctuations in superconductors with small superfluid density. *Nature*, 374:434–437, 1995.

[58] C. M. Varma. Non-fermi-liquid states and pairing instability of a general model of copper oxide metals. *Phys. Rev. B*, 55:14554–14580, 1997.

[59] S. Chakravarty, R. B. Laughlin, D. K. Morr, and C. Nayak. Hidden order in the cuprates. *Phys. Rev. B*, 63:094503, 2001.

[60] Thomas Maier, Mark Jarrell, Thomas Pruschke, and Matthias H. Hettler. Quantum cluster theories. *Rev. Mod. Phys.*, 77:1027–1080, Oct 2005.

[61] John M Ziman. *Electrons and phonons: the theory of transport phenomena in solids.* Oxford university press, 2001.

[62] M. Gurvitch and A. T. Fiory. Resistivity of $\mathrm{la}_{1.825}\mathrm{sr}_{0.175}\mathrm{cuo}_4$ and $\mathrm{yba}_2\mathrm{cu}_3\mathrm{o}_7$ to 1100 k: Absence of saturation and its implications. *Phys. Rev. Lett.*, 59:1337–1340, Sep 1987.

[63] S. Martin, A. T. Fiory, R. M. Fleming, L. F. Schneemeyer, and J. V. Waszczak. Normal-state transport properties of $\mathrm{bi}_{2+x}\mathrm{sr}_{2-y}\mathrm{cuo}_{6+\square}$ crystals. *Phys. Rev. B*, 41:846–849, Jan 1990.

[64] H. Takagi, B. Batlogg, H. L. Kao, J. Kwo, R. J. Cava, J. J. Krajewski, and W. F. Peck. Systematic evolution of temperature-dependent resistivity in $\mathrm{la}_{2-x}\mathrm{sr}_x\mathrm{cuo}_4$. *Phys. Rev. Lett.*, 69:2975–2978, Nov 1992.

[65] N. E. Hussey, H. Gordon-Moys, J. Kokalj, and R. H. McKenzie. Generic strange-metal behaviour of overdoped cuprates. *J. Phys. Conf. Series*, 449:012004, 2013.

[66] A. F. Ioffe and A. R. Regel. Non-crystalline, amorphous, and liquid electronic semiconductors. *Prog. Semicond.*, 4:237–291, 1960.

[67] M. Gurvitch. Ioffe-regel criterion and resistivity of metals. *Phys. Rev. B*, 24:7404–7407, Dec 1981.

[68] NE Hussey‖, K Takenaka, and H Takagi. Universality of the mott–ioffe–regel limit in metals. *Philosophical Magazine*, 84(27):2847–2864, 2004.

[69] A. Carrington, A. P. Mackenzie, C. T. Lin, and J. R. Cooper. Temperature dependence of the hall angle in single crystal $\mathrm{yba}_2(\mathrm{cu}_{1-x}\mathrm{co}_x)_3\mathrm{o}_{7-\delta}$. *Phys. Rev. Lett.*, 69:2855–2858, 1992.

[70] J. M. Harris, Y. F. Yan, P. Matl, N. P. Ong, P. W. Anderson, T. Kimura, and K. Kitazawa. Violation of Kohler's rule in the normal-state magnetoresistance of $\mathrm{YBa}_2\mathrm{Cu}_3\mathrm{O}_{7-\delta}$ and $\mathrm{La}_{2-x}\mathrm{Sr}_x\mathrm{CuO}_4$. *Phys. Rev. Lett.*, 75:1391–1394, Aug 1995.

[71] R. Lyu, Z. Tuchfeld, N. Verma, H. Tian, K. Watanabe, T. Taniguchi, C. N. Lau, M. Randeria, and M. Bockrath. Strange metal behavior of the hall angle in twisted bilayer graphene. *Phys. Rev. B*, 103:245424, 2021.

[72] C. M. Varma, P. B. Littlewood, S. Schmitt-Rink, E. Abrahams, and A. E. Ruckenstein. Phenomenology of the normal state of cu-o high-temperature superconductors. *Phys. Rev. Lett.*, 63:1996–1999, Oct 1989.

[73] P. B. Littlewood and C. M. Varma. Phenomenology of the normal and superconducting states of a marginal fermi liquid (invited). *Journal of Applied Physics*, 69(8):4979–4984, 04 1991.

[74] AJ Millis. Effect of a nonzero temperature on quantum critical points in itinerant fermion systems. *Physical Review B*, 48(10):7183, 1993.

[75] Ar Abanov, Andrey V Chubukov, and Jörg Schmalian. Quantum-critical theory of the spin-fermion model and its application to cuprates: Normal state analysis. *Advances in Physics*, 52(3):119–218, 2003.

[76] Philipp Gegenwart, Qimiao Si, and Frank Steglich. Quantum criticality in heavy-fermion metals. *nature physics*, 4(3):186–197, 2008.

[77] Hilbert v Löhneysen, Achim Rosch, Matthias Vojta, and Peter Wölfle. Fermi-liquid instabilities at magnetic quantum phase transitions. *Reviews of Modern Physics*, 79(3):1015–1075, 2007.

[78] C. M. Varma. Quantum-critical fluctuations in 2d metals: strange metals and superconductivity in antiferromagnets and in cuprates. *Rep. Prog. Phys.*, 79:082501, 2016.

[79] Xiao Yan Xu, Avraham Klein, Kai Sun, Andrey V Chubukov, and Zi Yang Meng. Identification of non-fermi liquid fermionic self-energy from quantum monte carlo data. *npj Quantum Materials*, 5(1):65, 2020.

[80] Peter Cha, Nils Wentzell, Olivier Parcollet, Antoine Georges, and Eun-Ah Kim. Linear resistivity and sachdev-ye-kitaev (syk) spin liquid behavior in a quantum critical metal with spin-1/2 fermions. *Proceedings of the National Academy of Sciences*, 117(31):18341–18346, 2020.

[81] Philipp T Dumitrescu, Nils Wentzell, Antoine Georges, and Olivier Parcollet. Planckian metal at a doping-induced quantum critical point. *arXiv preprint arXiv:2103.08607*, 2021.

[82] D. van der Marel, H. J. A. Molegraaf, J. Zaanen, Z. Nussinov, F. Carbone, A. Damascelli, H. Eisaki, M. Greven, P. H. Kes, and M. Li. Quantum critical behaviour in a high-tc superconductor. *Nature*, 425(6955):271–274, 2003.

[83] Subir Sachdev and Jinwu Ye. Gapless spin-fluid ground state in a random quantum heisenberg magnet. *Phys. Rev. Lett.*, 70:3339–3342, May 1993.

[84] Alexei Kitaev. A simple model of quantum holography (part 2). *Entanglement in strongly-correlated quantum matter*, page 38, 2015.

[85] Haoyu Guo, Yingfei Gu, and Subir Sachdev. Transport and chaos in lattice sachdev-ye-kitaev models. *Phys. Rev. B*, 100:045140, Jul 2019.

[86] Aavishkar A. Patel and Subir Sachdev. Theory of a planckian metal. *Phys. Rev. Lett.*, 123:066601, Aug 2019.

[87] Aavishkar A. Patel, Haoyu Guo, Ilya Esterlis, and Subir Sachdev. Universal theory of strange metals from spatially random interactions. *Science*, 381(6659):790–793, 2023.

[88] Chenyuan Li, Davide Valentinis, Aavishkar A. Patel, Haoyu Guo, Jörg Schmalian, Subir Sachdev, and Ilya Esterlis. Strange metal and superconductor in the two-dimensional yukawa-sachdev-ye-kitaev model. *Phys. Rev. Lett.*, 133:186502, Oct 2024.

[89] Aavishkar A. Patel, Peter Lunts, and Subir Sachdev. Localization of overdamped bosonic modes and transport in strange metals. *Proceedings of the National Academy of Sciences*, 121(14):e2402052121, 2024.

[90] Peter Cha, Aavishkar A. Patel, Emanuel Gull, and Eun-Ah Kim. Slope invariant t-linear resistivity from local self-energy. *Phys. Rev. Res.*, 2:033434, Sep 2020.

[91] Andrew Hardy, Olivier Parcollet, Antoine Georges, and Aavishkar A. Patel. Enhanced strange metallicity due to hubbard-u coulomb repulsion. *Phys. Rev. Lett.*, 134:036502, Jan 2025.

[92] Hongyun Zhang, Tommaso Pincelli, Chris Jozwiak, Takeshi Kondo, Ralph Ernstorfer, Takafumi Sato, and Shuyun Zhou. Angle-resolved photoemission spectroscopy. *Nature Reviews Methods Primers*, 2(1):54, 2022.

[93] Hideaki Iwasawa. High-resolution angle-resolved photoemission spectroscopy and microscopy. *Electronic Structure*, 2(4):043001, 2020.

[94] Frank MF de Groot, Maurits W Haverkort, Hebatalla Elnaggar, Amélie Juhin, Ke-Jin Zhou, and Pieter Glatzel. Resonant inelastic x-ray scattering. *Nature Reviews Methods Primers*, 4(1):45, 2024.

[95] Luuk JP Ament, Michel Van Veenendaal, Thomas P Devereaux, John P Hill, and Jeroen Van Den Brink. Resonant inelastic x-ray scattering studies of elementary excitations. *Reviews of Modern Physics*, 83(2):705–767, 2011.

[96] Akio Kotani and Shik Shin. Resonant inelastic x-ray scattering spectra for electrons in solids. *Reviews of Modern Physics*, 73(1):203, 2001.

[97] J Rossat-Mignod, LP Regnault, C Vettier, P Burlet, JY Henry, and G Lapertot. Investigation of the spin dynamics in yba2cu3o6+ x by inelastic neutron scattering. *Physica B: Condensed Matter*, 169(1-4):58–65, 1991.

[98] Ryogo Kubo. Statistical-mechanical theory of irreversible processes. i. general theory and simple applications to magnetic and conduction problems. *Journal of the Physical Society of Japan*, 12(6):570–586, 1957.

[99] K. Sheshadri, D. Malterre, A. Fujimori, and A. Chainani. Connecting the one-band and three-band hubbard models of cuprates via spectroscopy and scattering experiments. *Phys. Rev. B*, 107:085125, Feb 2023.

[100] F.Gebhard and M.C.Gutzwiller. Gutzwillerwavefunction. *Scholarpedia*, 2009.

[101] B. Edegger, V. N. Muthukumar, and C. Gros. Gutzwiller–rvb theory of high-temperature superconductivity: Results from renormalized mean-field theory and variational monte carlo calculations. *Advances in Physics*, 56(6):927–1033, 2007.

[102] L.P. Kadanoff. *Quantum Statistical Mechanics.* CRC Press, 1989.

[103] Andre-Marie Tremblay. The many-body problem, from perturbation theory to dynamical-mean field theory, 2017.

[104] Hazime Mori. Transport, Collective Motion, and Brownian Motion*). *Progress of Theoretical Physics*, 33(3):423–455, 03 1965.

[105] D. Forster. *Hydrodynamic Fluctuations, Broken Symmetry, And Correlation Functions (1st ed.).* CRC Press, 1990.

[106] D N Zubarev. Double-time green functions in statistical physics. *Soviet Physics Uspekhi*, 3(3):320, mar 1960.

[107] Antoine Georges, Gabriel Kotliar, Werner Krauth, and Marcelo J. Rozenberg. Dynamical mean-field theory of strongly correlated fermion systems and the limit of infinite dimensions. *Rev. Mod. Phys.*, 68:13–125, Jan 1996.

[108] M. Lee et al. Large enhancement of the thermopower in naxcoo2 at high na doping. *Nature Materials*, 5:537–540, 2006.

[109] Subroto Mukerjee and Joel E. Moore. Doping dependence of thermopower and thermoelectricity in strongly correlated materials. *Applied Physics Letters*, 90(11):112107, 03 2007.

[110] Ali A. Husain, Matteo Mitrano, Melinda S. Rak, Samantha Rubeck, Bruno Uchoa, Katia March, Christian Dwyer, John Schneeloch, Ruidan Zhong, G. D. Gu, and Peter Abbamonte. Crossover of charge fluctuations across the strange metal phase diagram. *Phys. Rev. X*, 9:041062, Dec 2019.

[111] Götz Seibold, Riccardo Arpaia, Ying Ying Peng, Roberto Fumagalli, Lucio Braicovich, Carlo Di Castro, Marco Grilli, Giacomo Claudio Ghiringhelli, and Sergio Caprara. Strange metal behaviour from charge density fluctuations in cuprates. *Communications Physics*, 4(1):7, 2021.

[112] M. H. Hettler, A. N. Tahvildar-Zadeh, M. Jarrell, T. Pruschke, and H. R. Krishnamurthy. Nonlocal dynamical correlations of strongly interacting electron systems. *Phys. Rev. B*, 58:R7475–R7479, Sep 1998.

[113] M. H. Hettler, M. Mukherjee, M. Jarrell, and H. R. Krishnamurthy. Dynamical cluster approximation: Nonlocal dynamics of correlated electron systems. *Phys. Rev. B*, 61:12739–12756, May 2000.

[114] Gabriel Kotliar, Sergej Y. Savrasov, Gunnar Pálsson, and Giulio Biroli. Cellular dynamical mean field approach to strongly correlated systems. *Phys. Rev. Lett.*, 87:186401, Oct 2001.

[115] X. Y. Zhang, M. J. Rozenberg, and G. Kotliar. Mott transition in the $d=\infty$ hubbard model at zero temperature. *Phys. Rev. Lett.*, 70:1666–1669, Mar 1993.

[116] H. Park, K. Haule, and G. Kotliar. Cluster dynamical mean field theory of the mott transition. *Phys. Rev. Lett.*, 101:186403, Oct 2008.

[117] O. Parcollet, G. Biroli, and G. Kotliar. Cluster dynamical mean field analysis of the mott transition. *Phys. Rev. Lett.*, 92:226402, Jun 2004.

[118] Walter Hofstetter. Generalized numerical renormalization group for dynamical quantities. *Phys. Rev. Lett.*, 85:1508–1511, Aug 2000.

[119] Andreas Weichselbaum and Jan von Delft. Sum-rule conserving spectral functions from the numerical renormalization group. *Phys. Rev. Lett.*, 99:076402, Aug 2007.

[120] Frithjof B. Anders and Avraham Schiller. Real-time dynamics in quantum-impurity systems: A time-dependent numerical renormalization-group approach. *Phys. Rev. Lett.*, 95:196801, Oct 2005.

[121] Masatoshi Imada, Atsushi Fujimori, and Yoshinori Tokura. Metal-insulator transitions. *Rev. Mod. Phys.*, 70:1039–1263, Oct 1998.

[122] Qiang Han and Andrew Millis. Lattice energetics and correlation-driven metal-insulator transitions: The case of $\mathrm{ca}_2\mathrm{ruo}_4$. *Phys. Rev. Lett.*, 121:067601, Aug 2018.

[123] A. Charnukha, Z. P. Yin, Y. Song, C. D. Cao, Pengcheng Dai, K. Haule, G. Kotliar, and D. N. Basov. Correlation-driven metal-insulator transition in proximity to an iron-based superconductor. *Phys. Rev. B*, 96:195121, Nov 2017.

[124] Mukul S. Laad and Luis Craco. Mott transitions: A brief review. *Advanced Quantum Technologies*, 7(12):2200186, 2024.

[125] Philipp Werner and Andrew J. Millis. Doping-driven mott transition in the one-band hubbard model. *Phys. Rev. B*, 75:085108, Feb 2007.

[126] Justin Leshen, Mariam Kavai, Ioannis Giannakis, Yoshio Kaneko, Yoshi Tokura, Shantanu Mukherjee, Wei-Cheng Lee, and Pegor Aynajian. Emergent charge order near the doping-induced mott-insulating quantum phase transition in sr3ru2o7. *Communications Physics*, 2(1):36, 2019.

[127] K. J. Kapcia, S. Robaszkiewicz, M. Capone, and A. Amaricci. Doping-driven metal-insulator transitions and charge orderings in the extended hubbard model. *Phys. Rev. B*, 95:125112, Mar 2017.

[128] Kenji Ishii, Takami Tohyama, Shun Asano, Kentaro Sato, Masaki Fujita, Shuichi Wakimoto, Kenji Tustsui, Shigetoshi Sota, Jun Miyawaki, Hideharu Niwa, Yoshihisa Harada, Jonathan Pelliciari, Yaobo Huang, Thorsten Schmitt, Yoshiya Yamamoto, and Jun'ichiro Mizuki. Observation of momentum-dependent charge excitations in hole-doped cuprates using resonant inelastic x-ray scattering at the oxygen k edge. *Phys. Rev. B*, 96:115148, Sep 2017.

[129] Hakuto Suzuki, Matteo Minola, Yi Lu, Yingying Peng, Roberto Fumagalli, Emilie Lefrançois, Toshinao Loew, Juan Porras, Kurt Kummer, Davide Betto, et al. Probing the energy gap of high-temperature cuprate superconductors by resonant inelastic x-ray scattering. *npj Quantum Materials*, 3(1):65, 2018.

[130] E. H. da Silva Neto, M. Minola, B. Yu, W. Tabis, M. Bluschke, D. Unruh, H. Suzuki, Y. Li, G. Yu, D. Betto, K. Kummer, F. Yakhou, N. B. Brookes, M. Le Tacon, M. Greven, B. Keimer, and A. Damascelli. Coupling between dynamic magnetic and charge-order correlations in the cuprate superconductor $\mathrm{nd}_{2-x}\mathrm{ce}_x\mathrm{cuo}_4$. *Phys. Rev. B*, 98:161114, Oct 2018.

[131] Matthias Hepting, Laura Chaix, EW Huang, R Fumagalli, YY Peng, B Moritz, K Kummer, NB Brookes, WC Lee, M Hashimoto, et al. Three-dimensional collective charge excitations in electron-doped copper oxide superconductors. *Nature*, 563(7731):374–378, 2018.

[132] H. Miao, R. Fumagalli, M. Rossi, J. Lorenzana, G. Seibold, F. Yakhou-Harris, K. Kummer, N. B. Brookes, G. D. Gu, L. Braicovich, G. Ghiringhelli, and M. P. M. Dean. Formation of incommensurate charge density waves in cuprates. *Phys. Rev. X*, 9:031042, Sep 2019.

[133] Kenji Ishii, Masahito Kurooka, Yusuke Shimizu, Masaki Fujita, Kazuyoshi Yamada, and Jun'ichiro Mizuki. Charge excitations in nd2−xcexcuo4 observed with resonant inelastic x-ray scattering: Comparison of cu k-edge with cu l3-edge. *Journal of the Physical Society of Japan*, 88(7):075001, 2019.

[134] Sean Vig, Anshul Kogar, Matteo Mitrano, Ali A. Husain, Vivek Mishra, Melinda S. Rak, Luc Venema, Peter D. Johnson, Genda D. Gu, Eduardo Fradkin, Michael R. Norman, and Peter Abbamonte. Measurement of the dynamic charge response of materials using low-energy, momentum-resolved electron energy-loss spectroscopy (M-EELS). *SciPost Phys.*, 3:026, 2017.

[135] R. S. Fishman and M. Jarrell. f-sum rule for the spin conductivity in itinerant magnets. *Journal of Applied Physics*, 91(10):8120–8122, 05 2002.